University of Technology, Sydney

Faculty of Science

# Analysis of trabecular bone mechanical properties from magnetic resonance images

Thesis submitted for the degree of

PhD in Science

**Zahra Zabolizadeh**

August 2012

## CERTIFICATE OF AUTHORSHIP/ORIGINALITY

I certify that the work in this thesis has not previously been submitted for a degree nor has it been submitted as part of requirements for a degree except as fully acknowledged within the text.

I also certify that the thesis has been written by me. Any help that I have received in my research work and the preparation of the thesis itself has been acknowledged. In addition, I certify that all information sources and literature used are indicated in the thesis.

Signature of Student

_____

# ACKNOWLEDGMENT

In acknowledging the contributions of a number of people to this thesis, it is difficult to know where to start and where to stop. I have been inspired on my learning journey by a number of people, many of whom contributed to my development well before the research commenced. I therefore want to thank to my parents and sisters for the inspiration, love and support that they have provided me in my life journey. I want to thank my amazing husband Kazem for his encouragement and support, and my two wonderful sons Taha and Arad. Without their sacrifice and love, I doubt that I would have made it this far.

I would like to take this opportunity to express my sincere gratitude and appreciation to my supervisor Dr Michael Braun for his guidance, support, encouragement, and empathy throughout the candidature. He gave me so much of his time and effort that I am in debt to him forever.

I would like to extend my great appreciation to my co-supervisor Dr Ali Saleh for his support and guidance. I want also to thank Dr Geoff Anstis who was my associate supervisor at the start. I would also like to thank Dr Terry Brown for his help with finite element analysis software. I am grateful for the support and help shown by Professor William Walsh and his team members Dr Nicky Bertollo and Mr Nick Russell, in the Surgical Orthopaedic Research Lab, and Dr Carl Power at the Oncology Research Centre, Prince of Wales Hospital, University of New South Wales.

I would like to thank to my friends and staff in the Faculty of Science and School of Physics and Advanced Materials, who have supported and encouraged me throughout the duration of this PhD, especially Ms Rochelle Seneviratne and Ms Linda Foley. Special thanks are due to Dr Norman Booth in UTS Material testing lab, Mr Gregory Dalsanto and Mr Greg Evans in Science workshop, Mr Michael Lake, Mr Philip Lawrence and Mr Harry Simpson. I would also like to thank to Professor Geraldine Naughton for her encouragement and Dr Felix Wehrli for providing MR image data, ANSYS technical support team at LEAP Australia, and Dr Matthew Gaston in the Faculty of Engineering and IT.

I would like to thank Dr Gary Cowin and Dr Karine Mardon at the Centre for Advanced Imaging, University of Queensland, for their help and support with μCT, μMR, and whole-body MR imaging. Finally, I would like to acknowledge the University of Technology Sydney for the IRS scholarship.

## Dedication

This thesis is dedicated to my husband Kazem for his patience, sacrifice, courage and support. Without his willingness to share parenting, while he was also doing his PhD during my study, I would not have considered undertaking this project.

# Table of Contents

# List of Figures

# List of Tables

# List of Abbreviations

| | |
|---|---|
| aBMD | Areal bone mineral density |
| BMD | Bone mineral density |
| BV/TV | Bone volume fraction |
| CT | Computed tomography |
| DICOM | Digital Imaging and Communications in Medicine |
| DXA | Dual energy x-ray absorptiometry |
| FE | Finite element |
| FEA | Finite element analysis |
| FEM | Finite element method |
| FID | Free induction decay |
| FLASE | Fast large-angle spin echo |
| FLASH | Fast low-angle shot |
| FSE | Fast spin echo |
| HR-pQCT | High resolution peripheral quantitative computed tomography |
| IDL | Interactive Data Language |
| IGFA | Image guided failure assessment |
| IOF | International Osteoporosis Foundation |
| MIMICS | Materialises Interactive Medical Image Control System |
| MR | Magnetic resonance |
| MRI | Magnetic resonance imaging |
| MSE | Multiple spin echoes |
| MTD | Main trabecular direction |
| NMR | Nuclear magnetic resonance |
| PCG | Preconditioned conjugate gradient |
| PBS | Phosphate buffered saline |
| PD | Proton density |
| PVE | Partial volume effect |
| QCT | Quantitative computed tomography |
| RF | Radio frequency |

| | |
|---|---|
| SE | Spin echo |
| SNR | Signal-to-noise ratio |
| Tb.N | Trabecular number |
| Tb.Sp | Trabecular separation |
| Tb.Th | Trabecular thickness |
| TE | Echo time |
| TR | Repetition time |
| µCT | Micro computed tomography |
| µMRI | Micro magnetic resonance imaging |
| vBMD | Volumetric bone mineral density |
| WHO | World Health Organization |

# ABSTRACT

Bone mineral density (BMD) measured by dual energy x-ray absorptiometry (DXA) is often used in the clinical diagnosis of bone disorders such as osteoporosis. However, several studies have shown that measuring BMD alone does not provide sufficient discrimination between individuals with and without increased fracture risk. In fact, bone quality is affected also by the bone micro-architecture and material properties. The development of imaging techniques, particularly computed tomography (CT) and magnetic resonance (MR) imaging, allowed the generation of three-dimensional (3D) images for the morphological analysis of trabecular bone. Furthermore, the 3D image data can be the source of finite element (FE) models. FE analysis of such data represents a means to assess the mechanical response virtually. Whole-body CT and MRI scanners are able to provide three-dimensional images *in vivo* of human femoral and spinal sites but compared to μCT and μMR, have poorer resolution and lower signal-to-noise ratio. As a result of the low resolution, a significant partial volume effect is expected to affect the reconstructed images primarily by blurring the interface between bone and soft tissue. Thus, the implications of such limitations on the FE assessment of mechanical properties should be investigated.

The main goal of this study was to assess the capability of whole-body low resolution MRI-based finite element model for the prediction of trabecular bone mechanical properties. The apparent elastic modulus and the displacement field were assessed and compared to a high resolution MR model. The effect of image voxel

size on these properties was examined using μMR images acquired with different resolutions.

The estimated mechanical properties of two trabecular bone samples (A and B), as assessed by whole-body MRI-based FE analysis, were compared with the corresponding measurements obtained from the validated μMRI-based FE analysis. It was found that increasing the voxel size from 30 μm to 200 μm raised the apparent elastic modulus by up to 13% and 21% for bone samples A and B, respectively. For whole-body MR, with voxel size of 260 μm, the overestimate rose to 24% for both bone samples. However, the apparent tissue elastic modulus stayed within the range (722- 1207) MPa, and (777 – 1228) MPa for bone samples A and B, respectively, imaged with high resolution μMR. The variations in the apparent elastic modulus appear to correlate with differences in the bone volume fraction, which varied between 0.44 and 0.68. FE analysis of load levels in the elastic range indicated that the more computationally costly geometric non-linear analysis did not improve the results significantly. Hence, a linear elastic FE analysis was deemed to be sufficiently accurate at low load levels.

In addition to estimating the apparent elastic modulus, FE analysis can produce a displacement field that represents the response to applied compression at every point in the trabecular bone. The results show that increasing the voxel size leads to a systematic overestimation of the mean displacement compared to the reference values. However, the mean norm displacement estimated from whole-body MR (0.64 mm) in the direction of the applied compression force falls within the range obtained from high resolution μMR (0.64 ± 0.13 mm). The results also suggest that the information provided by displacement field values may be statistically

uncorrelated with the apparent elastic modulus and hence serve as an additional source of parameterization of the mechanical response of trabecular bone.

The application of whole-body MRI to trabecular bone analysis is expected to be affected not only by resolution but also by other effects arising from the low strength of the steady magnetic field, the large imaging volume, and motion artefacts. Nevertheless, both the estimated apparent elastic modulus and displacement field are compatible with those obtained from µMR of comparable resolution.

Within the limit of this study the predictions of FE analysis derived from whole-body MR are within the range of predictions based on high resolution µMR, indicating a potential suitability of MR for assessment of bone strength.

# Chapter 1: Introduction

## 1.1 Introduction

The primary functions of bones are to provide mechanical support for the body, facilitate the body motion, and protect vital organs such as heart, lungs, brain, and spinal cord. Many bones are made up of two tissue types. The hard uniform outer layer is called the *cortical bone*. The interior of the bone, which contains a honeycomb network of hard bone with a very high surface area, is called the *cancellous* or the *trabecular bone*. The trabecular bone consists of a lattice of interconnected of tiny strands of bone called *trabeculae* which are either plate-like or road-like or a combination of both. Trabecular bone plays an important role in load transmission and energy absorption in major joints such as the knee, the hip and the spine.

Bone is a living tissue and can adapt its properties and configuration to mechanical stimuli (Wolff's law, 1892) through remodelling. Bone remodelling that occurs continually to repair, replace, and remove damaged or old bone and is a necessary process in the maintenance of the structural integrity of the skeleton to meet the mechanical demands. Bone remodelling induces bone structure adaptation to mechanical load which makes it stronger and denser if healthy, or weaker and more porous if unhealthy. Since trabecular bone makes up approximately 67% of the total bone surface and bone remodelling occurs on the whole bone surface, it is more sensitive to the effects of bone diseases than cortical bone. In metabolic bone disease, such as osteoarthritis and osteoporosis, the low bone mass and

microstructural deterioration of trabecular bone due to an imbalance in bone remodelling can lead to reduction in trabecular bone strength, thus leading to increasing bone fragility and fracture risk in the hip, wrist, and spine where trabecular bone is most prevalent.

According to International Osteoporosis Foundation (IOF), worldwide, 200 million women were estimated to have osteoporosis in 2007. The number of osteoporosis-related hip fractures has been estimated to increase approximately 1.6 million each year; by 2050 this number could reach between 4.5 million and 6.3 million as the elderly population continues to grow. In Australia in 2007, 2.2 million were estimated to have osteoporosis (75% women and 25% men), and it will have increased to 3 million by 2012. The estimated national direct expenditures (hospital and nursing home) related to osteoporosis fractures are $1.9 billion per year, and is expected to increase with the ageing of the population (IOF 2011). Given the clinical significance of osteoporosis, it is critical to accurately diagnose individuals who are at risk of fracture. If the bone diseases can be diagnosed in the early stages, then there would be an opportunity to begin treatment earlier with non-invasive options.

The clinical diagnosis of bone disorders such as osteoporosis is often based on measurements of areal bone mineral density (BMD), using dual energy x-ray absorptiometry (DXA). One limitation of the BMD measurement is that it gives only mineral density values that combine cortical and trabecular bone. Thus, due to bone degenerative diseases, the variation in material properties and three-dimensional structure of trabecular bone, which are important factors affecting bone strength, are not considered. Bone strength refers to the ability of bone to resist fracture and is determined by its material composition and structure. In the context of this thesis,

factors that contribute to bone strength but are not accounted for by measures of bone density or mass are termed bone quality factors.

Three common methods to measure or predict trabecular bone quality are by physical experiments, imaging techniques and finite element simulation. Physical experiments use strain gauges directly bonded to the bone to provide apparent strain values but not tissue values. Also, these gauges are difficult to mount on bone, because of irregular bone surface topology. The use of a strain gauge in humans is limited by the need for surgery to implant the gauge and this approach is invasive.

Imaging techniques, in particular computed tomography (CT) and magnetic resonance (MR) imaging, provide three-dimensional architecture images for the morphological analysis of trabecular bone. The morphological parameters (trabecular bone indices), such as trabecular thickness, trabecular spacing, trabecular number, and bone volume fraction (the fraction of the total volume occupied by bone), can be calculated but do not measure mechanical response of bone. In addition, morphology studies could not fully explain the pathological variation of the apparent mechanical properties of trabecular bone.

Besides experimental and structural analysis approaches, numerical simulation methods, principally finite element (FE) computer method became accepted research tools for estimating the mechanical properties of bone (Les et al. 1997). With the development of imaging technology, including computed tomography (CT), micro computed tomography (μCT) and magnetic resonance (MR) imaging, the finite element (FE) method based on medical image datasets is a potentially useful research and clinical tool for non-invasive, non-destructive and repeatable evaluation

of the mechanical properties of bone under loading. Apparent level (referring to intact specimen rather than component tissues) results of the bone mechanical properties as well as local stress and strain can be obtained from FE modelling based on µCT or µMR images (van Rietbergen et al. 1995, Cody et al. 1999)

Recently, the FE method based on high resolution imaging techniques namely micro-magnetic resonance (µMR) imaging and high resolution peripheral quantitative computed tomography (HR-pQCT), permitted the estimation of human *in vivo* trabecular bone quality at peripheral sites such as the distal radius, the distal tibia and the calcaneus (Boutroy et al. 2005, MacNeil & Boyd 2008). A disadvantage of the technique is that it is limited to peripheral sites where as osteoporosis fractures are more likely in the proximal femur and the lumbar spine.

CT and MRI scanners, routinely used in clinical practice, that can accommodate the full cross section of the patient's body (to be referred to as "whole-body" scanners) are able to provide three-dimensional images *in vivo* of human femur and spine but the resolution of the images is not high enough to visualize individual trabeculae . Unlike CT, MR makes no use of ionizing-radiation and is therefore safer in particularly in paediatric skeletal radiology. However, the capability of whole-body MRI-based FE analysis for the prediction of trabecular bone mechanical properties such as stiffness, tissue elastic modulus and displacement fields is still unknown.

Therefore, this research project aims to examine the capability of such MR image based FE models to predict mechanical properties of trabecular bone. The effect of MR image voxel size on the determination of trabecular bone mechanical properties based on FE analysis will also be investigated. To the best of the author's

knowledge, this is the first study to date, which applies and validates whole-body MR image based FE analysis to assess quantitatively the mechanical properties of the trabecular bone. In addition, the thesis describes an original investigation of the effect of different physical MR voxel sizes on the outcomes of FE analysis. There have been prior studies of the effect of μCT and μMR image resolution on the structural parameters of trabecular bone (Wehrli et al. 2003, Wehrli et al. 2006, Kim et al. 2012), and μCT image resolution on the mechanical parameters of trabecular bone (Keyak & Skinner 1992, van Rietbergen et al. 1995, Verhulp et al. 2006, Bevill & Keaveny 2009, Rajapakse et al. 2010, Mueller et al. 2011). However, the effect of MR image resolution on the mechanical parameters of trabecular bone has not been investigated. Such studies may not extend into the clinical resolution domain. Therefore, the effect of the influence of low resolution on the FE analysis needs further investigation. A comparison of FE analysis based on high resolution images and whole-body MRI is necessary to assess the suitability of the latter as a clinical source of structural data for assessment of bone mechanical properties

## 1.2 Research aims

The main aim of the present study was to investigate the capability of the whole-body MRI-based FE analysis to estimate trabecular bone mechanical properties. The results were compared to high resolution *in vitro* imaging modalities such as μMRI. Current whole-body MR scanners operate with voxel sizes that exceed the thickness of human trabeculae. Thus, a significant partial volume effect is expected (Hwang & Wehrli 2002). The voxel value is the weighted average of intensities of all tissues contained within the PSF centred on the voxel. The weight reflects both the volume of each tissue and the shape of the PSF. Even if the voxel is homogeneous, its

intensity may be artefactually changed by the presence outside the voxel of contrasting tissues in the tails of the point spread function centered on the voxel. All imaging modalities are subject to PVE but the effect becomes more significant at lower resolutions. The proximity of contrasting bone and soft tissues in the fine trabecular structure makes it particularly sensitive to PVE.

Thus, the first aim of this study was to assess the accuracy of μCT image-based FE model in the prediction of trabecular bone mechanical properties as compared to mechanical test measurements. The second aim was to compare the estimated mechanical properties of trabecular bone, as assessed by μMR-based FE model, against those based on μCT scans. The third aim was to investigate the suitability of whole-body MRI-based FE modelling to predict the mechanical properties of trabecular bone by a comparison to validated μMRI-based FE analysis. In addition, the effect of MR image voxel size on the FE result was evaluated.

## 1.3 Thesis Outline

The body of the thesis is presented in the following four chapters:

**Chapter 2** provides a summary of bone anatomy and bone imaging modalities, as well as a discussion of methods that quantify the mechanical properties of trabecular bone such as strain gauge measurement, and finite element modelling. Finally, a review of FE models based on MR images is presented, followed by the motivation of the current study

**Chapter 3** describes the μCT, μMR, and MR protocols adopted for both the prototyped model, and trabecular bone samples, as well as image processing method, and finite element modelling. The mechanical test protocol is then described. Finally, the method developed for the comparison of displacement fields is obtained.

**Chapter 4** presents the results and discussions of findings include mechanical testing, the validation of FE analysis, and the calculated mechanical properties from the FE analyses based on μCT, μMR and clinical MR images. Also, it includes the results and discussion of the effect of different image voxel sizes on the mechanical properties such as tissue elastic modulus, stiffness, and displacement fields. Finally, limitations and conclusions of the research are provided, and a possible direction for future research is pointed out.

# Chapter 2: Background and Literature Review

## 2.1 Introduction

In the following sections, relevant background and literature will be reviewed. First, a general anatomy and function of bone will be described. In section 2.3, plain x-ray, DXA, CT and MR imaging will be discussed. In the next section, BMD, generally accepted as the gold standard for quantifying bone health, and methods for quantifying of morphological parameters will be discussed. The different methods to quantify the mechanical properties of trabecular bone are examined. The strain gauge measurement and mechanical testing will be presented as the physical methods to quantify mechanical strains/stresses whereas the finite element models will be presented as the non-invasive virtual methods to estimate mechanical properties. The previous studies of FE models based on MR images will be reviewed and the motivation of the current study will be outlined.

## 2.2 Basic Bone Morphology and Mechanical Function

Bone is the main component of the skeleton; it provides mechanical support, enables motion, protects internal organs, and provides leverage for muscle contraction. There are two major bone components types in the skeleton: the *cortical bone* (also referred to as the *compact bone*) and the *trabecular bone* (also referred to as the *spongy bone* or the *cancellous bone*) (Figure 2.1). The basic structure unit of the cortical bone is the osteon. Cortical bone forms the outer shell of most bones and is mainly responsible for a supportive, protective function and surrounds trabecular

bone. Trabecular bone has a spongy-like structure and its basic unit are called *trabeculae*, which is made up of parallel lamellae. The trabeculae divide the interior volume of the bone into intercommunicating pores, which are filled with a variable mixture of red and yellow marrow. Each lamellae in both cortical bone and trabecular bone consists mostly of protein (mainly type I collagen fibers) and mineral in the form of hydroxyapatite crystals. Trabecular bone is located mainly in the epiphyseal and metaphyseal regions of long bones, i.e. the proximal femur in the leg or the radius in the arm, and also the vertebral body in spine. Trabecular bone plays an important role in load transmission and energy absorption in major joints such as the knee, the hip and the spine.

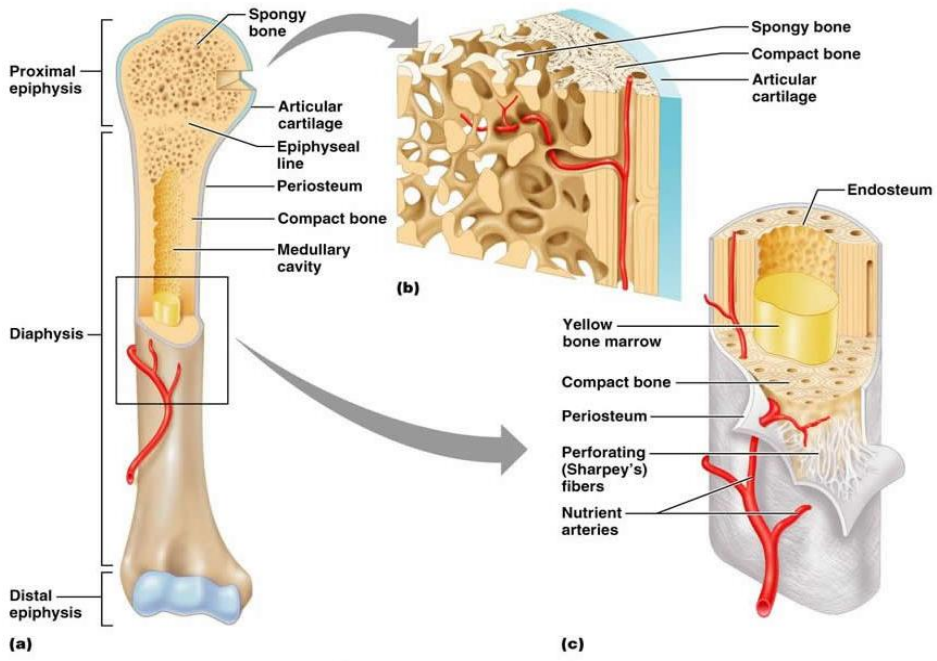


**Figure 2.1** A typical long bone is shown (a). The spongy-like structure (b) is the trabecular bone (named spongy bone in this figure). The cortical bone (compact bone) is the outer layer of the long bone structure (c) (From Carter 2011).

Bone has an excellent capacity to adapt to the change of environmental loading through remodelling. Bone remodelling, occurs continually, to repair, remove old or

damaged bone tissue and replace it with new bone tissue. The turnover (the proportion of the bone cells replaced in a given time period) is faster in trabecular bone than in the cortical bone because the former has a much large surface area per unit volume and a greater metabolic activity (Seeman & Delmas 2006).The study of trabecular bone is of considerable clinical importance due to the higher impact of its changes than the cortical bone on the aetiology of osteoporosis, age-related fractures, and damage due to trauma. Osteoporosis is characterized by a loss of bone strength due to a reduction of bone density (in both the cortical and trabecular bone) and the alteration of trabecular structure (Figure 2.2). These changes lead to increased bone fragility and fracture risk. More information about bone function will be found in Cowin's text (Cowin 2001).

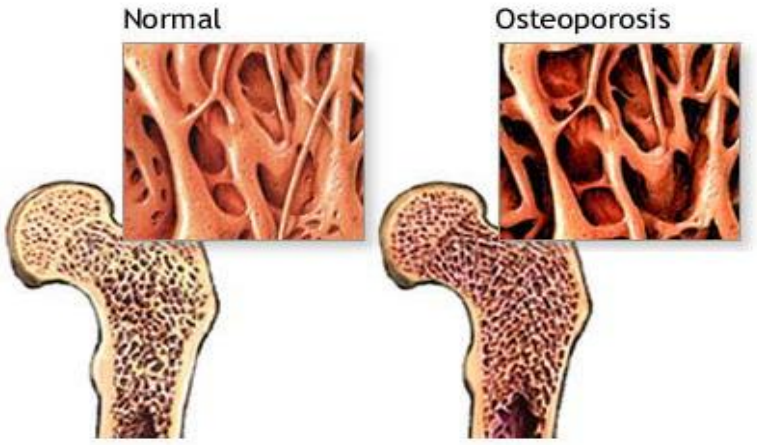


**Figure 2.2** A comparison between healthy bone (left) and osteoporotic (right) bone microstructure (From Evert 2011).

The bone strength is characterized by the stress or strain at which the bone fails, and failure may be defined by the ultimate stress or the ultimate strain (Carter & Hayes 1977). Parameters that contribute to bone strength but are not accounted for by measures of bone density or mass are trabecular microarchitecture and

biomechanical properties of the trabecular bone. The assessment of trabecular bone strength is important for the diagnosis and the effective treatment of bone metabolic disorders such as osteoporosis. Methods of estimating the strength of the trabecular bone include bone mineral densitometry, trabecular bone morphological analysis, mechanical testing, and finite element simulation. In the following sections different modalities for bone imaging will be discussed first, followed by discussion on the various methodologies to quantify the morphological and mechanical properties of the trabecular bone.

## 2.3 Imaging Modalities of Bone

The advancements in medical imaging technology have made non-invasive detection of microstructural changes in the bone possible. Currently used imaging technologies in bone research are plain x-ray, dual energy x-ray absorptiometry (DXA), computed tomography (CT), quantitative computed tomography (QCT), and magnetic resonance imaging (MRI) which provide two- or three-dimensional images for the morphological analysis, as well as finite element analysis of the trabecular bone.

### 2.3.1 Plain X-ray

Techniques using x-ray radiation quantitate the amount of bone at a given anatomic site. As x-ray photons with intensity $I_0$, penetrate some material, such as bone, the incident number and intensity of the photons decrease exponentially, due to their absorption by the material along the path of the x-ray. Since, bone has a higher atomic number than soft tissue, it absorbs most of the x-ray photons by photoelectric

processes. The attenuation of a mono-energetic beam passing through a homogeneous object obeys Lambert-Beer's Law,

$$I = I_0\ e^{-\mu x}, \tag{2.1}$$

where $I_0$ and $I$ are the primary and transmitted intensities, μ is the average linear attenuation coefficient for the object being scanned (units1/m), and $x$ is the length of the x-ray path through the object.

If the object is composed of non-homogeneous material, Equation (2.1) becomes

$$I = I_0\, e^{-\int \mu(x)\mathrm{d}x}, \tag{2.2}$$

where the absorption coefficient μ is integrated over the thickness of the material.

### 2.3.2 Dual energy X-ray absorptiometry

DXA is a 2D projectional imaging technique, which employs x-ray beams of two different energies to differentiate between bone tissue and soft tissue. DXA has two modes of operation, pencil-beam and fan-beam. An x-ray tube produces x-rays with a broad range of energies, which will then be transmitted through an object. The energy of these x-rays should be narrowed down to smaller range in order to produce two main energy peaks (one higher and one lower). This is done by filtering, typically with K-edge filters. The DXA system is connected to a computer which reconstructs and displays the attenuation map of the object, as well as the calculated bone mineral density, with the calculated mass per unit area of bone mineral on the object. The following equations are the expression for two x-ray beams with different energy levels, being attenuated through two materials (i.e. bone b and soft tissue s):

$$I' = I_0' \, e^{-\left[\left(\frac{\mu}{\rho}\right)_s' M_s + \left(\frac{\mu}{\rho}\right)_b' M_b\right]}, \tag{2.3}$$

$$I = I_0 \, e^{-\left[\left(\frac{\mu}{\rho}\right)_s M_s + \left(\frac{\mu}{\rho}\right)_b M_b\right]}, \tag{2.4}$$

where the primed values indicate the lower energy x-rays, and un-primed values indicate the higher energy x-rays. $I_0$ and $I$ are the incident and transmitted intensities, $\mu/\rho$ is the mass attenuation coefficients for soft tissue (s) and bone (b). $M_s$ and $M_b$ are the areal densities of soft tissue and bone respectively. The equations are solved for $M_b$, by taking the natural logarithms of both sides of the two equations and rearranging as follows

$$\frac{\ln\left(\frac{I}{I_0}\right) + \left(\frac{\mu}{\rho}\right)_b M_b}{\left(\frac{\mu}{\rho}\right)_s} = \frac{\ln\left(\frac{I'}{I_0'}\right) + \left(\frac{\mu}{\rho}\right)_b' M_b}{\left(\frac{\mu}{\rho}\right)_s'},$$

$$M_b = \frac{\left(\frac{\mu}{\rho}\right)_s' \ln\left(\frac{I}{I_0}\right) - \left(\frac{\mu}{\rho}\right)_s \ln\left(\frac{I'}{I_0'}\right)}{\left(\frac{\mu}{\rho}\right)_b' \left(\frac{\mu}{\rho}\right)_s - \left(\frac{\mu}{\rho}\right)_b \left(\frac{\mu}{\rho}\right)_s'} \tag{2.5}$$

### 2.3.3 Computed tomography

Computer tomography is a non-destructive technique which generates cross-sectional images of an object by rotating an x-ray source and detector array around the object. Both the x-ray source and the detector array are housed inside a gantry. At each angle increment a fan beam generates projections. These projections are reconstructed by computer using a back-projection algorithm to calculate the average linear attenuation coefficients within a cross-section of the object, and then to create a 3D CT image of the scanned region. During data acquisition, a series of x-ray beams with intensity $I_0$ are projected from an x-ray source through the subject. The

x-rays are differentially absorbed by the material along the path of the x-ray and the beam gets attenuated (Equation 2.2). The transmitted x-ray intensity $I$ is then measured by a detector array placed opposite the x-ray tube in the gantry. The transmitted intensity value measured by the detectors to provide a single projection dataset through the gantry is rotated at multiple angles around the object. The projection for a monochromatic x-ray beam through a material is

$$P = \ln\frac{I_0}{I} = \int \mu(x)\mathrm{d}x, \tag{2.6}$$

where $\mu(x)$ is the attenuation coefficient at position x along the ray path.

Therefore, generally the total attenuation $P$ of a ray at position $r$ on the projection at angle $\theta$ is given by the line integral

$$P(r,\theta) = -\int \mu(x,y)dx\, d_y, \tag{2.7}$$

where the value of $r$ onto which the point $(x, y)$ will be projected at angle $\theta$ is given by

$$r = x\cos\theta + y\sin\theta. \tag{2.8}$$

Using the Dirac delta function, Equation (2.7) can be rewritten as

$$P(r,\theta) = \int_{-\infty}^{+\infty}\int_{-\infty}^{+\infty} \mu(x,y)\delta(x\cos\theta + y\sin\theta - r)\mathrm{d}x\,\mathrm{d}y. \tag{2.9}$$

By calculating the one-dimensional Fourier transform of projections at multiple angles around the object, the two-dimensional frequency domain can be filled as a series of radial lines extending from zero frequency and rotated by angle $\theta$, with interpolation on to a Cartesian coordinates .The data can then be filtered and the inverse two-dimensional Fourier transform calculated to reconstruct the original object. An equivalent process can be used to form a more accurate reconstruction. This process involves taking the one-dimensional Fourier transform of a series of projections, filtering the resulting data, taking the inverse one-dimensional Fourier

transform of each projection, and summing the resulting projections in the spatial domain. This is the concept used in filtered back-projection, and is the most commonly used reconstruction method.

Contrast in CT is defined as difference in the attenuation coefficient between two adjacent regions of the image. The linear attenuation coefficient is usually converted into the CT number in Hounsfield Unit (HU) as follows:

$$\text{HU} = \frac{(\mu_m - \mu_w)}{\mu_w} \times 1000, \tag{2.10}$$

where $\mu_m$ is the linear attenuation coefficient of the material and $\mu_w$ is the linear attenuation coefficient of water. On the Hounsfield Unit scale, water has an attenuation value of zero. Air and fat have lower attenuation value than water and appear dark in the final image, while the bone tissue has higher attenuation values than water and appears bright in the final CT image.

The in-plane resolution of CT images is limited mainly by the source-detector distance, the source-object distance, the number of detector elements and the size of the object itself. The in-plane resolution (down to 0.33 mm) and the resolution in z-direction (down to 0.4 mm) of a conventional clinical CT are not high enough to depict the detail of the trabecular structure.

### 2.3.4 Micro-computed tomography

Micro-computed tomography was pioneered by Feldkamp in 1989, for the evaluation of the 3D microstructure of trabecular bone, using a micro-focus x-ray tube as the source, a vidicon camera as a 2D detector, and a cone-beam reconstruction algorithm

(Feldkamp et al. 1989). Current micro-CT systems employ a similar technology to conventional CT, but use a micro-focus x-ray tube as the source, and an image intensifier as the detector. Therefore, its in-plane resolution (2 µm to 100 µm) is much higher than clinical CT (0.33 mm – 1 mm). The µCT scanners can capture the detail of individual trabeculae, and morphological measurements based on µCT are often adopted as a gold standard for validation of studies using other imaging modalities with lower resolutions (Bonse et al. 1994, Rüegsegger et al. 1996, Peyrin et al. 1998). As the source-detector distance of µCT scanners is less than that of the CT system, the living specimen must be small enough to be positioned within the scanner and thus µCT scanner is not suitable for human use.

### 2.3.5 Quantitative-computed tomography

A high resolution peripheral QCT (HR-pQCT) has recently been developed for *in vivo* human measurements at peripheral sites, such as the distal radius or the tibia at a resolution of 82 µm. It can accurately quantify the bone density and microstructure for both trabecular and cortical bone separately (Laib et al. 1998). QCT is a non-destructive technique that measures the spatial mineral distribution and produces 3D images of the interior structure of an object. A conventional CT scanner is used, and x-rays attenuation measurements are compared with a standard reference to calculate volumetric bone mineral density. Unlike DXA, QCT-based vBMD is independent of bone size and can be measured separately in the trabecular and cortical bone compartments. Bone measurements from QCT have been used to evaluate sex-, age-, and ethnicity-related differences in density and geometry at the lumbar spine and proximal femur, thereby providing insight into the skeletal fragility

(Keaveny et al. 2001, Buckley et al. 2007). QCT has also proved useful in monitoring drug therapies as their effects may not be apparent using standard DXA measurements (Black et al. 2003).

Although HR-pQCT is a non-destructive method, it uses ionizing radiation (x-rays) and the spatial resolution may be limited by dose considerations. A recent clinical study indicated that HR-pQCT could detect the significantly different trabecular density at the distal radius in osteopenic women with a history of fracture and those without (Boutroy et al. 2005) independent of hip or spine BMD. A disadvantage of the technique is that it is limited to peripheral bone sites such as distal tibia and radius where osteoporotic fractures are less common.

The use of non-ionizing radiation in developing children is especially important since children are more radiosensitive and have more potential to develop radiation-induced cancer later in life (Brenner & Hall 2007). High resolution MR imaging has been introduced to quantify microstructural changes in trabecular bone architecture (Majumdar et al. 1994). It has comparable image quality to CT but does not rely on ionizing radiation.

### 2.3.6 Magnetic resonance imaging

Magnetic resonance imaging is used primarily in medical settings to visualize the structure and function of soft tissues and organs. The potential of MRI to detect longitudinal changes in bone micro-architecture *in vivo* has been demonstrated by various studies (Boutry et al. 2003, Chesnut et al. 2005, Takahashi et al. 2006, Wehrli et al. 2006, Wehrli et al. 2008, Zhang et al. 2008, Folkesson et al. 2011). The

fundamentals of MRI are covered extensively in texts (Callaghan 1991, Brown & Semelka 2005). The purpose of this section is to provide an introductory outline of MRI and its application to bone research.

#### 2.3.6.1 Principles of MRI

The intrinsic magnetic properties of atomic nuclei form the basis of magnetic resonance. Atomic nuclei, such as $^{1}H$, $^{13}C$, $^{31}P$, $^{23}Na$, which are composed of an odd number of protons or neutrons, possess a net nuclear angular momentum and magnetic moment. In classical mechanics, the nuclear spin can be thought of as an angular momentum associated with the rotation of a body about its centre of mass. As opposed to orbital angular momentum, which is defined by the rotation of a body about an external point, spin angular momentum or spin is an intrinsic physical property of particles, just like electric charge and mass. According to quantum mechanics, the spin of an elementary particle like a photon, electron and various quarks, is represented by a specific value of the spin quantum number.

Nuclear spin is the sum of the spins of the constituents and the orbital angular momentum of their motions in the nucleus. Unpaired protons or neutrons lead to a non-zero nuclear spin. The magnetic moment associated with the spin is given by

$$\mu = g_s \frac{q}{2m} s, \tag{2.11}$$

where $q$, $m$ and $s$ are the nucleus charge, mass and spin angular momentum, respectively, and the dimensionless quantity $g_s$ is called the spin g-factor. This is exactly the magnetic moment that is manipulated by nuclear magnetic resonance (NMR) experiments.

Water accounts for 60-80% of living tissue, and constitutes the greatest proportion of protons while macro-molecules such as proteins, and solid structures, such as bone, provide low MR signal intensity because of low density of free protons. Hydrogen nuclei are the best candidate for MRI scanners because hydrogen is the most abundant element in the human body and generates the strongest MR signal.

When a biological tissue is placed in a static external magnetic field $\boldsymbol{B}_0$, the individual spins precess about the direction of the field at a frequency proportional to its strength (Figure 2.3). By convention, the magnetic field $\boldsymbol{B}_0$ is assumed to be directed along the z-axis. The precessional frequency $\omega_0$, known as the Larmor frequency, is

$$\omega_0 = \gamma|\boldsymbol{B}_0|, \tag{2.12}$$

where the gyromagnetic ratio γ is an intrinsic property of the nucleus. For the proton, it is 42.6 MHz/T.

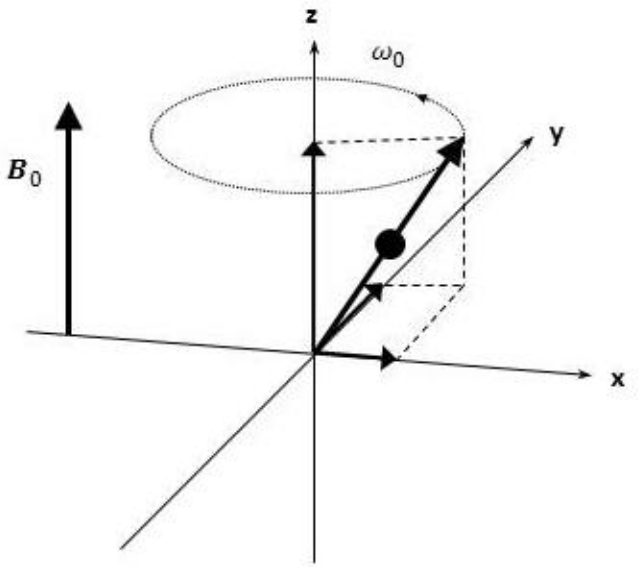


**Figure 2.3** Precession of a spin about the main magnetic field $\boldsymbol{B}_0$.

The net magnetization vector $\boldsymbol{M}$ for the collection of protons in a volume V is

$$\boldsymbol{M} = \frac{1}{V} \sum \boldsymbol{\mu_i}, \tag{2.13}$$

where $\boldsymbol{\mu}$ is the magnetic moment vector (Eq. 2.11).

The application of RF pulses of the resonant frequency disturbs the net magnetization vector $\boldsymbol{M}$, as illustrated in Figure 2.4. This process, referred to as RF excitation, is accomplished by passing a RF current through coil, which acts as a transmitter, to produce an oscillating electromagnetic field. During the pulse, the net magnetization deviates from the z-axis and acquires a component in the transverse plane. The frequency content of the RF pulses is determined by its duration and shape.

The RF pulse is represented by field $\boldsymbol{B}_1$, rotating at the Larmor frequency $\omega_0$,

$$\boldsymbol{B}_1\,(t) = B_1 \cos \omega_0\, t\, \boldsymbol{i} - B_1\, \sin \omega_0\, t\, \boldsymbol{j}. \tag{2.14}$$

During the pulse, the behaviour of $\boldsymbol{M}$ is governed by the differential equations,

$$\begin{aligned} \frac{dM_x}{dt} &= \gamma \left(M_y\, B_0 + M_z\, B_1\, \sin \omega_0\, t\right) \\ \frac{dM_y}{dt} &= \gamma\, (M_z\, B_1\, \cos \omega_0\, t - M_x\, B_0) \\ \frac{dM_z}{dt} &= -\gamma\, (M_x\, B_1\, \sin \omega_0\, t + M_y\, B_1\, \cos \omega_0\, t) \end{aligned} \tag{2.15}$$

In MRI, the magnetic field is made spatially dependent through the application of magnetic field gradients $\boldsymbol{G}$. These gradients provide small linear field variations superimposed on the main magnetic field $B_0$. When an RF pulse is applied in the presence of magnetic field gradient $\boldsymbol{G}$, it will excite a slice of tissue perpendicular to the gradient direction. Suitable modulation of the RF pulse will ensure

approximately rectangular slice profile. For maximum signal a so-called 90˚ pulse is applied which nutates the net magnetization to the x-y plane, as shown in Figure 2.4.

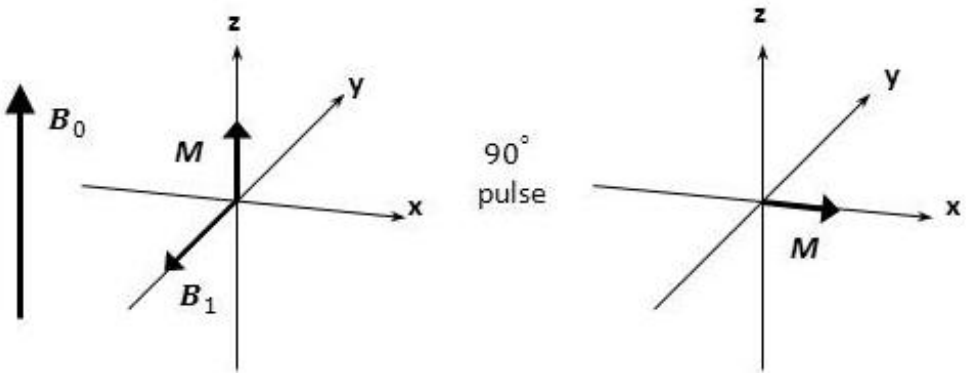


**Figure 2.4** In a reference frame rotating with Larmor frequency, a 90˚ RF pulse tips the net magnetization ***M***, initially at equilibrium, to lie in the transverse plane (From Brown & Semelka 2005).

From the end of the RF excitation, the net magnetization vector ***M*** will exponentially relax back to its equilibrium position. The transverse relaxation is governed by the spin-spin relaxation time $T_2$ while the relaxation of the longitudinal components is controlled by the spin-lattice relaxation time $T_1$. The time dependence of the nuclear magnetization ***M*** under the influence of a magnetic flux density ***B*** can be presented by Bloch equation,

$$\frac{\mathrm{d}}{\mathrm{d}t}\boldsymbol{M} = \boldsymbol{M} \times (\boldsymbol{B} + \boldsymbol{B}_1) - \frac{M_x X + M_y Y}{T_2} - \frac{M_0 - M_z}{T_1}\,\mathrm{Z}. \tag{2.16}$$

Following the excitation in the absence of any magnetic field other than the steady field $\boldsymbol{B}_0$, the Bloch equation reduces to:

$$\begin{aligned} \frac{\mathrm{d}M_x}{\mathrm{d}t} &= \omega_0 M_y - \frac{M_x}{T_2} \\ \frac{\mathrm{d}M_y}{\mathrm{d}t} &= -\omega_0 M_x - \frac{M_y}{T_2} \\ \frac{\mathrm{d}M_z}{\mathrm{d}t} &= \frac{M_0 - M_z}{T_1} \end{aligned} \tag{2.17}$$

where $M_0$ is the initial magnetization, $\omega_0 = \gamma \boldsymbol{B}_0$, and $t$ is time. Following a 90˚ excitation, the longitudinal and transverse magnetization components can be written as:

$$M_z(t) = M_0(1 - e^{-t/T_1}), \tag{2.18}$$

$$M_{xy}(t) = M_0\, e^{-t/T_2}. \tag{2.19}$$

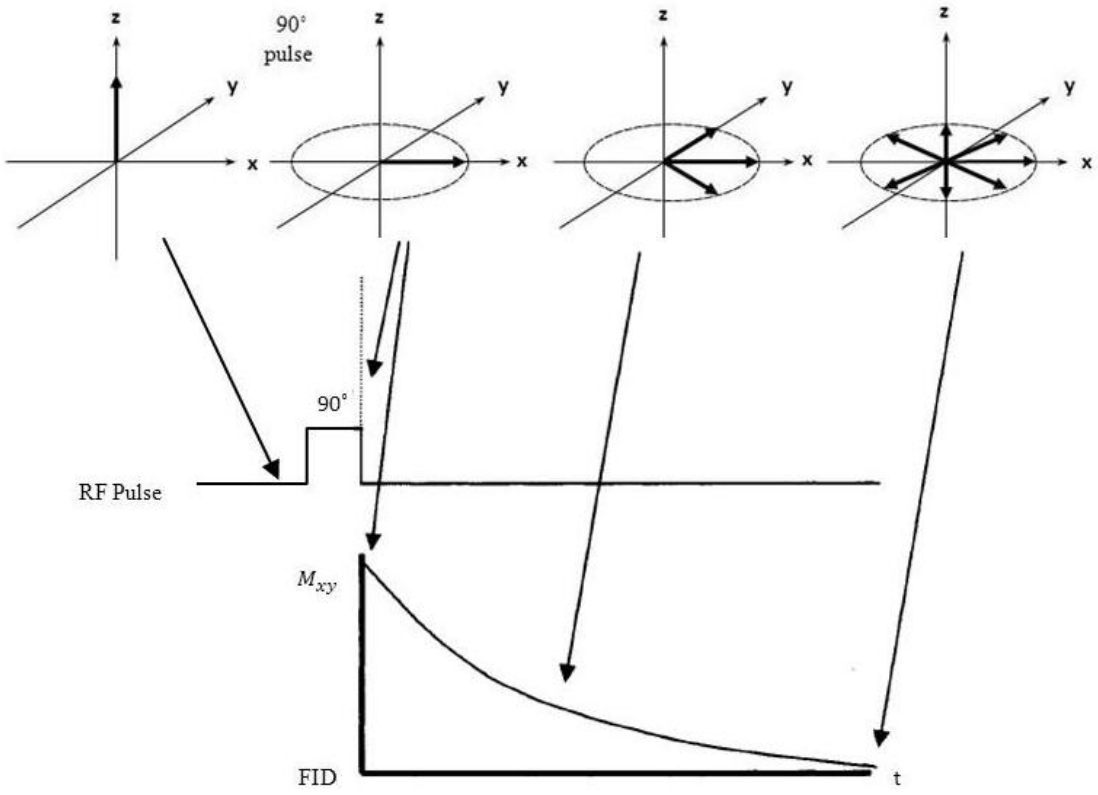


**Figure 2.5** Magnetization decay after 90˚ pulse, showing in a rotating frame (top). Free induction decay (FID) of magnetization after a 90˚ pulse (bottom). At the end of the 90˚ pulse, all magnetization is aligned with the rotating x-axis. The individual magnetic moments continue to precess at different frequencies, resulting in the decrease of the magnetization component in the transverse plane (x-y plane) $\boldsymbol{M_{xy}}$ over time. When the individual vectors are uniformly distributed in x-y plane, the net magnetization is zero and the signal vanishes (Adapted from Brown & Semelka 2005).

The $T_2$ relaxation arises from the spread of resonant frequencies and the subsequent loss of phase coherence of the transverse magnetization. Since the magnetization $\boldsymbol{M}$ eventually returns to equilibrium $M_0$, $T_2 \leq T_1$. Unlike $T_1$, $T_2$ is largely independent of field strength. $T_1$ and $T_2$ relaxation constants are characteristics of the molecular environment of a tissue.

Imposing a gradient in a given direction while recording the signal from the precessing transverse magnetization, encodes the coordinate positions along the gradient direction by the frequency of the obtained signal. This process is known as frequency encoding. Similarly, in phase encoding, gradient pulses are applied separately along the orthogonal direction to the frequency encoding to allow for the cumulative phase to be a function of the spatial position in the direction of the phase-encoding gradient. The specific order and timing associated with applying the gradient magnitudes in each direction is referred to as the pulse sequence. Reconstructing the raw data into useful images is then accomplished through an inverse 2D Fourier transform.

The intensity values of the acquired image are generally influenced by the underlying properties of the tissues from which the RF signal is generated. However, one of the primary strong points of MRI is that the contrast between different biological tissues may be tuned by varying the acquisition parameters. Proton density (PD) is a measure based upon the number of nuclei stimulated. The time between RF pulses (TR) and the time when the signal is acquired following this pulse (echo time, TE), determines the contribution from PD, $T_1$ and $T_2$ in the resulting image.

In MR imaging of the trabecular bone, the protons in bone marrow generally provide the high signal intensity and low signal is provided by bone tissue because of its minimal water content (Figure 2.6). So, the bone structure is revealed indirectly through surrounding bone marrow visualization (Ford & Wehrli 1991).

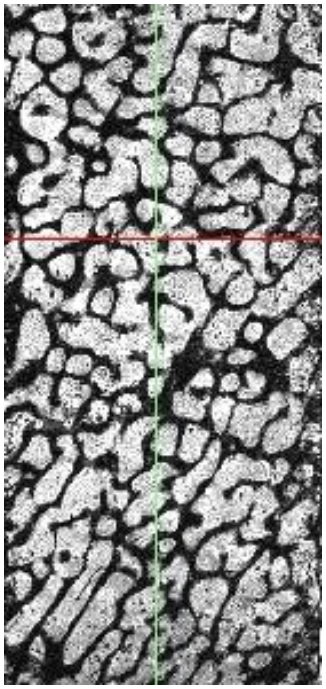

**Figure 2.6** µMR image of a bovine trabecular bone specimen

However, some studies reported techniques employing short or ultrashort echo time (UTE) pulse sequence, which detect signal from bone. UTE sequences detect both less tightly bound and free water signals. It was found that the T2* of bound water detected in this way is about 10 times shorter than that of free water. This manifest difference makes it possible to use a bi-component model to quantify the relative fractions and concentrations of both UTE detected bound and free water. Therefore, the assessment of organic matrix via bound water and bone porosity via free water using a clinical MR scanner is possible (Biswas et al. 2012).

The detected RF signal in a MRI experiment is proportional to the number of nuclei in each voxel and their magnetization. Thus, as the voxel size decreases, increasing higher magnetic field strength are required to compensate for the decrease in the numbers of spins. The limits of resolution in MRI with a given magnetic field gradient are also dependent on the type and size of RF coil, imaging scheme, and the acquisition time.

The inherent obstacles in MR imaging of trabecular bone are usually the acquisition time, signal-to-noise ratio constraints, restricted spatial in-plane resolution, partial volume effects and susceptibility artifacts (Chung et al. 1995, Li et al. 2008). At the resolution in the order of the trabecular thickness (80 μm – 150 μm), a voxel may contain both bone and bone marrow tissues and its grey level is a weighted average of its components. This effect is known as the partial volume effect (PVE) (Hwang & Wehrli 2002). The voxel value is the weighted average of intensities of all tissues contained within the PSF centred on the voxel. The weight reflects both the volume of each tissue and the shape of the PSF. Even if the voxel is homogeneous, its intensity may be artefactually changed by the presence outside the voxel of contrasting tissues in the tails of the point spread function cantered on the voxel. All imaging modalities are subject to PVE but the effect becomes more significant at lower resolutions. Also, a common artifacts in MR is aliasing caused by under sampling in Fourier space. Nonetheless, the trabecular bone morphological parameters derived from MR images still correlate well with those obtained from higher-resolution techniques such as μCT, because the trabecular spacing (300 μm – 1000 μm) is much larger than the image voxel size (Majumdar et al. 1996, Laib et al. 2001, Link et al. 2003).

To overcome those obstacles in MR imaging of trabecular bone, advances in the past decade have focused on image acquisition processing and analysis techniques (Majumdar et al. 1995, Ouyang et al. 1997, Hwang & Wehrli 2002, Boehm et al. 2003, Wehrli et al. 2003, Lammentausta et al. 2006, Raeth et al. 2006, Li et al. 2008). Different pulse sequence techniques have been tried, such as spin-echo (SE), multiple spin-echoes (MSE) (Capuani et al. 2002), fast spin-echo (FSE), fast large-angle spin-echo (FLASE) (Ma et al. 1996), and fast low-angle shot (FLASH) (Haase et al. 1986), to optimize the SNR, reduce the measuring time without loss of spatial resolution, and lower the RF power deposition. In this study, we used the FLASH pulse sequence. The technique takes advantage of excitation pulses with small flip angles, thus shortening the repetition time (TR) and the total scan time.

Since signal-to-noise ratio increases with magnetic field strength, operating at a high magnetic field strength is preferred. Typical high resolution MRI systems operate at 7 T, 9.4 T, 11.74 T, 14.1 T, and 17.6 T for *in vitro* studies of small samples. The strong static magnetic field can be used either to improve spatial resolution (with the aid of a strong magnetic field gradient) or reduce the acquisition time at a lower resolution (Banerjee et al. 2005, Bauer & Link 2009).

*In vivo* MRI of human bone is typically performed with a magnetic field strength of 1.5 T or 3 T. Most previous studies were done at 1.5 T (Herlidou et al. 2001, Newitt et al. 2002) but it was found that the signal-to-noise ratio at 3 T was significantly higher than at 1.5 T with the same imaging parameters (Ludescher et al. 2005). Recent studies (Wright et al. 2011, Juras et al. 2012) have shown practical utility of 7 T scanners for *in vivo* imaging of trabecular bone. It was found that mean SNR significantly increased at 7 T compared to 3 T (Juras et al. 2012), with an average

SNR gain of 2.8 and 4.9 compared to 3 T and 1.5 T, respectively (Wright et al. 2011).

Recent advances in μMRI allow detailed structural information of trabecular bone to be obtained (Majumdar et al. 1994, Gomberg et al. 2004, Sell et al. 2005, Palombarini et al. 2009, Folkesson et al. 2011, Orzada et al. 2011, Wright et al. 2011, Juras et al. 2012). Such imaging is limited to peripheral sites such as the distal radius, the distal tibia, and the calcaneus, due to signal-to-noise ratio constraints in the deeper regions of the skeleton such as the proximal femur and spine (Jara et al. 1993, Ma et al. 1996, Wehrli et al. 1998, Newitt et al. 2002, Ludescher et al. 2005, Kazakia et al. 2011). Improved pulse sequences and optimized coil design were used by Krug et al. (2005), to image the proximal femur with sufficient resolution to permit a structural analysis of its trabecular component.

To summarize, CT uses an ionizing radiation in the form of x-rays to perform the image acquisition. MRI employs a non-ionizing radiofrequency electromagnetic radiation, and is therefore safer. In the imaging of the trabecular bone by MRI, the bone structure is revealed indirectly through surrounding bone marrow visualization, because the protons in bone marrow generally provide the high signal intensity and low signal is provided by bone tissue because of its minimal water content. The revealed image of the trabecular bone in CT scan is due to its higher attenuation coefficient than soft tissue. Since, bone has a higher atomic number than soft tissue, it absorbs most of the x-ray photons by the photoelectric process.

### 2.3.7 Image segmentation

To construct trabecular bone structure from CT or MR images, the image must be segmented first to distinguish the bone tissue from soft tissue. In medical image analysis, anatomical segmentation is required in the identification of tissue boundaries in the image. There are many segmentation methods, including thresholding, region growing, and edge detection (Clarke et al. 1995).

Thresholding is the simplest method and two categories of this method, global and local thresholding were reported in the literature. Global thresholding is the most widely used segmentation technique. A single number (gray scale value) is selected, above which all voxels are considered bone and all remaining voxels are marked as non-bone. The segmentation procedure for the global thresholding is relatively simple and fast. The local thresholding technique is based on the calculation within small neighbourhoods throughout the volume. This should be a better method than global segmentation when a large difference of gray levels exists in an image, for example a combination of cortical and trabecular bone. There have been several local thresholding techniques developed to optimize segmentation quality (Dufresne 1998, Elmoutaouakkil et al. 2002, Waarsing et al. 2004).

Region growing is an image segmentation method which searches for connected regions of voxels with similar features, such as voxel intensity and gray level texture. The process of region growing begins through the user specification of initial seed voxels inside the object of interest. Then, selected seed voxels are compared to neighbouring voxels, a region is grown from the seed voxel by adding in similar neighbouring voxels (Clarke et al. 1995, Cendre et al. 2000). This process goes on

until no more voxels can be added to the region. The final region represents the group of voxels that make-up the object of interest. In our study, region growing was used to eliminate unconnected voxels on segmented data.

Edge-based algorithms search for pixels with high gradient values, and then try to connect them to form a curve representing a boundary of the object. Connecting high gradient pixels can be difficult, because in real images they might not be neighbours.

## 2.4 Estimation of Bone Strength

The assessment of trabecular bone strength is important for the diagnosis and the effective treatment of bone metabolic disorders such as osteoporosis. Methods of estimating the strength of the trabecular bone include bone mineral densitometry, trabecular bone morphological analysis, mechanical testing, and finite element simulation. In the following sub-sections the various methodologies to quantify the morphological and mechanical properties of the trabecular bone will be discussed.

### 2.4.1 Bone mineral density (BMD)

In clinical practice, the prediction of bone strength is usually based on areal bone mineral density (aBMD, g/cm$^2$) obtained by DXA. The BMD method provides an estimation of the amount of the mineralized phase (the amount of calcium) in regions of the bones in hip, wrist or vertebrae as these are the common sites of osteoporosis fractures. BMD method provided the basis for the World Health Organization diagnostic criteria for osteoporosis (WHO Scientific Group 2003).

One limitation of DXA is that it measures areal BMD when projected onto a 2D surface, neglecting the third dimension of bone, so that bone specimens with similar mineral density but different thicknesses will give different bone mineral densities. Moreover, it does not measure trabecular and cortical BMD separately. Volumetric BMD determined using quantitative computed tomography (QCT), eliminates this source of uncertainty. However, BMD is a value of material content and cannot reflect pathological variation of trabecular bone structure with disease. Two individuals with identical BMD may have different bone structures and therefore different fracture risks (Marshall et al. 1996).

### 2.4.2 Quantification of trabecular bone structure

Trabecular bone structure has an important role in the determination of bone strength and structural changes are associated with bone pathology (Link et al. 1998a, Majumdar et al. 1998a, Link et al. 1998b, Stone et al. 2003, Felsenberg & Boonen 2005, Lespessailles et al. 2006). There is an increasing body of evidence suggesting a combination of trabecular bone architecture and BMD improves the assessment of trabecular bone strength (Link et al. 1997, Keaveny & Yeh 2002, Mittra et al. 2008). A direct clinical method used to obtain structural information is bone biopsy, which is an invasive, unrepeatable technique and provides information only about the site of sample collection (Gregory et al. 1999).

Using the imaging techniques, parameters characterizing trabecular bone structure, corresponding to the histomorphological measures of trabecular bone can be calculated. The trabecular bone morphological parameters include bone volume fraction (BV/TV, the fraction of the total volume that is occupied by trabecular hard

tissue), trabecular thickness (Tb.Th, evaluated via distance transformation of the 3D binary image and determined by the average diameter of the maximum spheres that fit inside the bone tissue), trabecular spacing (Tb.Sp, the distance between the edges of trabeculae, evaluated by distance transformation of the bone marrow space), and trabecular number (Tb.N, derived as the inverse of the mean distance between the medial axes of bone tissue) (Hildebrand & Rüegsegger 1997, Hildebrand et al. 1999). These architectural measures have been shown to improve the density-elastic modulus correlations as they provide additional information on the structural orientation of the bone tissue (Ulrich et al. 1999).

Newitt et al. (2002) studied the effect of trabecular bone micro-architecture on bone mechanical properties in the distal radius, and found that the correlation between the mechanical measures (such as the elastic modulus and the shear moduli) and trabecular bone structure measures were higher than the correlation between them and the bone mineral density in the determination of bone strength.

The morphological parameters of the trabecular bone and volumetric BMD can be calculated to provide an estimation of bone strength by determining bone quantity, structure, and shape. However, the morphology study could not fully explain the variation of trabecular bone apparent stiffness and strength, because these mechanical properties depend on both bone architecture and bone mineral content.

### 2.4.3 Characterization of trabecular bone mechanical properties

From the biomechanical viewpoint, trabecular bone is a *heterogeneou*s and *viscoelastic* material. It is also an *anisotropic* material; its mechanical properties differ with direction. Trabecular bone behaves differently in compression and in tension (Keaveny et al. 2001). Its strength is also greater longitudinally than in the radial and transverse directions. Since trabecular bone is a biological material, its properties vary with time and are influenced by other factors, including age, sex, and state of health of the individual. The heterogeneity of trabecular bone is manifested in a wide variation in the mechanical properties across anatomical sites. This heterogeneity results from fundamental variations in bone volume fraction, architecture and tissue material properties and leads to differences in mechanical properties (Keaveny et al. 2001). Some alteration in mechanical properties of the trabecular bone can be attributed to functional adaptation, as specified by Wolff's law (Cowin 2001).

The mechanical properties of trabecular bone can be characterized at two levels: the tissue level properties, and the apparent level properties. The *tissue properties* of trabecular bone refer to properties evaluated at the level of individual trabecula (i.e. the intrinsic bone materials properties only) and are not influenced by its geometry. The *apparent properties* refer to properties measured at the continuum level of a whole trabecular bone (i.e. properties arising from the trabecular bone tissue properties and architecture). Human trabecular bone specimens behave as a continuum material when the bone samples are on the order of 5 – 10 mm in diameter or edge-length (Harrigan et al. 1988). As trabeculae are typically 100 μm – 300 μm thick in human bone, and are separated by larger marrow spaces

of 500 µm – 1000 µm (Morgan et al. 2004, Ün et al. 2006), specimens greater than 4 mm in diameter exhibit apparent properties (Harrigan et al. 1988, Homminga et al. 2002, Keaveny & Yeh 2002). Two common methods of measuring bone mechanical properties are mechanical testing and virtual mechanical testing or computational simulation in the form of finite element analysis (FEA). Both methods were used in this project and are described in more detail later.

#### 2.4.3.1 Mechanical test

The mechanical testing techniques, such as tensile, bending and compressive tests, are the "gold standard" for the mechanical assessment of whole bone or pure bone samples, such as individual trabeculae or cortical bone. When a compression load $F$ is applied to an object with a length $L$ and a cross-sectional area $A$, the load produces stress $\sigma$. The stress at a specific point is defined as:

$$\sigma = \lim_{\Delta A \to 0} \frac{\Delta F}{\Delta A} = \frac{dF}{dA} \tag{2.20}$$

The unit of stress is pascal (Pa= N/m²). The applied load $\Delta F$ produces a deformation $\Delta\delta$. The strain $\varepsilon$ at the specific point is defined by considering a small element of undeformed length $\Delta x$. The deformation $\Delta\delta$ of the element under the given load defines the normal strain at that point as follows:

$$\varepsilon = \lim_{\Delta x \to 0} \frac{\Delta \delta}{\Delta x} = \frac{d\delta}{dx} \tag{2.21}$$

Strain is dimensionless. The relationship between the applied stress to a structure and the resulting strain in response to stress can be described by stress-strain curve, as shown in Figure 2.7.

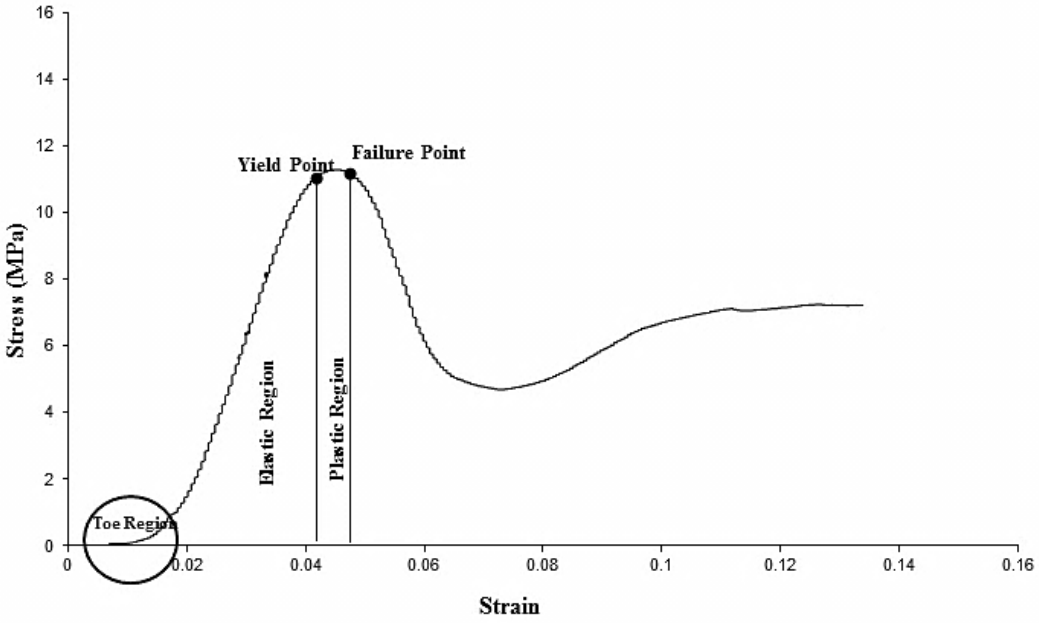


**Figure 2.7** Typical stress-strain curve of a core sample of the trabecular bone from the bovine proximal femur, under uniaxial compressive testing.

The stress-strain curve of trabecular bone (Figure 2.7) shows two regimes of behaviour (elastic and plastic). Initially, trabecular bone displays an approximately linear-elastic response to low stress with a subtle concave downwards nonlinearity (toe region) in the elastic region (Keaveny et al. 1994, Morgan & Keaveny 2001, Bayraktar et al. 2004a). The toe region, the so called 'end-artifact', originates from the damage incurred at the ends of the machined specimen and is mostly due to the upper and lower surfaces of a bone sample not being perfectly parallel in a simple platen-type compression test, producing a nonlinearity. This effect can be minimized using suitable experimental techniques.

The slope of the "most linear" portion of the curve is defined as *Young's modulus* (*E*) or the *elastic modulus*, representing the inherent stiffness of the sample. Morgan et al. (2001a) proposed that elastic modulus measurements be based on the initial

slope of a second-order polynomial fitted to the portion of the curve from 0 - 0.2% strain. They found that this choice minimized the variation in measurements among many samples. A reasonable first approximation to a mechanical model of the bone is to consider it as an anisotropic, linear elastic solid with Hooke's law as the appropriate constitutive equation:

$$\sigma_{ij} = C_{ijkl}\varepsilon_{kl}, \tag{2.22}$$

where $\sigma_{ij}$ and $\varepsilon_{kl}$ are the stress and infinitesimal strain tensors, respectively, and $C_{ijkl}$ is the fourth-order stiffness tensor or elasticity tensor. Using the reduced notation, the Equation 2.22 can be rewritten as:

$$\sigma_{ij} = C_{ij}\varepsilon_j , \quad \text{i, j = 1 to 6} \tag{2.23}$$

where $\sigma$ and $\varepsilon$ are the second order stress and infinitesimal strain tensors written as vectors, and $C$ is the stiffness matrix.

The mechanical material constants: elastic modulus, Poisson's ratio, and shear modulus are obtained from the compliance matrix $\boldsymbol{S}$, based on the inverse of the constitutive equation given by (2.22):

$$\varepsilon_i = S_{ij}\sigma_j, \tag{2.24}$$

$$\text{where } [S_{ij}] = \begin{bmatrix} 1/E_1 & -v_{21}/E_2 & -v_{31}/E_3 & 0 & 0 & 0 \\ -v_{12}/E_1 & 1/E_2 & -v_{32}/E_3 & 0 & 0 & 0 \\ -v_{13}/E_1 & -v_{23}/E_2 & 1/E_3 & 0 & 0 & 0 \\ 0 & 0 & 0 & 1/G_{23} & 0 & 0 \\ 0 & 0 & 0 & 0 & 1/G_{31} & 0 \\ 0 & 0 & 0 & 0 & 0 & 1/G_{12} \end{bmatrix} \tag{2.25}$$

and $G$ is shear modulus (or modulus of rigidity), $E$ is elastic modulus, and $v$ is Poisson's ratio. In the case of an orthotropic material the symmetry of the $\boldsymbol{S}$ tensor implies that:

$$\frac{v_{12}}{E_1} = \frac{v_{21}}{E_2}\,, \quad \frac{v_{13}}{E_1} = \frac{v_{31}}{E_3}\,, \quad \frac{v_{23}}{E_2} = \frac{v_{32}}{E_3}\,, \tag{2.26}$$

meaning only 9 of the 12 non-zero terms in the Equation 2.24 are independent. Furthermore in the transversely isotropic case, material symmetry imposes that:

$$E_1 = E_2 = E_3, \qquad v_{12} = v_{21}, \qquad v_{31} = v_{32} = v_{13} = v_{23},$$

$$G_{23} = G_{31}, \qquad G_{12} = \frac{E_1}{2(1+v_{12})} \tag{2.27}$$

Thus, the number of independent coefficients reduces to 5.

The linear-elastic region ends where yielding is initiated and beyond this point, irreversible plastic deformation occurs. Beyond the yield point, there is a non-linear increase in stress with increasing strain until ultimate stress is reached. With further strain, stress decreases due to progressively more trabeculae becoming damaged and fractured. The fractured trabeculae fill the marrow spaces as the tissue compacts. When most of the pore spaces are filled with fractured trabeculae, a noticeable increase in stiffness occurs (Cordey & Gautier 1999, Bayraktar & Keaveny 2004).

The apparent elastic modulus is often used to describe the mechanical properties of trabecular bone (Keaveny et al. 1997, Keaveny et al. 2001). It was found to be age-, sex-, and anatomic site related but well correlated with density and morphological parameters (Kabel et al. 1999, Mittra et al. 2005). Trabecular bone yield stress and strain are used to characterize the failure behaviour. The yield stress and strain are defined at the yield point, commonly located at the intersection of the strain-stress curve and a line parallel to the linear portion of the strain-stress curve and offset by 0.2% strain (Turner 1989, Keaveny et al. 1994). The elastic modulus and yield stress

are linearly dependent on bone volume fraction, while the yield strain is not dependent on variation in volume fraction and architecture (Kopperdahl & Keaveny 1998). Trabecular bone yield strain was found to vary across anatomic sites but was uniform within a site (Morgan & Keaveny 2001), and it was isotropic for bovine trabecular bone (Chang et al. 1999).

#### 2.4.3.2 Strain gauge measurement

In biomechanics, the effects of mechanical load on the bone tissue can be measured as strain at selected locations by strain gauges attached to the bone surface. A common strain gauge is composed of a metal wire grid encapsulated between two thin protective sheets. As the gauge wire is strained, its resistance ($R$) changes according to:

$$R = \rho L/A, \tag{2.28}$$

where $\rho$ is resistivity of the wire, $L$ is length of the wire, and $A$ is its cross-sectional area. Thus, as the wire is stretched, the increase in $L$ and the decrease in $A$ act to increase the resistance. This change in resistance is proportional to the applied strain.

The strain gauge measurements are the most common direct way *in vitro* to measure the stiffness and the apparent strain of bone (Cordey & Gautier 1999, Fritton et al. 2000, Ryoyama et al. 2004, Talaia et al. 2007). A major advantage of using strain gauges is that they can accurately measure local strains directly, without altering the state of the host material. Moreover, they can be monitored continuously in dynamic loading situations. The main disadvantage of strain gauges is that they measure strain

only at discrete points. Therefore, one must have a good idea of the regions of interest in the specimen prior to gauge attachment and testing. *In vivo* applications of this technique have obvious limitations. The preparation of a bone to insert the strain gauges involves an invasive surgical procedure (Arndt et al. 1999). Besides, there is a limited access to the area of interest such as the femoral neck.

By contrast, non-invasive image modalities provide anatomically valid structural data that, together with information on mechanical properties of tissue, might be used to simulate the effect of mechanical loading. Finite element (FE) method based on medical image datasets potentially offer a clinical tool for the non-invasive, non-destructive and repeatable evaluation of the mechanical properties of bone (Charras et al. 1999, Borah et al. 2001, van Rietbergen 2001, Stolk et al. 2002, Crawford et al. 2003, Shahar et al. 2003, Li & Wang 2006, Muller & Harry van Lenthe 2006, Schileo et al. 2008, Cristofolini et al. 2010, Pal et al. 2010, Varghese et al. 2011).

#### 2.4.3.3 Finite element method

As an alternative to mechanical testing, computer simulations with finite element analysis have begun to be applied to estimate the mechanical behaviour for an object with a complex geometry like the trabecular bone structure under virtual mechanical loading. FE method is a powerful tool for complex biomechanical problems. It predicts whole bone stiffness, fracture progression, and load sharing between cortical and trabecular bone, which are difficult to obtain using experimental studies (Buckley et al. 2007, McDonnell et al. 2009). As opposed to experimental testing, numerous specimens are not required, and several loading scenarios and implant designs can be simulated relatively easily. FE method is able to predict in situ stress

and strain distribution in trabecular bone structure under physiological loading conditions (van Rietbergen et al. 1999, Keyak & Rossi 2000, Keyak & Falkinstein 2003, Laz et al. 2007).

FE modelling is a numerical method which uses simple shapes, known as elements, to form complex geometric structures. The elements are assembled together at nodes and along edges to form the overall structure. Material properties, boundary and interface conditions, and loads of the actual problem can be incorporated into the meshed model. The next step after model creation is model solution. The equations that govern force equilibrium at each node are solved to obtain a solution, for example, in the form of the nodal displacements resulting from the applied loads and constraints. The system of equations is given by:

$$K\boldsymbol{u} = \boldsymbol{F}, \tag{2.29}$$

where $K$ is the global stiffness matrix which is assembled from the stiffness matrices of each element, $\boldsymbol{u}$ is the global vector of nodal displacement, and $\boldsymbol{F}$ is the global vector of nodal forces. The size of the stiffness matrix is related to the number of nodes and degree of freedom at each node. For a problem with $N$ nodes with three degrees of freedom per node, the global $K$ is of size ($3N\times3N$), while the global $\boldsymbol{u}$ and $\boldsymbol{F}$ vectors are of size ($3N\times1$), as follows:

$$\begin{bmatrix} K_{11} & K_{12} & K_{13} & \cdots & K_{1,3N} \\ K_{21} & K_{22} & K_{14} & \cdots & K_{2,3N} \\ \vdots & \vdots & \vdots & \ddots & \vdots \\ \vdots & \vdots & \vdots & \ddots & \vdots \\ \vdots & \vdots & \vdots & \ddots & \vdots \\ \cdots & \cdots & \cdots & \cdots & K_{3N,3N} \end{bmatrix} \begin{bmatrix} u_{x1} \\ u_{y1} \\ u_{z1} \\ u_{x2} \\ \vdots \\ u_{yN} \\ u_{zN} \end{bmatrix} = \begin{bmatrix} F_{x1} \\ F_{y1} \\ F_{z1} \\ \vdots \\ F_{yN} \\ F_{zN} \end{bmatrix} \tag{2.30}$$

The stiffness matrix $K$ is related to both geometry and material properties of the FE model and the matrix can be written as:

$$K = \int B^T EB dV, \tag{2.31}$$

where $B$ is the strain matrix related to shape function of each nodal point in an element, $E$ is the stress-strain matrix which is related to material properties of the model, and $dV$ is the volume change of an element.

#### 2.4.3.3.1 Geometry and mesh consideration

The first challenge with generating FE model is to accurately define the geometry of the domain to be meshed. The geometrical or solid model of an object may be obtained in many ways. Currently, CT or MR images provide accurate input data for a variety of software that will produce a solid model of the object. The next step is dividing the structure into small elements. The computing time required to solve a model depends on the number and type of elements. The solution of the model will converge to the exact solution as the mesh density approaches infinity. Thus, the accuracy of the model can be checked by using the convergence test, where the mesh is refined until results stabilize. It should be noted that the convergence test assesses accuracy only in terms of the closeness of the solution to the expected theoretical values for the defined parameters. The validity of the model, also depends on accurate geometry, material properties, loading and boundary conditions (Steele 1989, Adams & Askenazi 1999).

The solid elements of a mesh may be based on tetrahedral or hexahedral elements, which are usually first-order (linear) or second-order (quadratic). Second-order elements have mid-side nodes, which allow curved boundaries that can approximate irregular geometry more closely than straight-sided first-order elements. Tetrahedral elements can have 4-nodes (first-order) or 10-nodes (second-order) in terms of

degrees of freedom. The hexahedral elements have more degrees of freedom than tetrahedral elements, 8-nodes for first-order and 20-nodes for second-order.

Some studies have focused on the development of rapid and automated mesh generator algorithms which are able to obtain accurate results (Muller & Ruegsegger 1995, Viceconti et al. 1999, Viceconti et al. 2004). The mesh generation schemes used in the studies of trabecular bone were either geometry-based or voxel-based. In the geometry-based meshing, the CT or MR scan dataset must be pre-processed to extract the surface of bone. Then, elements are defined on the surface. A full 3D set of elements is usually obtained by propagation from the surface. The surface of trabecular bone is complex (Figure 2.1) and may be difficult to define.

On the other hand, voxel-based meshing is generated by converting a voxel or several adjacent voxels directly into an eight-node brick element. Because it bypasses the step of defining the surface, it can be fast and fully automated. However, voxel elements may lead to jagged edges which result in errors in the computation of local stress and strain distribution near boundaries (Guldberg et al. 1998). Les et al. (1997) demonstrated that while there is a correlation ($0.69 < r < 0.90$) between the surface strain of voxel models and the measured surface strains in the strain gauge experiment, the models tended to overestimate the strain magnitudes. Some studies focused on providing smooth surface meshing for FE models (Camacho et al. 1997, Charras & Guldberg 2000, Wang et al. 2005). A method was introduced that produces a smooth mesh generation automatically from CT data (Viceconti et al. 1999). The method uses Hexar program which obtains a tiled surface of hexahedral elements which correctly connect and share the vertex and bounding edges. They demonstrated improved accuracy in the prediction of

stress using this model. Muller and Ruegsegger (1995) introduced a method that uses the volumetric marching cubes algorithm creating a tetrahedral mesh with smooth surfaces from image voxels. Nevertheless, the mesh generation time is much higher than a direct transfer from the CT or MR voxels to the hexahedron elements. Boyd and Muller (2006) used a smooth surface meshing model for FE modelling and concluded that the computational time increases linearly with the number of smoothing iterations and the number of smoothed elements.

Lengsfeld et al. (1996) compared geometry-based and voxel-based mesh modelling of human femur and found a good agreement between the FE solutions obtained with the two models. They also introduced a geometry-based modelling to create 3D models of human femora and found that generation of the models appears still rather time-consuming and requires a significant human effort.

Viceconti et al. (1998) did a comparison between several techniques of obtaining viable meshes (mapped, tetrahedral, hexahedral and voxel meshes) for the human femur, in order to evaluate advantages and limits in terms of geometric adaptability, accuracy of the result and computational cost. The mapped meshing is a manual procedure that decomposes the solid model into hexahedral elements. It needs extensive intervention by expert operator, but can be very accurate. The tetrahedron meshing which automatically generates linear (4-node) or quadratic (10-node) elements is widely available and accurate, and offers probably the best method for the solid model. The hexahedron meshing uses the linear (8-node) hexahedral elements to define the boundary of the solid model and it results in the tiled surface. This meshing model produced the most accurate results but was slow and required significant computational resources, due to a high number of elements and more

degrees of freedom for the nodes in the model. The voxel meshing, which creates elements directly from the CT data set, was the easiest and fastest but required a huge number of elements for the complex shapes such as the trabecular bone to reach accuracy comparable to other methods.

Ulrich et al.(1998) investigated the effect of μCT image resolution (28 μm and 168 μm) and different mesh cells (hexahedron, compensated hexahedron and tetrahedron) on the results from FE analyses of trabecular architecture, and found that the accuracy of the results of FE model based on images with a resolution of 168 μm (highest available *in vivo* resolution) depended on the trabecular morphology, especially its thickness. In addition, the plain hexahedron mesh resulted in a substantial loss of connected bone tissue and a subsequent loss of stiffness. The tetrahedron and compensated hexahedron (a modification of plain hexahedron) methods produced more accurate results, because both reduced the loss of trabecular connections. The tetrahedral models could model trabecular connections that were smaller than the voxel size of the images, and generated a smooth surface which lead to more accurate results, but its computational cost was much higher than the other models.

Saxena & Keller (1999) and Coleman et al. (1999) compared hexahedral and tetrahedral elements and concluded that the accuracy of tetrahedral mesh was superior but its model generation was more difficult than the hexahedron mesh. Crawford et al. (2003) compared voxel-based FE models with bone mineral density derived from a QCT dataset in the prediction of vertebral body strength and demonstrated that voxel-based FE models were better predictors than clinical measurements of bone mineral density.

Although most of these studies have shown that tetrahedral meshes are sufficiently accurate for most biomechanical studies, the creation of the three-dimensional solid model of a bone segment from CT or MRI data is a complex and time-consuming procedure. Therefore, automatic mesh generation methods based on voxels are of interest and have begun to be considered in virtual biomechanical studies of human bone.

#### 2.4.3.3.2 Geometric linearity and non-linearity

The choice of the order of the equations for FE solvers is dependent on the expected deformation of an object. Linear FE formulation is based on the assumption that element displacement and strain is small. Its computational cost is much lower than the cost of a non-linear FE analysis. Moreover, the stiffness matrix of the system is constant. In linear analysis, the structure has elastic behaviour. On the other hand, a non-linear approximation models large deformations accurately. The stiffness matrix is no longer constant and the behaviour of the structure can be modelled beyond the elastic limit (Adams & Askenazi 1999) .

The non-linear problems in solid mechanics have been classified into three main types: material non-linearity, in which the stress-strain relationship is non-linear, geometric non-linearity, in which a structure has a large deformation due to its displacement under loading and the changing geometry of the structure considers in analysing its behaviour, and boundary non-linearity in which the displacements and stresses of the contacting bodies are not linear.

Bayraktar (2006) investigated the role of geometrical non-linearities in trabecular bone mechanical behaviour and concluded that since the effects of geometric non-linearities cause softening in compression and stiffening in tension, the incorporation of this non-linear mechanical behaviour of trabecular tissue in micro-FE models is necessary to assess the mechanical behaviour of trabecular bone accurately.

Stolken & Kinney (2003) studied the effect of geometrically linear and non-linear analyses in the results of FE modelling of trabecular bone for two different material models, a plastic damage model and a brittle damage model, and found that non-linear terms must be included in the total stiffness matrix to obtain accurate results. In addition, trabecular bone is a geometrically non-linear structure and linear analysis cannot accurately simulate its failure.

Linear elastic FE models cannot simulate failure behaviour of bone but they are widely used to determine bone tissue elastic properties. Non-linear FE models are employed rarely due to their complexity and computational cost.

#### 2.4.3.3.3 The effect of resolution and element size

Resolution is defined as the ability to differentiate two small high contrast features located a small distance apart in an image. The tradeoff between image resolution and the computational effort in FE simulations has to be considered. A studying of mesh convergence (van Rietbergen et al. 1995) found that solving a model with 40 μm voxel size resulted in <2% difference in the stress and strain histograms when compared to a model with 20 μm voxel size. This result indicates that 40 μm voxel

model was sufficiently accurate, while the computational effort was reduced by a factor of eight.

Bevill and Keaveny (2009) found that the elastic modulus and yield stress predictions from the FE analysis based on CT image at voxel sizes of 40 μm and 80 μm were highly correlated with yield stress from the 20 μm models. Keyak and Skinner (1992) used three different sizes (3.1 mm, 3.8 mm and 4.8 mm) of hexahedral elements for FE modelling based on CT images of human proximal femur. The results demonstrated that with the increase in element size from 3.1 mm to 3.8 mm, the predicted stresses decreased by 13% to 29% overall, and strains decreased by 4% to 20%.

Van Rietbergen et al. (1995) analysed trabecular bone structure and found that the apparent Young's modulus dropped 19% when the mesh element size increased from 20 μm to 100 μm. Pistoia et al. (2001) found that 165 μm *in vitro* HR-pQCT image data of distal radius in human cadavers, which is approximately the thickness of human trabeculae, were sufficient for measuring apparent and tissue level properties of trabecular bone, with correlation of $r^2 > 0.95$ for apparent level results and $r^2 > 0.83$ for tissue level results. In modelling mechanical behaviour of trabecular bone, different element sizes (0.08 mm, 0.64 mm and 3.04 mm) were compared and it was found that there was less than 5% difference in predicted yield loads and stiffness from the coarsest models (0.64 mm and 3.04 mm) with reference model (0.08 mm) results (Verhulp et al. 2006).

More recently, the effect of voxel size (16.4 μm, 82 μm, 164 μm, 328 μm and 488 μm) on strain patterns in cortical shell was investigated through FE modelling

based on CT images (Mueller et al. 2011). They found that, compared to 16.4 μm voxel, voxel size of 488 μm (similar to their available clinical CT scanners) resulted in overestimating bone thickness in thinner specimens and also more jagged edges, both of which influenced the results of FE analysis and caused a great reduction in maximum principal strains. In the evaluation of the effect of resolution and element size on the results of FE analysis in the prediction of trabecular bone mechanical properties, all studies used CT image-based FE models and none investigated this effect for MRI-based FE models.

### 2.4.4 Validating FE models

Predictions by FE analysis of the fracture load in animal and human bones have been successfully validated experimentally (Keyak et al. 1993, Bessho et al. 2007, Chevalier et al. 2007, Wolfram et al. 2010). Experimental tests were used to measure apparent level results from animal and human bone samples with different loading conditions mimicking daily activities. For example, a human metacarpal model was tested under both torsion and combined axial/bending loading conditions (Barker et al. 2005). Strain gauges were mounted on the cortical bone to measure local strains. The corresponding FE models included half of the metacarpal bone by assuming symmetrical geometry in the metacarpal sample. The FE cortical strain results were validated well with correlation coefficients greater than 0.95 in torsion results and 0.84 in combined axial/bending testes. But strains in individual trabeculae were not measured and could not be validated directly in these cases because strain gauges could not be mounted on intact trabecular tissue. Also, these validations were for

loading consistent with normal daily activity, so fracture and yield stress and strain were not known.

At the local level, Guldberg et al. (1998) applied a hexahedron mesh for the FE model of a circular cantilever beam, in bending tests using analytical calculations to validate the FE results. When averaging over three to four elements through the beam cross section, they reported the relative error of $\leq 4\%$. The disadvantage of the analytical validation is that, in practice, it can only be used for simple models. Validations on realistic trabecular bone models are not possible by this method.

An alternative and novel approach to validate failure criteria on trabeculae is image guided failure assessment (IGFA) which captures trabecular bone microstructure local deformation and failure in sequential μCT images. A compression testing device was placed in a μCT or μMRI scanners so those modalities could record step-wise micro-compression testing results on the trabecular bone during in situ compression tests (Müller et al. 1998, Benoit et al. 2009). The step-wise results have high correlation with the classical continuous testing ($R^2 = 0.98$) (Nazarian & Müller 2004). This method was used for validation of FE simulation on not only local failure criteria, but also the micro-damage initiation of the trabecula at the tissue level (Nagaraja et al. 2005). These studies found that significantly higher local stresses and strains were measured in the damaged trabecular microstructure than undamaged trabecular microstructure. This might indicate the difference in the local tissue mechanical properties between healthy and unhealthy bones. However, the damage area was quantified on 2D histology sections so that errors were expected when using a 2D data to estimate a 3D sample. The IGFA method might be able to

extend the measurement of local stress and strain by recording tissue deformation in time-lapsed measurements. 3D image correlation technique was used to quantify and estimate 3D displacement fields in bone or solid foam (Verhulp et al. 2004, Zauel et al. 2006, Benoit et al. 2009, Dickinson et al. 2011). Image registration is often used in longitudinal studies to track disease development and treatment progress. Image registration technique aligns images acquired at different times, obtained with the same or with different modalities. Mechanical and morphological measurements from µMR, HR-pQCT and µCT were compared and quantified by image registration technique (Newitt et al. 2002a). Li et al. (2006) applied an image registration technique to CT images of proximal femur in astronauts before and after a long duration spaceflight. Bone loss was studied and visualized directly at a sub-regional level. In our study, image registration technique was used to validate the results of FE analysis.

### 2.4.5 Previous MRI-based FE models and motivation of the current study

FE analysis based on µMRI (with voxel dimensions of 195 µm in-plane and slice thickness of 500 µm) of calcaneal trabecular bone from post-menopausal women, who had been treated with drugs for osteoporosis in the preceding 12 months, showed significant changes in estimated anisotropic elastic modulus despite undetectable changes in BMD or bone volume fraction (van Rietbergen et al. 2002). The feasibility and potential of using MRI-based FE modelling was demonstrated in the study of osteoporosis (Newitt et al. 2002). They scanned the distal radius with a 1.5 T µMR scanner with voxel dimensions of 156 µm in-plane and slice thickness of 500 µm. Benoit et al. (2009) used a FE model based on µMRI with an isotropic

voxel size of 78 µm to determine 3D displacement and strain fields of trabecular bone during an in situ compression test. Two *in vivo* MRI data sets, one with an isotropic voxel size of 160 µm, the other with voxel sizes of 137 µm in-plane and 410 µm slice thickness were used to estimate structural parameters and elastic modulus of trabecular bone from distal tibia (Wald et al. 2010). It was found that the lower signal-to-noise ratio of the isotropic voxel image was reflected in a significantly different structural parameter measurement. The reproducibility of measurements based on the model with the larger anisotropic voxel size was higher than that with the isotropic voxel. Rajapakse et al. (2010) found that FE model based on µMRI at an isotropic voxel size of 160 µm could estimate mechanical parameters such as stiffness, elastic moduli, and shear moduli of bone in the distal tibia and these were highly correlated ($r^2$= 0.85) with those derived from FE model based on µCT image with an isotropic voxel size of 25 µm.

These studies indicate that high resolution MRI-based FE method is valuable for monitoring the efficacy of bone disease treatment. Also, mechanical properties such as strain/stress fields from detailed microstructures of the trabecular bone can be estimated using µMRI-based FE analysis (Benoit et al. 2009). However, this technique has been limited to high resolution MR images and is most often performed at peripheral sites such as the distal tibia, the distal radius, and the calcaneus where osteoporotic fractures are less common than in the proximal femur and the spine. Imaging of the proximal femur and the spine requires whole-body MRI scanners.

The potential of whole-body MRI-based FE model to estimate mechanical properties and stress/strain distributions of trabecular bone at these anatomic sites has not been investigated. In addition, no study has been reported on the effect of MR voxel size, especially in images obtained at clinical resolution, on the results of FE estimation of apparent mechanical properties of trabecular bone. The effect of MR voxel dimensions on the accuracy of trabecular bone morphological parameters has been investigated in previous studies. One recent study (Kim et al. 2012) evaluated this effect and determined the acceptable isotropic voxel size (up to 230 μm) for accurate structural analysis of trabecular bone. However, the effect of different physical MR voxel sizes on the mechanical parameters of trabecular bone has not been investigated.

In order for a whole-body MRI-based FE analysis to be considered a clinical tool for assessing the bone mechanical properties, it must be thoroughly validated and compared with the high resolution MRI or CT. Mechanical properties, such as apparent stiffness, apparent tissue elastic modulus and displacement fields, obtained by whole-body MRI-based FE should be compared to μMRI-based FE analysis results.

# Chapter 3: Materials and Methods

## 3.1 Introduction

The broad aim of this study is to investigate the potential of whole-body MRI-based finite element modelling to predict displacement fields of trabecular bone, and also to assess the impact of resolution on displacement fields through FE modelling. The following tasks were undertaken to achieve the specifics aims of the study as outlined in section 1.2:

(1) fabrication of a compressive mechanical testing device capable of loading a physical phantom or trabecular bone samples during acquisition of μCT images.

(2) estimation of tissue effective elastic modulus using FE analysis based on μCT images of the physical phantom or the trabecular bone specimens and validation of the accuracy of FE model by comparison of the results of FE analysis with mechanical testing results.

(3) estimation of tissue effective elastic modulus using FE analysis based on μMR images of the trabecular bone specimens and assessment of the FE model accuracy by comparison of the results of FE analysis based on μCT images.

(4) estimation of displacement fields using FE analysis based on μMR images of the trabecular bone specimens and evaluating the accuracy of FE model by comparison of the results of FE analysis with μCT-based FE results.

(5) estimation of displacement fields using FE analysis based on whole-body MR images of the trabecular bone and assessment the FE model accuracy by comparison of the results of FE analysis with μMR-based FE results.

(6) estimation of displacement fields using FE analysis based on μMR images of the trabecular bone with various voxel sizes and determination of acceptable image voxel size.

## 3.2 Development of a Compressive Mechanical Loading Chamber

In order to visualise the response of the trabecular bone to external stimuli during a compressive test and reveal local deformations, estimate high stress/strain regions, a small compressive mechanical loading chamber (mini-jig) was built (Figure 3.1) and validated in μCT. Criteria for the design of the mini-jig included:

1. must fit within the micro-CT system.
2. must generate uniaxial compressive displacements.
3. must measure and record in real-time the compressive applied force on specimens.
4. must contain a physical phantom with dimension of 16 mm × 12 mm × 32 mm, and trabecular bone specimens less than 9 mm in diameter, and length double the diameter.
5. must be a radiolucent window for micro-CT imaging.
6. must prevent damage to the specimen on insertion and removal from the system

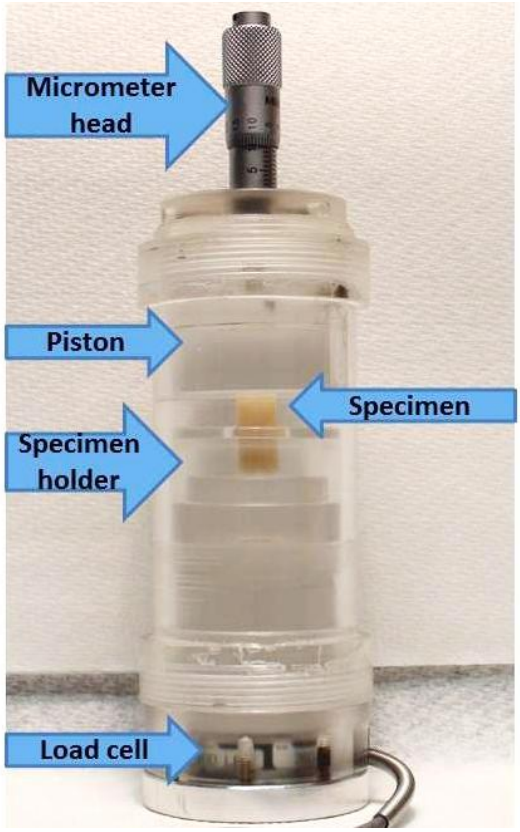


**Figure 3.1** The compressive mechanical loading chamber (mini-jig).

The system design was based on Nagaraja et al. (2005) study. This system applied stepwise uniaxial strains to the specimen and was designed to fit within the micro-CT system. The uniaxial strains were applied using a micrometer head (Series 148 Mitutoyo Corp. USA) with a displacement resolution of 0.01 mm. A custom polycarbonate piston translated micrometer displacement into specimen strain. A spherical face at the end of the micrometer shank mated with a stainless steel ball integrated into the piston; thus, rotation of the micrometer head did not apply torque to the piston or the sample. A 100 N load cell (Model MLGLE-100, Entran, USA), with dimensions small enough to fit inside the base of the chamber, measured applied force on a phantom. It was replaced with a high capacity (2224 N) load cell (Model LBC-500, Transducer Techniques, USA) for the compression testing of the

trabecular bone samples. The housing of micrometer head, piston, specimen and load cell consisted of a stiff polycarbonate body with a radiolucent window for x-ray penetration through the specimen during μCT imaging. The overall dimensions of the jig, 18 cm in length and 5 cm in diameter were chosen to meet the spatial restriction of the μCT bore. For the load ranges in this study, polycarbonate housing compliance was calculated to be less than 10% of the maximum applied displacement. It also was calculated and considered for each load step.

## 3.3 Physical Phantom

In order to assess the accuracy of the μCT-based FE methods, two types of solid materials, a physical phantom and vitro trabecular bone, were used. The physical phantom was manufactured by ARRK company (Arrk Australia & New Zealand Pty Ltd,5 Lynch Street Hawthorn VIC 3122, now known as 3D Systems Asia-Pacific) from a CAD model of a related study (Nikro 2008). The structure of the phantom was modelled by a rectangular lattice of cylindrical beams (Figure 3.2) and represented a simplified trabecular bone structure. The phantom's material was Objet's FullCure 720, an acrylic-based photopolymer, and its tissue elastic modulus was 2870 MPa. The dimensions of the phantom were 16 mm × 12 mm × 32 mm. The apparent elastic modulus of the phantom was determined by a mechanical platen test in-camera (in-situ for μCT imaging) using the mini-jig described in section 3.5.1.

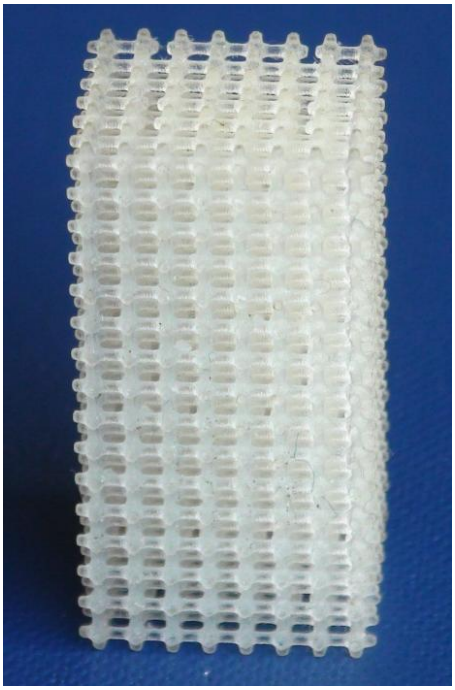

**Figure 3.2** The manufactured phantom has the form of a rectangular lattice of cylindrical beams and the dimensions of 16 mm × 12 mm × 32 mm.

Due to the simple rod-like structures in this model, unlike in real trabecular bone structure, the meshing and FE analysis of the phantom imaged made relatively modest demands of the computational storage and processing resources.

## 3.4 Trabecular Bone Preparation and Mechanical Testing

### 3.4.1 Trabecular bone sample preparation

Due to its availability, young bovine bone has been commonly used in bone studies. The proximal part of a bovine femur (approximately 2 years old) was obtained fresh from a local butchery shop. Slabs from the femoral head were cut using a bone saw to expose trabecular bone. The first cut was made about 5 mm from the proximal tip of the femoral head in a plane perpendicular to the superior-inferior main trabecular

direction (MTD). The second cut was performed parallel to the first plane, producing a 21-mm thick bone slab (Figure 3.3).

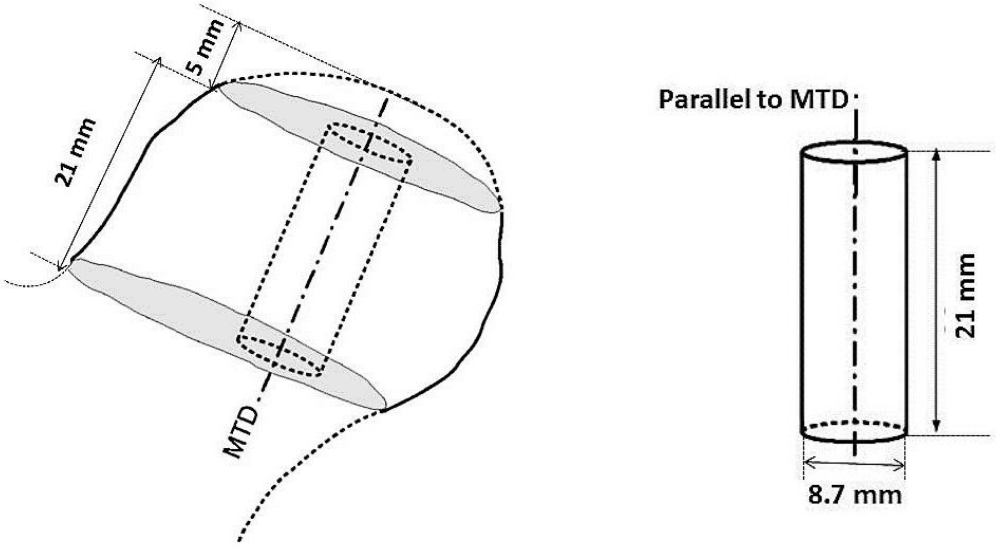


**Figure 3.3** The outline of a femoral head, showing the 21-mm thick bone slab with end planes perpendicular to MTD (left). The bone slab was cut out from the head, and then cylindrical cores were drilled out from the slab. The extracted trabecular bone cylinder was 8.7 mm in diameter and 21 mm in height (right). (Adapted from Perilli, Baleani et al. 2008).

The cylindrical bone samples of 8.7 mm in diameter with the axis parallel to MTD were extracted from the bone slab with a diamond-coated coring drill (Starlite Industries, Inc. USA) attached to a drill press (Model SPD 30, Hafco Metalmaster). The coring step was carried out under constant water irrigation. Both end-surfaces of cores were ground down to give the required core length (17.4 mm), and polished using a low-speed polisher (Model Forcipol 1V, Kemet Int. Ltd., UK) and a grinding paper (with a grit size of 800 μm). When not in use during the preparation, the bone samples were constantly irrigated in the bath of phosphate buffered saline (PBS) (pH 7.4) to minimize bone damage due to drying or heating and to preserve the bone properties. Twenty cylindrical trabecular bone specimens of length 17.4 mm and

8.7 mm in diameter were prepared (Figure 3.4). Their dimensions followed the 2:1 length to diameter ratio suggested by Keaveny et al. (1993).

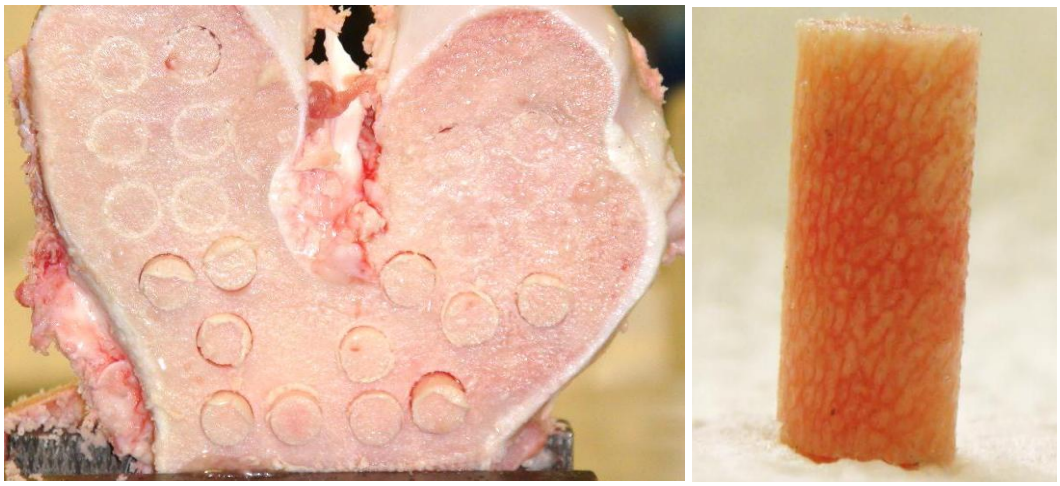

**Figure 3.4** The surface of the bovine bone slab with cored cylindrical bone samples in situ (left), and a trabecular core with diameter of 8.7 mm and length of 17.4 mm (right).

Of the 17 specimens, two (A and B) were arbitrarily selected for image acquisition in µMRI, clinical MRI and µCT scans. Remaining specimens were used for destructive mechanical testing in order to estimate the linear elastic region, failure point, stiffness and apparent elastic modulus. This was used to guide the setup of strain steps in the in-camera compression tests on the imaged samples. The specimens stored in PBS at -20ºC and were thawed in the saline solution at room temperature (21ºC) for approximately three hours prior to use. The freezing and thawing are unlikely to affect the mechanical properties of the specimens. Borchers et al. (1995), Kang et al. (1997), Hongo et al. (2008) have subjected bone sample to multiple thawing-freezing cycles, and reported negligible effects on bone mechanical properties.

### 3.4.2 Mechanical testing

Two types of mechanical testing, platen test and end-cap test are commonly used for testing the mechanical properties of trabecular bone. In the end-cap method, the trabecular core is held (usually with glue) in end-caps and core deformations are measured using an extensometer attached to the end-caps. This type of test was reported to be accurate and particularly suitable for relatively large specimens (Odgaard & Linde 1991, Keaveny et al. 1994, Nagaraja et al. 2005). There are several disadvantages to using this method. A large portion of bone must be press-fitted and glued into the end-caps for proper adhesion. After testing, the gauge region of the bone core is cut out from the end-caps, which can damage the bone surface. In the platen compression test, a trabecular bone sample is compressed between two parallel smooth platens. This method is relatively easy to implement and is particularly suitable for small specimens (Bevill et al. 2006, MacNeil & Boyd 2008, Huang et al. 2010, Jiroušek et al. 2011) such as the samples used in this study. Thus the platen compression test was chosen for this work.

Fifteen bovine trabecular bone samples were destructively compressed using a material testing device (Instron 6022, 10 kN at Materials Testing Lab, UTS), a part of which is shown in Figure 3.5. The linear elastic and failure point, stiffness and apparent elastic modulus were determined. Prior to mechanical testing, specimens were thawed in a saline solution at room temperature and wrapped in saline-soaked gauze to prevent dehydration during experiment. The platen compression test, in which the bone samples were compressed between two parallel stainless-steel platens, was used for mechanical testing. The conventional platen setup for compressive tests produces an interruption of trabecular network at the specimen

ends and results in an initial nonlinear toe region in the stress-strain curve (Figure 3.6). Bending, sliding and settling of longitudinally-oriented trabeculae at the platen surface due to reduced stability caused by the loss of transverse trabeculae, is a commonly known structural end effect (Linde & Hvid 1989, Keaveny et al. 1997). The effect is enhanced when the platen surface is polished and lubricated as trabeculae slide more easily (Linde & Hvid 1989). The following protocol was used for the compression testing of the bone samples. Once the bone cylinder was carefully positioned in the centre of the lower platen, the actuator was adjusted by hand control to move the upper platen down to slightly touch the surface of sample. A compression preload of 5 N was first applied to guarantee the contact between the upper platen and bone sample. The strain at 5 N loading was defined as the zero strain. Then, a uniaxial compression preconditioning of 0 to 0.1% strain was used to minimize the end-artifact effect (Bevill et al. 2006), followed by a final ramp to failure (> 5% strain) at a strain rate of 0.5% per second. For three samples, before the final ramp, following the application of each strain step at intervals of 2% and 3%, the specimens were allowed to relax in order to establish an appropriate time interval for specimens to reach a plateau for stress relaxation. That interval was between 18 min and 22 min.

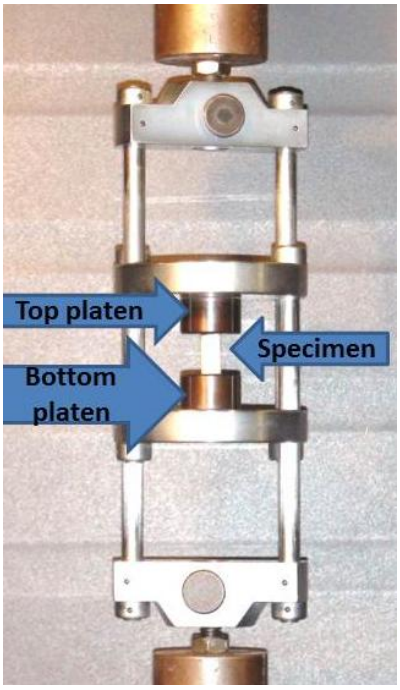


**Figure 3.5** Set-up for compression testing of the trabecular bone specimen in the mechanical testing device (Instron 6022, 10 kN).

The force and displacement data collected during the testing were analysed using a Microsoft Excel spreadsheet. Stresses and strains were calculated and the stress-strain curves were plotted for each sample (an example is shown in Figure 3.6). The apparent elastic modulus of trabecular bone was determined as the slope of the linear fit to the stress-strain curve between 40% and 65% of the maximum stress (Turner 1989).

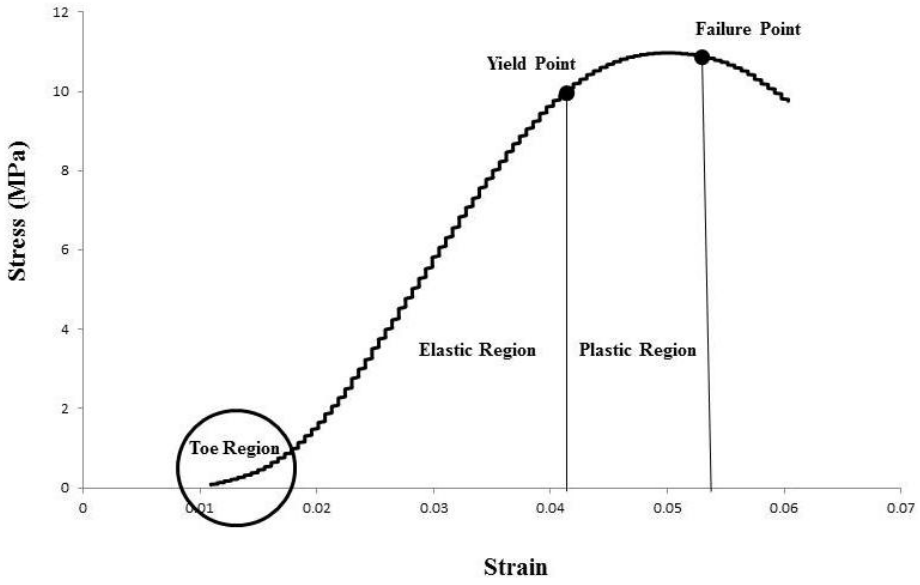


**Figure 3.6** A stress-strain curve obtained for a trabecular bone sample, illustrating the toe, elastic and plastic regions. The toe region located at the left of the curve is the end-artifact of the platen test.

## 3.5 Image Acquisition

### 3.5.1 Micro-CT images of the phantom

The phantom was inserted into the specimen housing of the mini-jig, between two compression platens. A polycarbonate base contained a load cell and a piston (Figure 3.1). The specimen holder located the sample in the centre of the device, thus ensuring consistent orientation of the specimen. The mini-jig with the mounted sample was placed horizontally on the bed of a µCT scanner (Inveon PET/CT, Siemens at National Imaging Facility, University of New South Wales) and fixed with adhesive tapes to prevent excessive movement of the jig during the displacement of micrometer head (Figure 3.7). The phantom was scanned at an

isotropic resolution of 50 µm with the following acquisition parameters: tube current 500 µA, acceleration voltage 40 kV, 360° rotation with 180 projections, and exposure time 2500 ms.

**Figure 3.7** Experimental setup showing the placement of the jig in the µCT scanner.

The first CT image of the phantom was acquired without loading (0% strain condition). The sample was then slowly uniaxially compressed. Three loading steps were applied, corresponding to a translation of the micrometer head of 0.03 mm, 0.06 mm and 0.1 mm. The load values were measured by the load cell for each displacement as well as during scans. The apparent elastic modulus of the phantom was determined from the stress-strain curve. Different elastic modulus was calculated from the three loading steps that were applied to the phantom. Finally, the images were exported from the µCT computer in the DICOM (Digital Imaging and Communications in Medicine) format.

### 3.5.2 Micro-MR images of the trabecular bone specimens

Due to the high cost of MR imaging, no μMR nor MR images of the phantom were obtained. First, two selected bone samples were thawed in a saline solution at room temperature. A common reference was provided by marking the samples with small dots of superglue at three separated points (two at the top and one at the bottom of the sample) that showed up on both MR and CT images. Each sample was then immersed in a saline solution tube to keep it fresh during image acquisition. The tube with the specimen was placed in the bore of a vertical 16.4 T magnet (Bruker Avance 16.4 T at National Imaging Facility, University of Queensland). The acquisition protocol employed a 3D fast low-angle shot pulse sequence (FLASH-3D) and the following parameters, a field-of-view (FOV) of 13 mm×26 mm × 13 mm, matrix 432 × 864 × 32 voxels, echo time (TE) = 3.096 ms, repetition time (TR) = 50 ms, flip angle = 22˚, scan time = 12 hrs 20 min, to obtain images with isotropic voxel size of 30 μm. Also, images with isotropic voxel sizes of 50 μm (matrix 256 × 512 × 256 voxels), 100 μm (128 × 256 × 128 voxels), and 200 μm (64 × 128 × 64 voxels) were obtained to evaluate the effect of resolution on the FE analysis. Finally, the images were exported from the μMRI computer in the DICOM format.

### 3.5.3 Whole-body MR images of the trabecular bone specimens

The specimen A and B were immersed in a saline solution container and placed in a whole-body MRI scanner operating at 3T (Siemens, Magneton Trio at National Imaging Facility, University of Queensland). Acquisition protocol used a FLASH-3D pulse sequence with parameters: FOV of $(50\ mm)^3$, matrix 192 × 192 × 192 voxels, TE = 6 ms, TR = 50 ms, flip angle = 30˚, scan time = 20 min, to obtain

images with an isotropic voxel size of 260 μm. A 32 channel head coil was used. Finally, the images were exported from the MRI computer in the DICOM format. With this FOV and matrix size no aliasing in image space was apparent.

### 3.5.4 Micro-CT images of the trabecular bone specimens

The bone specimens (A and B) of previous sections were wrapped in saline-soaked gauze, then inserted in the mini-jig ensuring they were kept wet during the scanning procedure. The experimental set-up was identical to that used for the phantom. The bone samples were scanned at an isotropic voxel size of 18 μm using the acquisition parameters: tube current 100 μA, acceleration voltage 80 kV, 360° rotation with 180 projections, exposure time 6500 ms. Then, μCT images with an isotropic voxel size of 36 μm were reconstructed from the 18 μm images using the reconstruction software provided with the scanner.

First, a compression pre-load of 5 N was applied to guarantee the contact between the piston and bone sample. The strain at 5 N loading was defined as the reference strain and bone specimens were scanned at this step. Then, each sample was slowly uniaxially compressed in the elastic region as determined by the preliminary mechanical testing of the fifteen bone samples (section 3.4.2).

Three loading steps were then applied, corresponding to a translation of the screw of the micrometer head of 0.2 mm, 0.4 mm and 0.6 mm. Following each loading step, the bone specimen was allowed to relax for 20 min prior to image acquisition, so that the specimen reached a plateau for stress relaxation, as determined by the

mechanical testing (section 3.4.2), and also suggested by Nazarian & Müller (2004), Thurner et al. (2006), Benoit et al. (2009).

Due to the step-wise loading and the stress relaxation occurring in the bone samples between two measurement sections, the stress–strain graphs consisted of three discontinuous sections between the applied displacement steps. Hence, a straight line was fitted from the end of one displacement step to a point on the next displacement step to provide a continuous graph from the step-wise data, as suggested by Nazarian & Müller (2004). Finally, the images were exported from the µCT computer in the DICOM format.

## 3.6 Transformation of Image Data into a Volumetric Mesh

### 3.6.1 Transformation of image data into a volumetric mesh

µCT, µMR and MR image data obtained in DICOM format were processed with a medical image processing software (MIMICS 14.1, Materialise). Materialise, Interactive Medical Image Control System (MIMICS) is a program designed to create 3D surface models from CT or MRI data. The following procedures were carried out to generate a finite element model from the image data.

#### 3.6.1.1 Importing DICOM image data

The slice images were imported consecutively into MIMICS (Figure 3.8). Representations of roughly the same cross section of the trabecular bone sample in

µCT, µMR and whole-body MR are shown in Figure 3.9. The image data information is presented in the Table 3.1.

**Table 3.1** Image data information

| | **Image voxel size (µm)** | | |
|---|---|---|---|
| **Sample** | **µCT** | **µMR** | **whole-body MR** |
| Phantom | 50 | ___ | ___ |
| Bone | 18 | 30 | 260 |
| | 36 | 50 | |
| | | 100 | |
| | | 200 | |

Due to limited CPU capacity, memory and storage space, the slice images were sorted by the acquisition time and each group of slices was consecutively imported and saved in separate files. For the same reasons, the 18 µm µCT image was not used and the 36 µm µCT image provided.

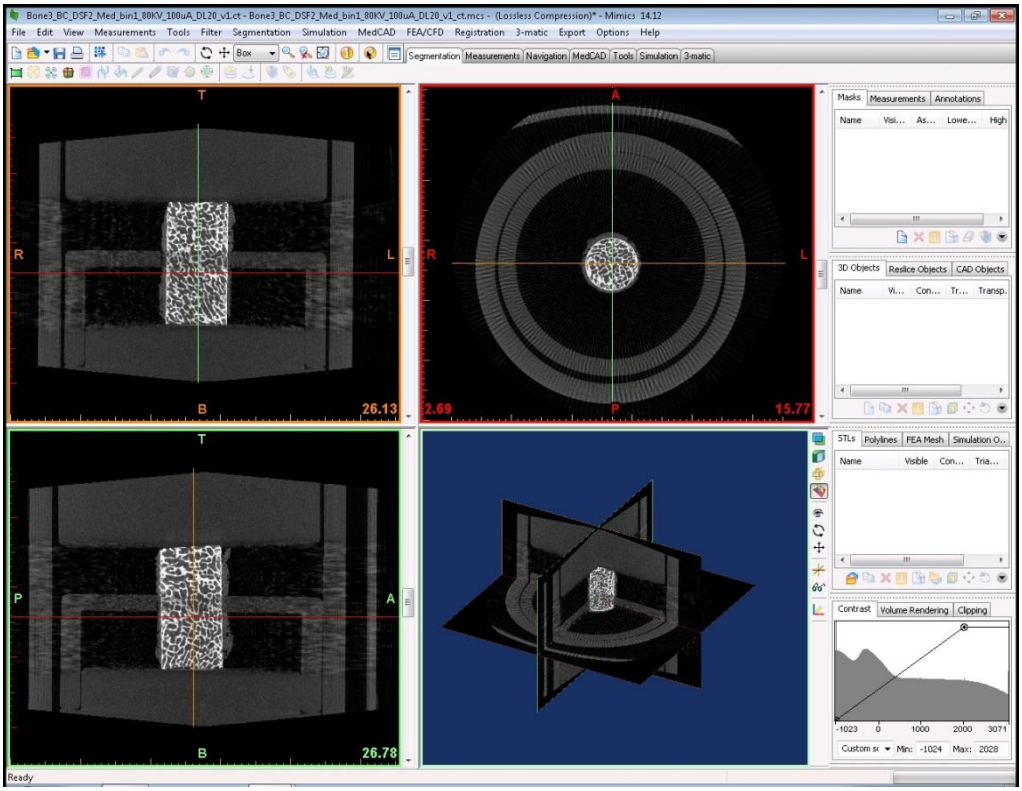


**Figure 3.8** The imported µCT image data of the trabecular bone specimen inside the mini-jig before compression

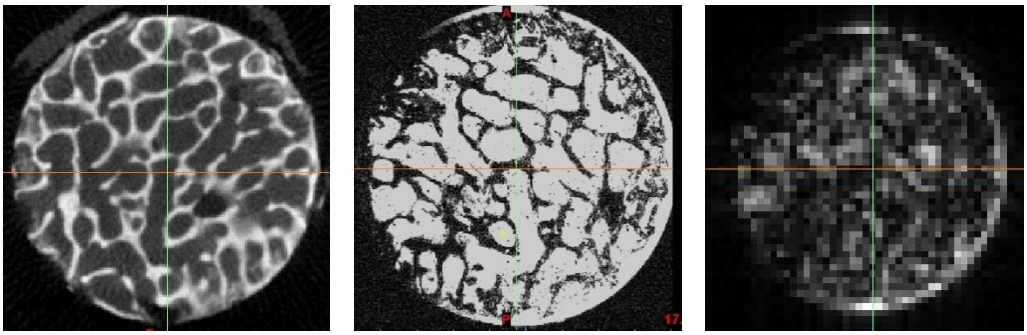

**Figure 3.9** Representations of roughly the same cross section of the trabecular bone sample in µCT (left), µMR (middle) and whole-body MR (right).

#### 3.6.1.2 Thresholding

Thresholding is the most widely used segmentation technique to separate bone voxels from non-bone voxels. Global thresholding was used to separate the phantom material from the surrounding air in the phantom images, and bone from marrow in the bone sample. All voxels with a grey value between lower and upper threshold values were assigned the bone lable. The threshold values used was obtained interactively by minor adjustment to the optimum values provided by MIMICS. In the μCT images, lower threshold value for the phantom material was set to -827 HU and that was 1000 HU for the bone samples, based on their grayscale histograms. The segmented image was used as a mask for further processing. In the μMR and MR images, the intensity range for bone was set to 370 – 6231 and 13 – 717, respectively.

#### 3.6.1.3 Region growing

After segmentation, the images often have small isolated groups of voxels. These regions must be eliminated, in order to avoid numerical problems in the following finite element analysis such as an unconstrained rigid body motion. A voxel could be taken as geometrically connected if it shares (1) one face, or (2) two edges, or (3) one edge and one node, or (4) at least three distinct nodes with other voxels. Such unconnected voxels were eliminated by a manually controlled region growing process.

### 3.6.1.4 Volumetric mesh generation

The segmented images were used to develop the hexahedron meshes. Eight-node hexahedron brick elements were automatically generated by the MIMICS mesher tool. The finite element mesh containing the definitions of all nodes and elements was exported as an input file to ANSYS for FE analysis. The element numbers of the FE meshes and required time to run FE analysis for different image voxel size are given in Table 3.2. Also the BVF of the bone samples were calculated in the MIMICS.

**Table 3.2** The element numbers of the FE meshes and required time to run FEA

| Sample | Voxel size (μm) | | Element numbers | Required time (min) |
|---|---|---|---|---|
| | μCT | MRI | | |
| Phantom | 50 | - | 8,928,112 | 15 |
| Bone | 36 | | 8,931,827 | 42 |
| | | 30 | 10,730,807 | 73 |
| | | 50 | 3,378,062 | 16 |
| | | 100 | 466,359 | 0.9 |
| | | 200 | 58,027 | 0.1 |
| | | 260 (whole-body) | 31,700 | 0.04 |

## 3.7 Finite Element Modelling of Phantom and Trabecular Bone

FE analysis was performed using a commercial software (ANSYS, V 13.0). The pre-processing, solution and post-processing stages of the FE model of the phantom and trabecular bone are described below. All FE analyses were implemented on the

Linux cluster running Red Hat Enterprise Linux 6.2 (64bit) all connected to a Server with a total of 59 TB of disk storage via a gigabit network. A typical cluster node consisted of 6 cores running at 1.3 GHz. ANSYS was executed in parallel node with a total memory allocation of 43 GB.

### 3.7.1 Element description and material selection

The FE models were imported into ANSYS. The eight-node hexahedron elements were used to model the phantom and trabecular bone structures. The element connectivity was checked and all coincident nodes were merged. The material properties were assigned, for the phantom, tissue elastic modulus 2870 MPa and Poisson's ratio of 0.3, and for bone samples tissue elastic modulus 983 MPa and Poisson's ratio of 0.3, as data from the back-calculation procedure by matching experimentally and computationally obtained apparent elastic moduli. The assigned material properties were considered to be linear, elastic, and isotropic.

Back-calculation is a technique used to compute an effective tissue modulus for trabecular bone by matching experimentally and computationally obtained apparent moduli (van Rietbergen et al. 1995). The procedure is as follows: (1) a trabecular bone specimen is mechanically tested within the linear elastic region to obtain the experimental apparent elastic modulus ($E_{\mathrm{exp}}^{\mathrm{app}}$); (2) the same specimen is scanned with micro-CT imaging to obtain architecture; (3) the three-dimensional image is converted into a finite element model; (4) assuming an initial guess of trabecular bone modulus ($E_{\mathrm{init}}^{\mathrm{tissue}}$), the predicted apparent modulus ($E_{\mathrm{FE}}^{\mathrm{app}}$) is calculated by simulating the same boundary conditions as the mechanical test; (5) the ratio of these

apparent moduli is multiplied by the initial guess of the tissue modulus to yield the effective tissue modulus($E_{\mathrm{eff}}^{\mathrm{tissue}}$). The back-calculation equation of trabecular bone tissue modulus is

$$E_{\mathrm{eff}}^{\mathrm{tissue}} = \frac{E_{\mathrm{exp}}^{\mathrm{app}}}{E_{\mathrm{FE}}^{\mathrm{app}}} \; E_{\mathrm{init}}^{\mathrm{tissue}} \tag{3.1}$$

### 3.7.2 Boundary conditions

To simulate the uniaxial compressive test (sections 3.5.1 and 3.5.2), the following boundary conditions were applied to the phantom and trabecular bone models: (1) the base of the model was constrained in the z-direction (zero displacement); (2) the displacements of 0.03 mm, 0.06 mm and 0.1 mm (phantom) and 0.2 mm, 0.4 mm, 0.6 mm (bone) in the z-direction were applied on the top of the model; (3) two nodes at the base of the model, displaced along the x-axis, the other along the x-axis and the y-axis, both nodes constrained to zero displacement to prevent any translations and rotations of the base.

### 3.7.3 Solution and output data

The static linear FE analysis was executed using an iterative preconditioned conjugate gradient (PCG) solver, and the total reaction force in the z-direction was calculated from the FE analysis. The overall apparent stress $\sigma$ was then calculated from the ratio of the reaction force ($F_{\mathrm{r}}$, N) to the cross-sectional area ($A$, mm²) of the specimen ($\sigma = F_{\mathrm{r}}/A$, N/mm²). The apparent stiffness ($S_{\mathrm{app}}$) was calculated from the ratio of reaction force to displacement ($S_{\mathrm{app}} = F_{\mathrm{r}}/d,$), the apparent elastic modulus ($E_{\mathrm{app}}$) in z-direction for the specimen as a whole was obtained from the ratio of

apparent stress to apparent strain in z-direction ($E_{\text{app}} = \sigma/\varepsilon$), or from the ratio of specimen's length (L) to its cross-sectional area, multiple by apparent stiffness ($E_{\text{app}} = S_{\text{app}} \frac{L}{A}$).

Three-dimensional displacement fields for the applied displacement of 0.4 mm were computed automatically from the FEA based on μCT images and used as a reference. μMR- derived displacement field were also obtained by FEA and compared to the reference field. Finally, estimated displacement fields using FE analysis based on various voxel sizes of μMR and whole-body MR images of the trabecular bone were compared with the results of μMR-based FE analysis to determine adequate voxel size for the prediction of the displacement field.

## 3.8 Comparison of Displacement Fields from FE Analysis

The difference between the FE-estimated displacement field based on μCT and that based on high resolution μMR was calculated for the trabecular bone specimen. The estimated displacement fields arising from μMR images of various voxel sizes, and whole-body MR were compared to that of high resolution μMR, in order to evaluate the effect of image voxel size on the accuracy of the FE result, and the capability of whole-body MR-based FE analysis to predict the displacement field.

Images acquired at different times, from different modalities such as μCT and μMR scanners, are usually defined in different coordinate systems. Thus, to compare μCT and μMR images, the following steps were done.

(1) Registration: it is necessary to put the images into the same coordinate system. Using a program written by Fulton (2000) in Interactive Data Language (IDL), a global rigid-body transformation matrix was determined from pairs of markers coordinates. The algorithm followed the method of Horn (1987) which provides a closed-form least-squares solution (see Appendix B in Fulton 2000 for program listing). The rigid-body transformation comprises rotations and translations. The transformation is represented in homogeneous coordinates by matrix

$$\mathrm{T_c} = \begin{bmatrix} \mathrm{R} & & & \mathbf{t} \\ 0 & 0 & 0 & 1 \end{bmatrix}, \tag{3.2}$$

where $\mathbf{t} = [\Delta x, \Delta y, \Delta z]^{\mathrm{T}}$ represents the translation vector, and R is a rotation transformation matrix about x, y, z axes. In Euler angles,

$$\mathrm{R} = \mathrm{R}_z(\psi)\mathrm{R}_y(\theta)\mathrm{R}_x(\phi) \tag{3.3}$$

$$= \begin{bmatrix} \cos\theta\cos\psi & -\cos\phi\sin\psi + \sin\phi\sin\theta\cos\psi & \sin\phi\sin\psi + \cos\phi\sin\theta\cos\psi \\ \cos\theta\sin\psi & \cos\phi\cos\psi + \sin\phi\sin\theta\sin\psi & -\sin\phi\cos\psi + \cos\phi\sin\theta\sin\psi \\ -\sin\theta & \sin\phi\cos\theta & \cos\phi\cos\theta \end{bmatrix}$$

The registration method assumes a rigid body transformation between the two coordinate frames. The validity of the assumption can be checked by calculating the differences $\epsilon_i$ between measured μMR marker coordinates $m_i$ and the transformed μCT coordinates $c_i' = T_c c_i$, where $\mathrm{T_C}$ transforms the μCT image data to the μMR coordinate

$$\|\epsilon_i\| = \|c_i' - m_i\|. \tag{3.4}$$

The calculation of the transformation matrix needs at least three paired points from the two images. The samples were marked with small dots of superglue at three separated points (section 3.5.2) but some of these did not show up in μCT images. Using the MIMICS software, identical geometric structures from μCT and μMR

images were identified, segmented in 3D (as shown in Figure 3.10), and their centroids were used as a substitute for the missing markers. With increasing voxel size, the identification of corresponding structures became impossible.

Then, an IDL procedure was coded to apply the rigid-body transformation to μCT image (Appendix B.1). The IDL was run under Linux operating system on a PC platform with 7 Intel Xeon E5420 cores operating at 2.5 GHz, with 32 GB RAM and 0.5 TB RAID 1 storage.

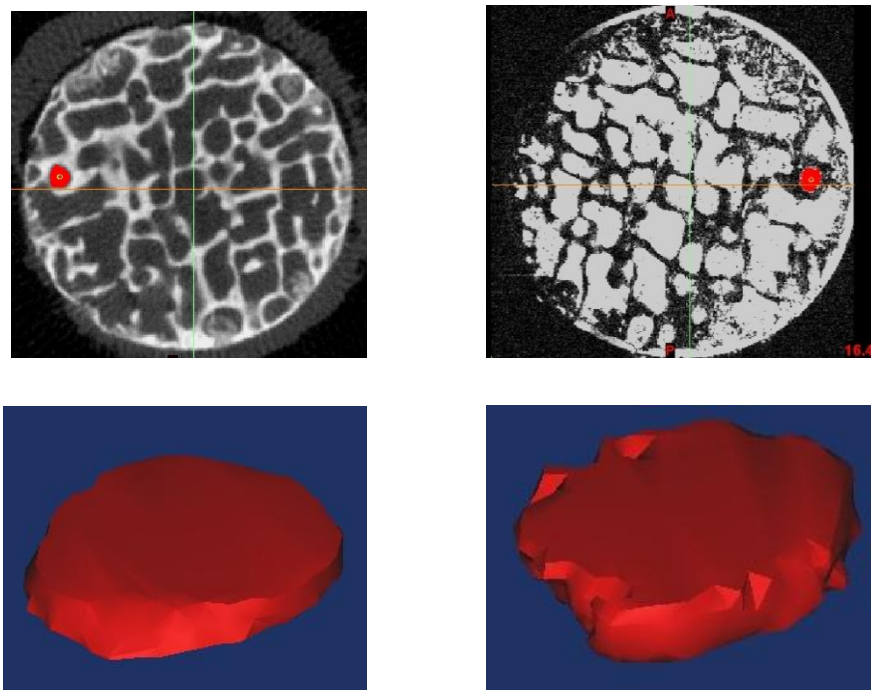

**Figure 3.10** An illustrated example of the determination of corresponding geometric structures from μCT (top left) and μMR (top right) images, and the 3D segmented structures (bottom).

(2) Interpolation and comparison: even though the sample is the same, the nodes in the two data sets (transformed μCT and μMRI) are not guaranteed to occupy the same positions, and we need to find displacements at the locations of one set of nodes by interpolation. Thus, an IDL procedure was coded (Appendix B.2) based on

Braun (2012). The interpolated value of a displacement field $\boldsymbol{d}(\boldsymbol{r}_i)$ at a point $\boldsymbol{r}_i = (x, y, z)$ is obtained by a weighted average:

$$\boldsymbol{d}(\boldsymbol{r}) = \frac{\sum_{i=1}^{N} p_i \boldsymbol{d}(\boldsymbol{r}_i)}{\sum_{i=1}^{N} p_i}, \tag{3.5}$$

and weight $p_i$ is

$$p_i = \xi - \|\boldsymbol{r} - \boldsymbol{r}_i\| = \xi - \sqrt{(x - x_i)^2 + (y - y_i)^2 + (z - z_i)^2}, \tag{3.6}$$

where ξ is the largest possible distance between a node and its neighbour nodes ($\xi = \sqrt{3}\eta$), and η is the inter-nodal separation along any coordinate axis, which initially equals to the image voxel size and *i* ranges over all nodes in the neighbourhood.

The difference (error) between estimated displacements fields using FE analyses based on μCT, high resolution μMR, μMR images of various voxel sizes, and whole-body MR images of the trabecular bone specimen was calculated. The mean error and the standard deviation of the displacement field were calculated to validate the accuracy of the result of μMR-based FE analysis.

# Chapter 4: Results and Discussion

This chapter presents the results and discussions of findings. First, the measurements of the bone apparent elastic modulus obtained from mechanical tests will be presented, followed by the finite element model validation results. Then, the results of finite element analysis based on whole-body MR and MR images with different element voxel sizes will be presented in the form of mechanical properties such as apparent stiffness, apparent elastic modulus, and displacement field. Finally, limitations and conclusions of the research are provided, and a possible direction for future research is pointed out.

## 4.1 Mechanical Testing of Trabecular Bone and Physical Phantom

Mechanical testing was carried out on fifteen trabecular bone specimens in order to determine the elastic region of the stress-strain response. This was used to guide the setup of strain steps in-camera (in-situ for μCT imaging) in the compression test on two trabecular bone samples (denoted A and B). The apparent elastic moduli, ultimate stress and ultimate strain obtained from the experiments are given in Table 4.1. The time it took the specimens to reach a plateau for stress relaxation was found to be between 18 min and 22 min. The values for the apparent elastic modulus obtained from the in-camera mechanical test on the physical phantom are given in Table 4.2.

**Table 4.1** Apparent elastic modulus, ultimate stress and ultimate strain for bovine trabecular bone samples.

| Bone sample | Elastic modulus | Ultimate stress | Ultimate |
|---|---|---|---|
| 1 | 390 | 11.2 | 0.051 |
| 2 | 316 | 12.4 | 0.063 |
| 3 | 316 | 13.8 | 0.059 |
| 4 | 455 | 12.3 | 0.062 |
| 5 | 414 | 11.0 | 0.050 |
| 6 | 330 | 8.4 | 0.052 |
| 7 | 311 | 6.9 | 0.057 |
| 8 | 195 | 4.3 | 0.490 |
| 9 | 371 | 7.6 | 0.057 |
| 10 | 191 | 6.7 | 0.062 |
| 11 | 166 | 4.3 | 0.054 |
| 12 | 176 | 3.2 | 0.041 |
| 13 | 173 | 3.1 | 0.039 |
| 14 | 176 | 5.4 | 0.053 |
| 15 | 166 | 4.0 | 0.050 |
| Mean | 280 | 7.6 | 0.083 |
| SD | 100 | 3.7 | 0.11 |

**Key:** SD = standard deviation

The results of the mechanical tests show a wide variation in the mechanical properties of the trabecular bone specimens. This is likely attributable to their heterogeneity including variation in trabecular bone volume fraction, architecture,

and tissue properties. Choi et al. (1992) found that compressive elastic modulus within a single proximal tibia varied as much as 100-fold from one location to another. Therefore a set of regions of interest (ROI) needs to be defined accurately for imaging and FE analysis. Conventional BMD regions of interest for the femur, that is, the femoral neck, trochanter, or Ward's triangle, enclose bone volumes that can be scanned and modelled. For example, the default region for the femoral neck in a DXA scan is the narrowest and lowest density section of the neck; typically, this will be about half way between the femoral head and the trochanter (El Maghraoui & Roux 2008).

**Table 4.2** Apparent elastic modulus of phantom in-camera

| | $E_{app}$ (MPa) |
|---|---|
| E1 | 110 |
| E2 | 114 |
| E3 | 124 |
| Mean ± SD | 116 ± 7 |

**Key:** $E_{app}$ = apparent elastic modulus, SD = standard deviation

## 4.2 Validating FE Analysis

### 4.2.1 Evaluating high resolution µCT-based FE analysis

The accuracy of FE analysis based on high resolution µCT image has been tested against mechanical test as a gold standard method. The calculated apparent elastic modulus, tissue effective elastic modulus values from the FE analysis (section 3.7.1)

of the trabecular bone samples, and its range are given in Table 4.3. Each value of apparent elastic modulus is an average over the three loading steps.

**Table 4.3** Apparent elastic modulus and tissue effective elastic modulus of bone samples (high resolution µCT-based FEA)

| Bone sample | $E_{app}$(MPa) ± SD | $E_{tissue}$ (MPa) | Range in $E_{tissue}$ (MPa) |
|---|---|---|---|
| A | 172 ± 43 | 964 | 722 - 1207 |
| B | 180 ± 41 | 1003 | 777 - 1228 |

**Key:** $E_{app}$ = apparent elastic modulus, $E_{tissue}$ = tissue effective elastic modulus

FE analysis based on high resolution µCT images of the physical phantom yielded the apparent elastic modulus of 116 MPa, which is well within the range of the results of compression tests performed on the phantom (116 ± 7 MPa). The large difference (95.9%) between the apparent elastic modulus of the phantom (116 MPa) and its tissue elastic modulus (2870 MPa) is due to the phantom structure.

For the trabecular bone samples the predicted tissue effective modulus from FE analysis are in the range of reported values from previous study. These results indicate that the linear FE model estimation of tissue effective elastic modulus is in agreement with those experimentally determined (Ryan & Williams 1989). Van Rietbergen et al. (1995) reported an adequate accuracy of FE based on µCT scans with image voxel size of 40 µm.

### 4.2.2 Validating high resolution µMR-based FE analysis

The accuracy of FE analysis based on high resolution µMR image (30 µm) has been compared to that based on high resolution µCT image (36 µm). The predicted tissue

elastic modulus, apparent elastic modulus and its range values from the high resolution µMRI-based FE analysis for bone samples are given in Table 4.4.

**Table 4.4** Apparent elastic modulus and tissue effective elastic modulus of bone samples (high resolution µMR-based FEA)

| **Bone sample** | **$E_{tissue}$ (MPa)** | **$E_{app}$(MPa)** |
|---|---|---|
| A | 988 | 168 |
| B | 1000 | 181 |

**Key:** $E_{app}$ = apparent elastic modulus, $E_{tissue}$ = tissue effective elastic modulus

The calculated tissue elastic modulus from the high resolution µMRI-based FE analysis for bone sample A is 988 MPa, and for bone sample B is 1000 MPa, that are within the range of the results from the µCT-based FE analysis which are (722 – 1207) MPa for bone sample A, and (777 – 1228) MPa for bone sample B. The differences between calculated tissue elastic modulus from the µCT- and µMR-based FEA for bone samples A and B are 2.5% and 0.3% respectively, and indicating that our FE models are able to predict the tissue elastic modulus of trabecular bone.

## 4.3 Linear and Geometric Non-linear FE Analysis

Table 4.5 presents the reaction forces values from the FE models based on µMR image (50 µm) of trabecular bone sample for three load levels.

**Table 4.5** Reaction forces of linear and geometric non-linear FEA based on MR with image voxel size 50 µm

| Strain (%) | Reaction force (N) | |
|---|---|---|
| | **Linear FEA** | **Non-linear FEA** |
| 1.15 | -164 | -165 |
| 2.30 | -303 | -304 |
| 3.45 | -460 | -462 |

FE analysis of load levels in the elastic range indicates the more computationally costly deemed for geometric non-linear analysis do not affect the results significantly. Therefore, a linear elastic FE analysis is sufficiently accurate at low load levels, a conclusion also supported by others (Keaveny et al. 1994, Morgan & Keaveny 2001, Bayraktar et al. 2004a). Moreover, a non-linear FE analysis of a high resolution model would not be tractable given the computational resources available.

## 4.4 The Effect of Voxel Size on the apparent tissue elastic modulus

The effect of voxel size on FEA results has been evaluated. The results of FEA based on µMR images with different voxel sizes and whole-body MR image of trabecular bone samples and BVF are presented in Table 4.6. BVF calculated by dividing of volume occupied by bone to total volume of the sample.

**Table 4.6** Apparent elastic modulus, tissue elastic modulus and stiffness from µMRI- and whole-body MRI-based FEA for bone samples A and B, and BVF

| Voxel size (µm) | $S_{app}$ (N/mm) | | $E_{app}$ (MPa) | | $E_{tissue}$ (MPa) | | BVF | |
|---|---|---|---|---|---|---|---|---|
| | A | B | A | B | A | B | A | B |
| 30 | 799 | 653 | 168 | 181 | 988 | 1000 | 0.43 | 0.45 |
| 50 | 820 | 662 | 172 | 186 | 963 | 997 | 0.46 | 0.48 |
| 100 | 1027 | 796 | 215 | 223 | 769 | 830 | 0.54 | 0.56 |
| 200 | 900 | 781 | 189 | 219 | 877 | 846 | 0.52 | 0.54 |
| 260 (whole-body) | 994 | 812 | 209 | 225 | 794 | 804 | 0.65 | 0.71 |

**Key:** $S_{app}$ = apparent stiffness, $E_{app}$ = apparent elastic modulus, BVF = bone volume fraction, $E_{tissue}$ = tissue effective elastic modulus

The mechanical properties obtained from FE analysis based on whole-body MR and µMR images with various voxel sizes were compared to those derived from high resolution µMR image with voxel size of 30 µm. Table 4.6 shows that at the largest voxel size (200 µm) in µMR, the apparent elastic modulus was overestimated by 13% for bone sample A, and 21% for bone sample B compared to the 30 µm voxel case. For whole-body MRI (260 µm voxel) the overestimate rose to 24% for both bone samples. However, the apparent tissue elastic modulus is within the range obtained from high resolution µCT: (722 – 1207) MPa and (777 – 1228) MPa for bone samples A and B, respectively (Table 4.3).

Also, the results are in agreement with previous studies investigating the effect of µCT element size on the trabecular bone mechanical properties (Keyak & Skinner 1992, van Rietbergen et al. 1995). Van Rietbergen et al. (1995) reported 19% maximum difference in the calculated apparent elastic modulus between two models with 20 µm and 100 µm voxels size. The overestimate in the result from low

resolution MR when compared to higher resolution MR images was expected due to possibly resulting from artefactual connections being introduced into the trabecular network once voxel dimensions exceed the trabecular thickness and spacing. Newitt et al. (2002) reported that in the limited resolution of *in vivo* MR images, the measurements of the apparent trabecular bone volume fraction, trabecular thickness and trabecular number were overestimated, while the trabecular spacing was underestimated.

If the whole-body MR based FE method is going to be utilised as a clinical tool for the assessment of bone quality, further *in vivo* and *in vitro* experiments are needed to validate the results of the calculations described in this thesis. Therefore, methods need to be developed to create patient-specific models that take account of both morphological and material differences between subjects.

The relationships of predicted average apparent elastic modulus with voxel element size and average BVF for bone samples are plotted in Figure 4.1.

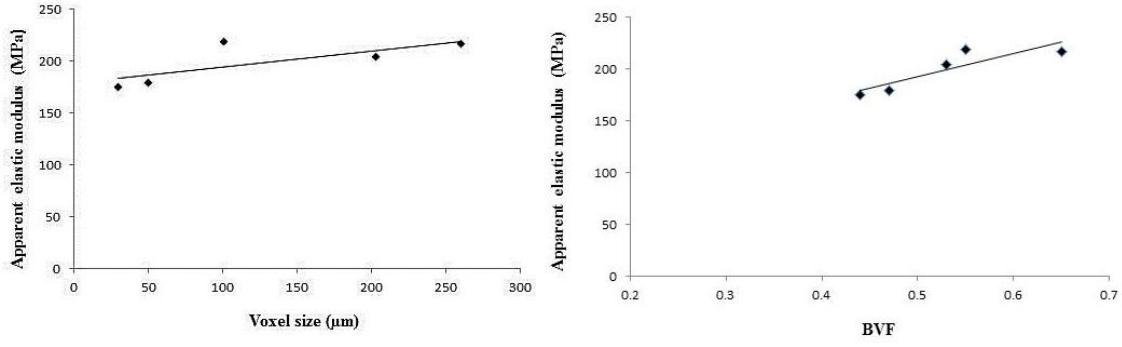


**Figure 4.1** Relationship of the estimated apparent elastic modulus from µMRI-based FEA with image voxel size (left), and BVF (right) for bone sample.

The variation in the apparent elastic modulus appears to correlate with differences in the bone volume fraction, which varied between 0.44 and 0.68. Figure 4.2 shows the variation of BVF with voxel size.

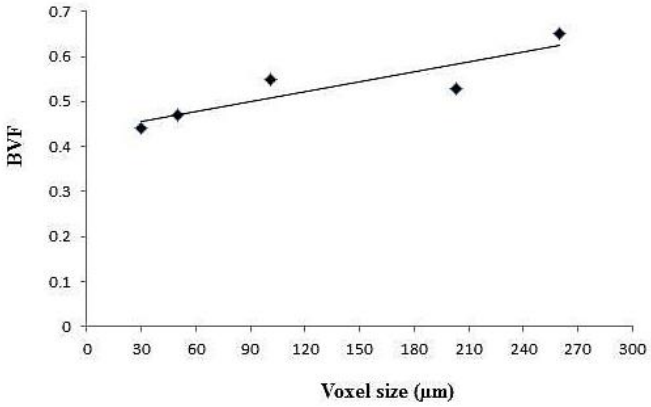


**Figure 4.2** The relation between the bone volume fraction and MR image voxel size.

BVF appears to increase linearly with voxel size. As voxel size increased from 30 µm to 260 µm, BVF increased by 54%. The values of BVF and the apparent elastic modulus from whole-body MR are substantially higher than those obtained from high resolution µMR, likely due to limited spatial resolution of the images. Optimising the image acquisition protocol and image processing (Hwang & Wehrli 2002, Jiroušek et al. 2011, Juras et al. 2012) may help reduce the impact of PVE on the measured parameters and make the whole-body MR measures closer to the absolute measures of trabecular bone properties.

## 4.5 Displacement Field Visualization

The displacement vectors were easily visualized with the ANSYS FE post-processing tool. A distribution of displacement magnitude was provided from the FE analysis post-processing results. An example is shown in Figure 4.3.

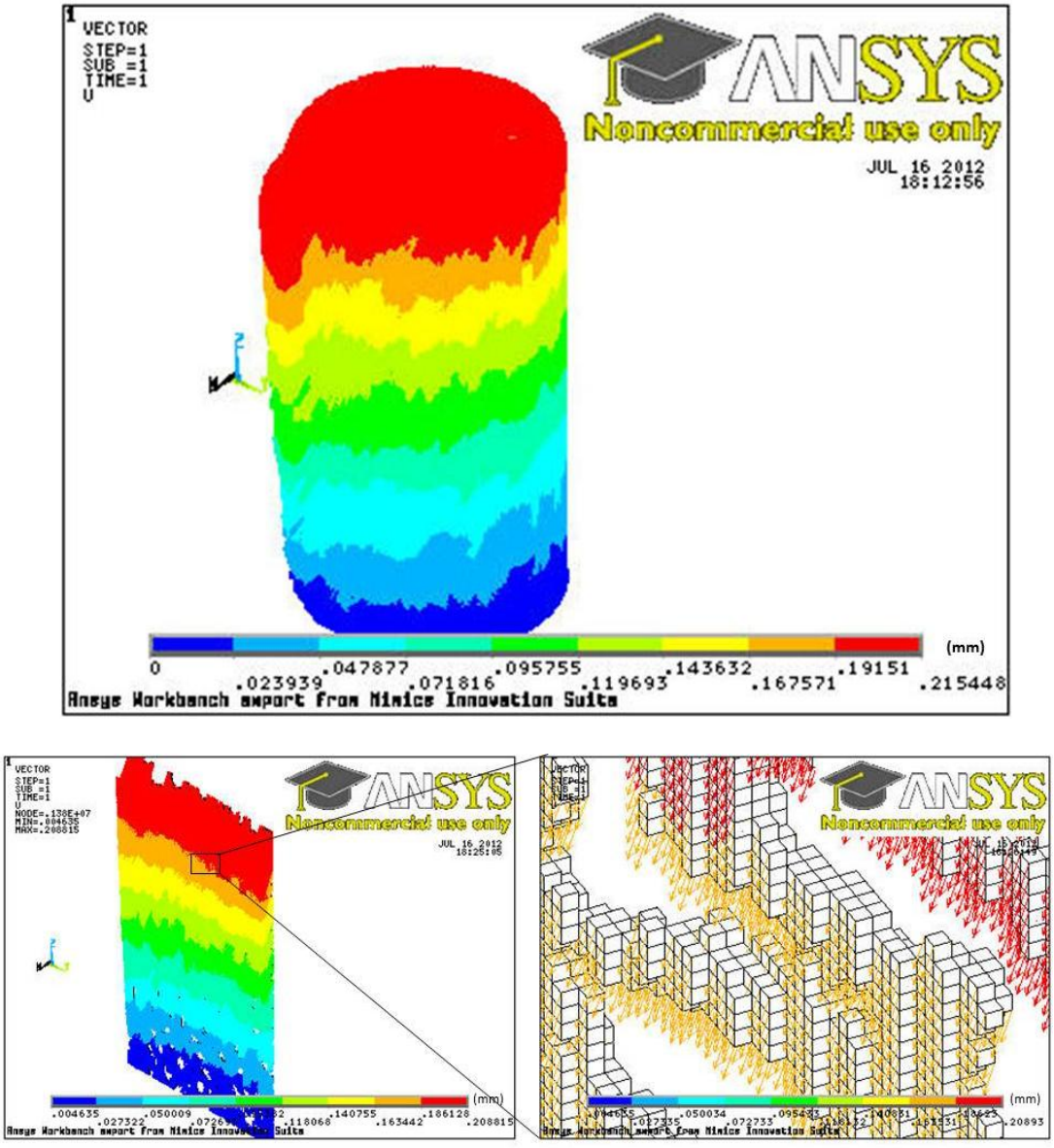


**Figure 4.3** The displacement magnitude from FE analysis based on μMR image data for the applied displacement of 0.2 mm at the top of specimen, the bottom left is a central longitudinal section of the top model. Because of the density of the displacement field, the individual vector cannot be seen, a zoomed version of the portion of the sample is provided on the right of figure.

As the displacement magnitude is predominately due to z component, then the colour scheme effectively codes for the z component. The colour banding of the structure indicates that displacement magnitude monotonically decreased toward the base platen. Figure 4.4 shows a displacement magnitude from FE analysis based on μMR, and whole-body MR images.

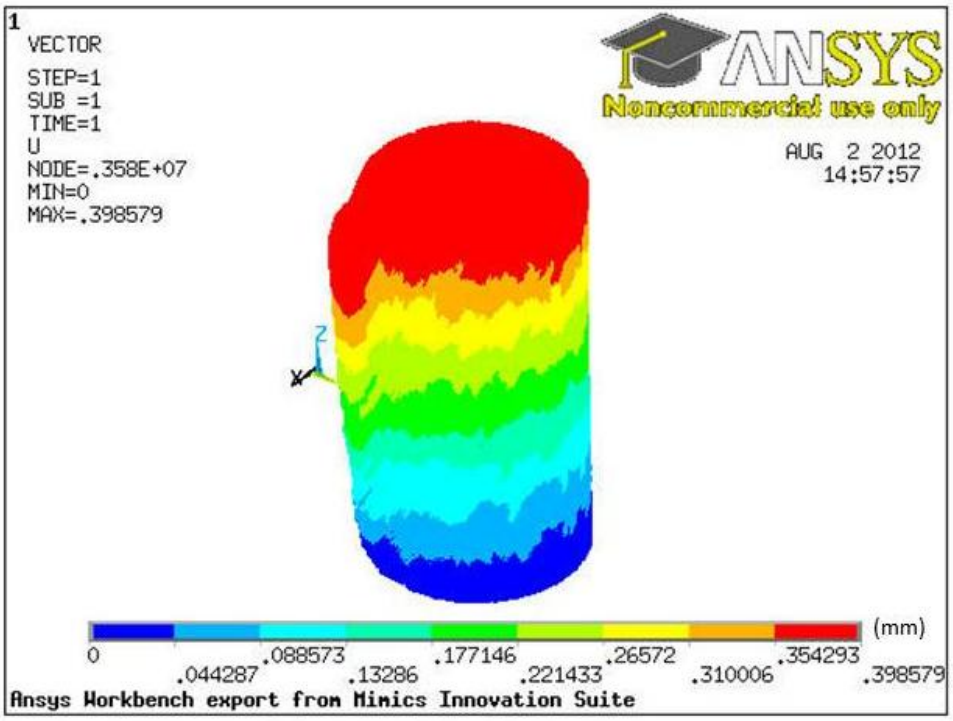


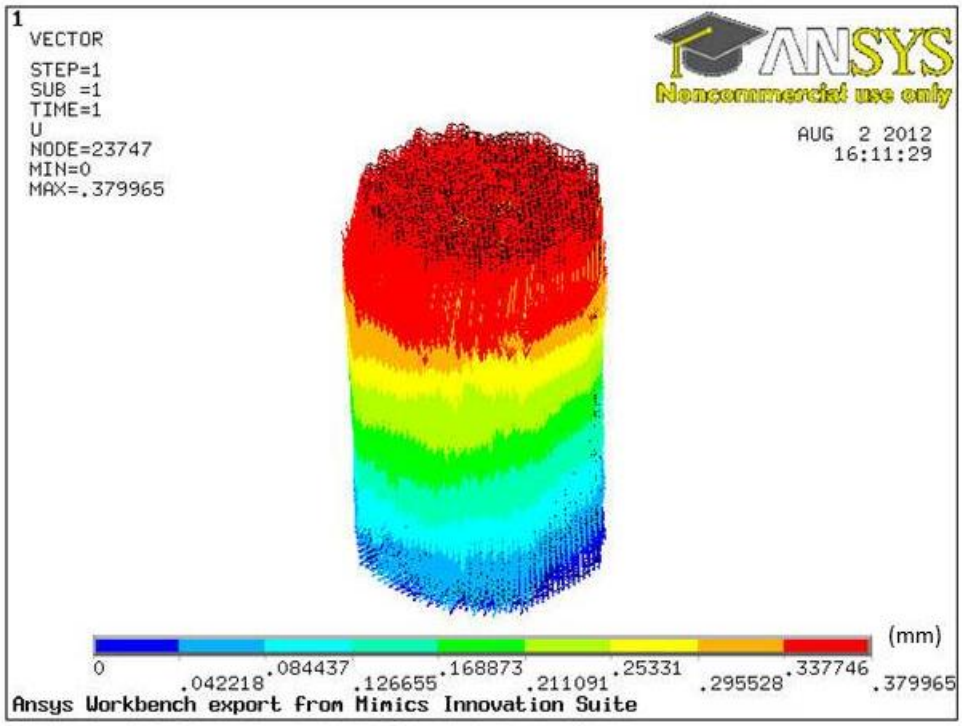


**Figure 4.4** The displacement magnitude from FE analysis based on μMR image data (top), and whole-body MR image (bottom) for the applied displacement of 0.4 mm at the top of specimen.

The thicknesses of colour bands represent the average of displacement magnitudes. The smoother appearance of the μMR image data is due to the data density been greater by a factor of 650.

## 4.6 Displacement Fields Comparison

### 4.6.1 Comparison of μCT and high resolution μMRI (30 μm)

In order to compare the displacement fields of μCT and μMR, their coordinate frames needed to be registered. Transformation matrix was derived from coordinates of three paired marker points in the μCT and μMR using the procedures described in section 3.8. The two first markers are anatomical markers, and the third one is physical (glue) marker. The initial marker coordinates are presented in Table 4.7.

**Table 4.7** Paired coordinate measurements

| Marker | μCT (mm) | | | μMR (mm) | | |
|---|---|---|---|---|---|---|
| | X | Y | Z | X | Y | Z |
| 1 | -0.509 | 3.547 | 7.012 | -6.511 | 3.812 | 7.298 |
| 2 | -4.356 | 1.628 | 5.773 | -3.708 | 0.809 | 5.985 |
| 3 | -0.698 | -0.130 | -9.911 | -7.896 | 0.776 | -9.667 |

Using marker data the transformation matrix coefficients were to be:

$$T_C = \begin{bmatrix} -0.4104 & -0.8703 & 0.2724 & -5.5966 \\ 0.9038 & -0.3485 & 0.2484 & 3.8234 \\ -0.1212 & 0.3482 & 0.9296 & -0.4955 \\ 0.0000 & 0.0000 & 0.0000 & 1.0000 \end{bmatrix}$$

The differences $\epsilon_i$ between measured μMR marker coordinates $m_i$ and the transformed μCT coordinates $c_i'$ are given in Table 4.8.

**Table 4.8** Errors in transformed coordinates of µCT image

| Marker | Error (mm) | | | |
|---|---|---|---|---|
| | $\epsilon_x$ | $\epsilon_y$ | $\epsilon_z$ | $\|\epsilon\|$ |
| 1 | 0.053 | 0.056 | 0.021 | 0.080 |
| 2 | 0.054 | 0.057 | 0.019 | 0.081 |
| 3 | 0.001 | 0.001 | 0.002 | 0.002 |
| Mean | 0.036 | 0.038 | 0.014 | 0.054 |
| SD | 0.031 | 0.032 | 0.011 | 0.045 |

**Key:** $\epsilon_x$, $\epsilon_y$, $\epsilon_z$= Cartesian components of error, $\|\epsilon\|$= norm errors

The components of the average errors in the x and y directions are of similar magnitude, about the µCT image voxel size whereas the mean error in the z direction is about the half the image voxel size, indicating the rigid body transformation relates the two frames well.

Two programs coded in IDL (Appendices B.1 and B.2) were used. Transform.pro applied the transformation matrix $T_C$ to the µCT image data thus aligning µCT and µMR images. Program displ_discr_fast.pro compared, node by node, the displacement in µMR against the transformed displacement in µCT. The code included interpolation of displacements in a neighbourhood of each node location. Finally, the discrepancy between displacements in the two files at each node positions was calculated. Table 4.9 shows the components of mean displacement errors in the x, y and z directions, mean norm error, the standard deviations of mean errors and mean norm error between µCT with high resolution µMR images.

**Table 4.9** The components of displacement errors between FE results of µCT (36 µm) with high resolution µMR (30µm) for the applied displacement of 0.4 mm.

| Mean Errors (mm) ± SD | | | |
|---|---|---|---|
| $\epsilon_x$ | $\epsilon_y$ | $\epsilon_z$ | $\|\epsilon\|$ |
| 0.101 ± 0.008 | 0.022 ± 0.010 | 0.099 ± 0.002 | 0.127 ± 0.013 |

**Key:** $\epsilon_x$, $\epsilon_y$, $\epsilon_z$ = Cartesian components of error, $\|\epsilon\|$= mean norm errors

### 4.6.2 Comparison of MR images of different voxel sizes

The transformation matrix $T_c$ based on the coordinates of three paired points in the µMR and whole-body MR coordinate frames was determined to be

$$T_C = \begin{bmatrix} 0.9564 & -0.2900 & -0.0358 & 1.1218 \\ 0.2901 & 0.9570 & -0.0006 & 91.4997 \\ 0.0344 & -0.0098 & 0.9994 & 4.2496 \\ 0.0000 & 0.0000 & 0.0000 & 1.0000 \end{bmatrix}$$

**Table 4.10** Errors in transformed coordinates of µMRI (30 µm)

| Marker | Error (mm) | | | |
|---|---|---|---|---|
| | $\epsilon_x$ | $\epsilon_y$ | $\epsilon_z$ | $\|\epsilon\|$ |
| 1 | 0.018 | 0.028 | 0.024 | 0.041 |
| 2 | 0.026 | 0.030 | 0.035 | 0.053 |
| 3 | 0.034 | 0.032 | 0.029 | 0.054 |
| Mean | 0.026 | 0.030 | 0.029 | 0.049 |
| SD | 0.008 | 0.002 | 0.005 | 0.007 |

**Key:** $\epsilon_x$, $\epsilon_y$, $\epsilon_z$= Cartesian components of error, $\|\epsilon\|$= norm errors

The Cartesian components of the average error are of similar magnitude and about the voxel size of the high resolution μMR image, indicating the rigid body transformation relates the two frames well.

The IDL programs were executed and discrepancy between displacements in two MR files was calculated. The reference displacement field was that of the 30 μm μMR data. The computed components of mean displacement errors in the x, y and z directions, norm error, the standard deviations of mean errors and norm error for each lower resolution MR data relative to the reference are given in Table 4.11.

**Table 4.11** The components of displacement errors between FE results of lower resolution μMR, whole-body MR and high resolution μMR (30 μm) for the applied displacement of 0.4 mm.

| **Voxel size** | **Mean errors (mm) ± SD** | | | |
|---|---|---|---|---|
| **(μm)** | $\epsilon_x$ | $\epsilon_y$ | $\epsilon_z$ | $\|\epsilon\|$ |
| 50 | - 0.006 ± 0.02 | - 0.011 ± 0.01 | - 0.092 ± 0.01 | 0.098 ± 0.01 |
| 100 | - 0.013 ± 0.02 | - 0.003 ± 0.01 | - 0.113 ± 0.01 | 0.115 ± 0.01 |
| 200 | - 0.120 ± 0.03 | 0.071 ± 0.01 | - 0.116 ± 0.01 | 0.176 ± 0.03 |
| 260 (whole-body ) | - 0.114 ± 0.02 | - 0.086 ± 0.01 | - 0.120 ± 0.02 | 0.188 ± 0.04 |

**Key:** $\epsilon_x$, $\epsilon_y$, $\epsilon_z$= Cartesian components of error, $\|\epsilon\|$= norm errors

The results show that increasing the voxel size leads to a systematic overestimation of displacement measurements compared to the reference values. Figure 4.5 shows a plot of the mean displacement magnitude error as a function of the voxel size.

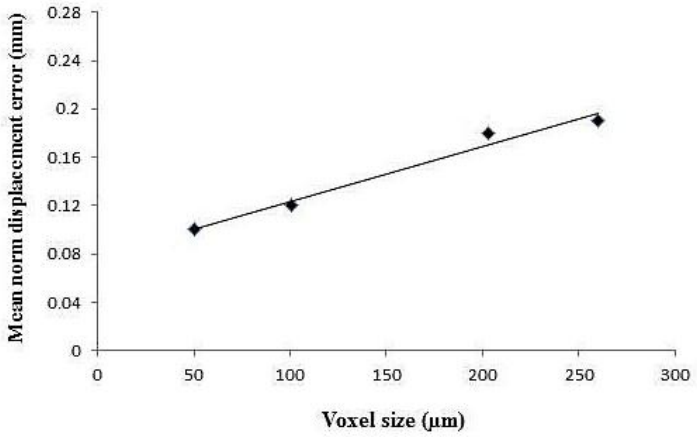


**Figure 4.5** The relationship between the mean norm displacement error and MR image voxel size

The errors in predicted displacement fields for the 50 µm and 100 µm models are 3-4 voxels (of high resolution µMR). For the whole-body MR, the error is 5-6 voxels of the reference µMR. The discrepancy may be due to partial volume effects and loss of trabecular connection and variation in the bone volume fraction across resolutions, the latter effect is shown in Figure 4.2, which shows BVF increase linearly with image voxel size. With voxel size increasing from 50 µm to 260 µm, the BVF increased by 49%, and mean displacement error increased to 92%. If BVF contribute to the results, increasing BVF with voxel size could count for increasing a half of error. As well, interpolation of MRI for the purpose of the registration may have contributed to the error.

The partial volume effect will increase whenever an object of interest is smaller in any one orthogonal direction than the voxel. The effect of PVE can be reduced by sub-voxel processing which sub-divides voxels and assigns voxel intensities to each sub-voxel, based on the amount and location of the bone of surrounding voxels and strict bone mass conservation (Hwang & Wehrli 2002, Braun 2005).

Moreover, Les et al. (1997) demonstrated that while there is a correlation ($0.69 < r < 0.90$) between the surface strain of voxel mesh FE models and the measured surface strains in strain gauge experiments, FE models tended to overestimate the strain magnitudes, due to jagged inner and outer surfaces of the model. Various methods have been proposed to generate smooth surfaces from hexahedron elements (Muller & Ruegsegger 1995, Viceconti et al. 1999), but they may place excessive demands on computational resources.

Since the average displacement is expected to vary with the depth of the model in the direction of applied force, we investigated the dependency of displacement error on z. With Pearson correlation coefficient, we found that there is no correlation ($-0.09 < r < 0.0$) between the z component of errors and depth of the model.

The mean displacement error was also plotted against apparent elastic modulus (Figure 4.6).

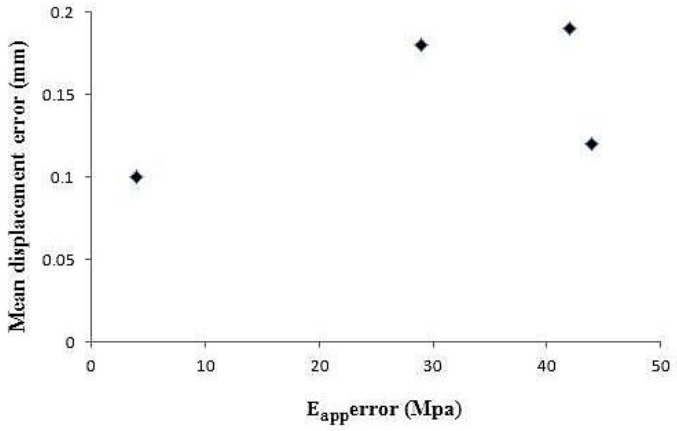


**Figure 4.6** Variation of the mean displacement norm error with the apparent elastic modulus error.

Although the small number of data points does not permit firm conclusion to be reached, the two measures appear to be statistically independent. The apparent lack of statistical correlation suggests that the displacement field estimate incorporate information about mechanical function additional to that provided by the apparent elastic modulus.

The results of displacement field estimated based on high resolution μMR and whole-body MR images are presented in Table 4.12.

**Table 4.12** The components of displacement between FE results of whole-body MR and high resolution μMR (30 μm)

| **Voxel size (μm)** | **Displacement ± SD (mm)** | | | **Mean norm displacement** |
|---|---|---|---|---|
| | **dx** | **dy** | **dz** | **± SD (mm)** |
| 30 | 0.059 ± 0.02 | -0.041 ± 0.02 | -0.158 ± 0.19 | 0.6421 ± 0.13 |
| 260 (whole-body) | -0.106 ± 0.02 | 0.009 ± 0.02 | -0.162 ± 0.23 | 0.6423 ± 0.16 |

**Key:** dx, dy,dz = Cartesian components of displacement.

The results show that increasing the voxel size leads to a systematic overestimation of displacement measurements compared to the reference values. However, the mean norm displacement (as a function of depth *z*) of whole-body MR (0.64 mm) falls within the range obtained from the high resolution μMR (0.64 ± 0.13 mm).

## 4.7 The Limitation of Study

The limitations of this study relate to sample selection, experimental and computing aspects. The first limitation was that only two bone specimens from a single anatomical site (proximal femur) were investigated in this study. There was no attempt to represent trabecular bone with different morphologies and bone volume fraction. Additionally, the bovine bone used may not represent the human skeleton. Nonetheless, the use of these bone samples eliminated the confounding effects of pre-existing damage and heterogeneity of mineralization, which would be inescapable in the human bone. Also, obtaining a large number of samples was not an important issue for the main purpose of this study.

The relatively high density of bovine bone (Cowin 2001) also limits the direct application of these results to human bone, especially in the case of osteoporosis. Further studies in human bone or from multiple anatomic sites may be needed to identify correlations between architecture and mechanical properties.

The second limitation was the use of global thresholding to segment MR image into bone and soft tissue components. In this study, the image segmentation commercial software MIMICS, was used for image segmentation. Using the commercial package meant the choice of segmentation algorithms was restricted to global thresholding, which may not be optimum, with limited control over the parameters of the algorithm. The error may be reduced by the use of BVF-scaled FE model. It was shown in previous studies (Homminga et al. 2001, Rajapakse et al. 2010) that BVF-scaled FE models produce mechanical parameters superior to those derived from binary images, especially when the voxel dimensions are on the order of trabecular

thickness. Further work is warranted to optimize the thresholding process. The third limitation was that two of the three well-separated superglue markers placed on the surface of the bone sample, did not appear in one image. However, using MIMICS software, the corresponding anatomical features in μCT and μMR images were identified and segmented, their centres of mass serving as markers to calculate the transformation matrix.

Finally, due to a limited CPU capacity, memory and storage space for FE analysis, the 18 μm μCT image was not used. Instead, the 36 μm μCT image provided the high resolution reference. A previously reported mesh convergence study (van Rietbergen et al. 1995) indicated that, when the voxel size doubled from 20 μm to 40 μm, the voxel model converged sufficiently while the computational effort was reduced by a factor of eight. Therefore, a nominal voxel size of the order of 36 μm appears to provide acceptable balance between microstructure detail and FE computational effort (Figure 3.9 and Table 3.2).

## 4.8 Conclusions

This study has assessed the capability of whole-body, low resolution MRI-based FE analysis to predict trabecular bone mechanical properties. The apparent elastic modulus and the displacement field were assessed and compared to a high resolution μMR-derived model. The effect of image voxel size on these properties was examined using μMR images acquired with different resolutions.

Since the imaging modality generally adopted for trabecular bone analysis is μCT, μMR results were also compared to μCT. The estimated trabecular apparent elastic

modulus obtained from a linear FE analysis based on a 30 μm μMR image was within the range of the results from a μCT image of comparable voxel size. FE analysis of load levels in the elastic range indicated that the more computationally costly geometric non-linear analysis did not affect the results significantly. Hence, a linear elastic FE analysis was deemed to be sufficiently accurate at low load levels. This study has demonstrated a significant variation in the mechanical response over multiple cores excised from a trabecular bone specimen. The result is corroborated by other studies that also showed wide variation from one specimen to another.

Low resolution is a critical factor in considering the suitability of whole-body MR. The effect of voxel size on the μMR-based FEA results was investigated. Increasing the voxel size from 30 μm to 200 μm raised the apparent elastic modulus by up to 13% and 21% for bone samples A and B, respectively. For whole-body MR, with voxel size of 260 μm, the overestimate rose to 24% for both bone samples. However, the apparent tissue elastic modulus stayed within the range (722- 1207) MPa, and (777 – 1228) MPa for bone samples A and B, respectively, imaged with high resolution μMR. The variations in the apparent elastic modulus appear to correlate with differences in the bone volume fraction, which varied between 0.44 and 0.68.

In biomechanics, the effect of a mechanical load on bone tissue is usually measured as strain at selected locations by strain gauges attached to the bone surface. *In vivo* applications of this technique have obvious limitations as reported by other studies. One disadvantage of strain gauges is that they measure strain only at the points of application. FEA based on μMR and whole-body MR images was used to estimate the full displacement field in the trabecular bone specimens. The results show that increasing the voxel size leads to a systematic overestimation of displacement

measurements compared to the reference values. However, the mean norm displacement (as a function of depth *z*) of whole-body MR (0.64 mm) falls within the range obtained from the high resolution μMR (0.64 ± 0.13) mm. The results also suggest that the information provided by displacement field values may be statistically uncorrelated with the apparent elastic modulus and hence serve as an additional source of parameterization of the mechanical response of trabecular bone.

The application of whole-body MRI to trabecular bone analysis is expected to be affected not only by resolution but also by other effects arising from the low strength of the steady magnetic field, the large imaging volume, and motion artefacts. Nevertheless, both the estimated apparent elastic modulus and displacement field values are compatible with those obtained from μMR of comparable resolution.

Within the limit of this study the predictions of FE analysis derived from whole-body MR are within the range of predictions based on high resolution μMR, indicating a potential suitability of whole-body MR for assessment of bone strength.

In this study, only the average displacement was examined. However, a displacement field is potentially a rich source of information about local response that should be explored further.

# Appendix A: Selected FE Input File

```
/CLEAR, START
/FILNAME,MRI_BoneA_30um      ! Define job name (file name)
/PREP7
! Enter a title
/title, MR_BoneA_30um
!=====================================

MP,EX,1,963.49    ! Define elastic modulus material No.1 = 963.49
MP,PRXY,1,0.3     ! Define Poisson's ratio material No.1 = 0.3

! Define parameters (z coordinates in the top interfaces and end
of the each sub-model)

Z4 = 7.1122
Z3 = 3.5613
Z2 = -0.8622
Z1 = -5.3460
Z0 = -9.6493

! Input sub-model files including elements and nodes
/INPUT,sub-m1,cdb
/INPUT,sub-m2,cdb
/INPUT,sub-m3,cdb
/INPUT,sub-m4,cdb

SELTOL,0.0001
NSEL,S,LOC,Z,Z1         ! Select nodes at interface

CPINTF,AL               ! Couple node pairs at interface
NSEL,ALL

SELTOL,0.0001
NSEL,S,LOC,Z,Z2         ! Select nodes at interface

CPINTF,AL               ! Couple node pairs at interface
NSEL,ALL

SELTOL,0.0001
NSEL,S,LOC,Z,Z3         ! Select nodes at interface

CPINTF,AL               ! Couple node pairs at interface
NSEL,ALL

FINISH
!=====================================

! Activate Solution module & Solve
/SOLU
ANTYPE,STATIC           ! Static analysis

EQSLV,PCG               !CHANGE SOLVER
```

```
! Apply Base support
! NSEL, Type, Item, Comp, VMIN, VMAX, VINC, KABS
! D, NODE, Lab, VALUE, VALUE2, NEND, NINC, Lab2, Lab3, Lab4,
Lab5, Lab6

SELTOL,0.001
NSEL,S,LOC,Z,Z0
D,ALL,UZ,0
NSEL,ALL



! Fix one corner in x & y directions
NSEL,S,LOC,Z,Z0
NSEL,R,LOC,X,-11.0117
NSEL,R,LOC,Y,2.0889
D,ALL,UX,0
D,ALL,UY,0
NSEL,ALL

! Fix other corner in x direction only
NSEL,S,LOC,Z,Z0
NSEL,R,LOC,X,-3.8843
NSEL,R,LOC,Y,4.9498
D,ALL,UY,0
NSEL,ALL

! Apply vertical Z-displacement at Top
NSEL,S,LOC,Z,Z4
D,ALL,UZ,-0.2
NSEL,ALL

SAVE
SOLVE
FINISH
!=====================================

! Entre Post processor
/ POST1
! Print Results
! Print Node Displacement
INRES,NSOL
PRNSOL,U,COMP

PLDISP,2       ! Plot displacement
ANDSCL,36,0.05 ! Animate displacement at 36 frames @ 0.05 seconds
```

# Appendix B: IDL Procedures

## B.1 Procedure for the Image Registration

```
; transform.pro
; procedure to apply a predefined rigid-body transformation to a 3D
; array.
; Call: transform
; Inputs: array - The 3D array to be transformed
; x,y,z are the node coordinates in FE file
; Output: result - The transformed 3D array and displacement
;=============================================
pro transform

xyz=fltarr(3)   ; 3D Cartesian coordinates of a node
dxyz=fltarr(3)  ; 3D displacement of a node

defpath = '~zahra/interpolation' ; default path

; Get transformation parameters from a file and place in array TC
tc = fltarr(4,4)  ; initialize the array of coefficients
fname = defpath+path_sep()+'tc'  ; get full name of the file
openr, lun, fname, /get_lun
readf, lun, tc
close, lun

; Select files for input and output and open corresponding logical
; units
fname1r = dialog_pickfile(/read, path=defpath, title='Select file
with node coordinates to be transformed')
openr, lun1r, fname1r, /get_lun
fname2r = dialog_pickfile(/read, path=defpath, title='Select file
with node displacements')
openr, lun2r, fname2r, /get_lun
fname1w = dialog_pickfile(/write, path=defpath, title='Name the
output file containing transformed node coordinates')
openw, lun1w, fname1w, /get_lun

; Initialize variables
recno1= 1   ;initialize record count on lun1r
recno2= 1   ;initialize record count on lun2r
nodeid1 = 0UL  & nodeid2 = 0UL ;initialize nodeids to unsigned long
integers
nhead1 = 2                     ;number of records to be skipped
(header) on lun1r
header1 = strarr(nhead1)       ;dummy string array to read the
header into
nhead2 = 9                     ;number of records to be skipped
(header) on lun2r
header2 = strarr(nhead2)       ;dummy string array to read the
header into
; Read in coordinates and displacements node by node
while not EOF(lun1r) and not EOF(lun2r)  do begin
    ; every 21st record on lun1r starts a header
```

```
    if recno1 eq 21 then begin
      readf, lun1r, header1         ; reads dummy header (to skip)
      recno1= 1                     ; reset record count
    endif
    readf, lun1r, nodeid1, xyz      ; xyz will default to float
    recno1++

    ; every 38th record on lun2r starts a header
    if recno2 eq 38 then begin
      readf, lun2r, header2         ; reads dummy header (to skip)
      recno2 = 1                    ; reset record count
    endif
    readf, lun2r, format='(I9,3E12.5,:)', nodeid2, dxyz
    recno2++
    ; stop the program if the nodes are not the same
    if (nodeid1 ne nodeid2) then stop
    xyzdisp = xyz + dxyz     ; node position after displacement
    ; convert each vector to a 4 coordinate colum vector, transform,
    ; and reformat to a 3-element array
    tmp = transpose(tc##transpose([xyz,1])) & newxyz1 = tmp[0:2]
    tmp = transpose(tc##transpose([xyzdisp,1])) & newxyz2 = tmp[0:2]
    ; store transformed coords & displacements in a file
    printf, lun1w, nodeid1,xyz,dxyz ;newxyz1, newxyz2-newxyz1
endwhile
close, lun1r
close, lun2r
close, lun1w

end
```

## B.2 Discrepancy between Two Displacement Fields

```
; displ_discr_fast.pro
; Procedure to apply a linear interpolation to a 3D array
; This is a fast version of displ_discr.pro
; The gain in speed is obtained by reading the entire target file
; into memory
; Call: displ_discr_fast
; Inputs: array - The 3D array and displacement to be compare
; x,y,z are the node coordinates and dx,dy,dz are the displacement
; in reference FE file
, x1,y1,z1 are the node coordinates and dx1,dy1,dz1 are the
; displacement in target FE file
; Outputs: result - The 3D array of reference file
, the discrepancy between two displacement fields of reference and
; target file
;=============================================
pro displ_discr_fast, mean, sd, meannorm, sdnorm

xyz = fltarr(3)       ; 3D Cartesian coordinates of a reference node
dxyz = fltarr(3)      ; 3D displacement of a reference node
xyz1 = fltarr(3)      ; 3D Cartesian coordinates of a target node
dxyz1 = fltarr(3)     ; 3D displacement of a target node
nodeid = 0UL          ; initialize nodeids to unsigned long integers
thousands = 0         ; initialize the thousands count of ref nodes
; used in status reporting
vox = 0.0508            ; the target (micro-MR) voxel, assumed cubic
voxplus = 1.05*vox      ; interpolation length along each axis
diag = sqrt(3)*voxplus  ; diagonal of interpolation volume
eps = 1.E-6    ; min value of ref displacement accepted for error


defpath = '~zahra/interpolation' ; default path

;Open the target file as structure and store required data in arrays
ntarget = 0UL
fname = dialog_pickfile(/read, path=defpath, title='Select target
file')
target = read_ascii(fname,
template=ascii_template(fname),count=ntarget)
ntarget1 = ntarget - 1
; coordinate arrays
targetx = target.(1) & targety = target.(2)& targetz = target.(3)
; displacement arrays
targetdx = target.(4) & targetdy = target.(5)& targetdz = target.(6)
target = 0  ; clear memory

; Sort target x-coordinates
isort = sort(targetx)    ; once-only sort of x-coordinate field
xsorted = targetx[isort] ; use sorted file for faster searching
; xmin = xsorted[0]  & xmax = xsorted[ntarget-1]

; Open the reference file
fnamer = dialog_pickfile(/read, path=defpath, title='Select
reference file with node coordinates & displacements')
openr, lunr, fnamer, /get_lun
; Open file to record differences in displacement
```

```
fname1w= dialog_pickfile(/write, path=defpath, title='Name the
output file containing differences in node displacements')
openw, lun1w, fname1w, /get_lun
;open file to record compute stats
fname2w= dialog_pickfile(/write, path=defpath, title='Name the
output file containing stats for error')
openw, lun2w, fname2w, /get_lun

; Read in coordinates and displacements of reference nodes
inode = 0UL   ; count the nodes (only those that can be compared)
mean = dblarr(3)
meannorm = 0D
meannormsq = 0D
meansq = dblarr(3)
t = systime(1)
while not EOF(lunr) do begin
    ; read next reference node
    readf, lunr, nodeid, xyz, dxyz
    ; coordinates xyz & displacements dxyz
    refx = xyz[0] & refy = xyz[1] & refz = xyz[2]
    ;find target nodes with x-coordinate nearest to refx
    if refx lt xmin then continue  ; no match
    if refx gt xmax then continue  ; no match
    isel = value_locate(xsorted, refx)
    iselmin = isel
    diff = 0.
    ; find lowest x-value within range
    while (iselmin gt 0) and (diff lt voxplus) do
    diff = abs(refx - xsorted[--iselmin])
    iselmin++
    iselmax = isel
    diff = 0.
    ; find highest x-value within range
    while (iselmax lt ntarget1) and (diff lt voxplus) do
    diff = abs(refx - xsorted[++iselmax])
    iselmax--
    ; indices of x-field where x-values are in range
    indx = isort[iselmin:iselmax]
    indy = where(abs(refy-targety[indx]) lt voxplus, count)
    ; indx nodes with y within neighbourhood
    if count lt 1 then continue  ; no match
    ; keep only nodes that have x and y within neighbourhood
    indx = indx[indy]
    indz = where(abs(refz-targetz[indx]) lt voxplus, count)
    ; indx nodes with z within neighbourhood
    if count lt 1 then continue  ; no match
    ; keep only nodes that have x, y and z within neighbourhood
    indx = indx[indz]
    ; set up the target for neighbour nodes
    nearby = [[targetx[indx]],[targety[indx]],[targetz[indx]],
    [targetdx[indx]],[targetdy[indx]],[targetdz[indx]]]
    ; arrange so nodes data are given row by row
    nearby = transpose(nearby)
    ; interpolate (linearly) displacement at xyz in target file
    ; initialize the denominator and numerator of the interpolator
    den = 0.
    num = fltarr(3)

    for i=0,count-1 do begin ; compute the interpolated displacement
      xyz1 = nearby(0:2,i)
```

```
      dxyz1 = nearby(3:*,i)
      p = abs(diag - norm(xyz1-xyz))
      den = den + p
      num = num + p*dxyz1
    endfor
    dxyz2 = num/den       ; the interpolated value
    discr = dxyz2 - dxyz  ; the difference between displacements in
    ;the two files at position xyz
    ;write the difference between reference and target displacements
    printf, lun1w, nodeid, xyz, discr
    inode++                           ; increment node count
    if (inode/1000) gt thousands then begin
      t2 = systime(1)
      print,'Progress:',100.*inode/ntarget,'%',t2-t,'s/1000 nodes'
      t = t2
      thousands++
    endif
    mean = mean + discr        ; sum for the mean of error
    meansq = meansq + discr^2  ; sum for the variance
    tmp = norm(discr)
    meannorm = meannorm + tmp  ; sum for mean displacement length
    meannormsq = meannormsq + tmp^2 ; sum for variance of
    ; displacement length
endwhile
close, lunr
close, lun1w
print, inode      ;diagnostic
; compute stats
if inode gt 0 then begin
      mean = mean/inode
      sd = sqrt(meansq/inode - mean^2)
      meannorm = meannorm/inode
      sdnorm = sqrt(meannormsq/inode - meannorm^2)

endif else print, 'No neighbours found for any reference nodes'
printf,lun2w, '% mean', mean, '% sd', sd, '% meannorm', meannorm,
'% sdnorm', sdnorm
close, lun2w
end
```

# References


Adams, V. & Askenazi, A. 1999, *Building better products with finite element analysis*, Santa Fe, NM.

Arndt, A., Westblad, P., Ekenman, I., Halvorsen, K. & Lundberg, A. 1999, 'An in vitro comparison of bone deformation measured with surface and staple mounted strain gauges', *Journal of Biomechanics*, vol. 32, no. 12, pp. 1359-63.

Banerjee, S., Han, E.T., Krug, R., Newitt, D.C. & Majumdar, S. 2005, 'Application of refocused steady-state free-precession methods at 1.5 and 3 T to in vivo high-resolution MRI of trabecular bone: Simulations and experiments', *Journal of Magnetic Resonance Imaging*, vol. 21, no. 6, pp. 818-25.

Barker, D.S., Netherway, D.J., Krishnan, J. & Hearn, T.C. 2005, 'Validation of a finite element model of the human metacarpal', *Medical Engineering & Physics*, vol. 27, no. 2, pp. 103-13.

Bauer, J.S. & Link, T.M. 2009, 'Advances in osteoporosis imaging', *European Journal of Radiology*, vol. 71, no. 3, pp. 440-9.

Bayraktar, H.H. & Keaveny, T.M. 2004, 'Mechanisms of uniformity of yield strains for trabecular bone', *Journal of Biomechanics*, vol. 37, no. 11, pp. 1671-8.

Bayraktar, H.H., Morgan, E.F., Niebur, G.L., Morris, G.E., Wong, E.K. & Keaveny, T.M. 2004a, 'Comparison of the elastic and yield properties of human femoral trabecular and cortical bone tissue', *Journal of Biomechanics*, vol. 37, no. 1, pp. 27-35.

Benoit, A., Guérard, S., Gillet, B., Guillot, G., Hild, F., Mitton, D., Périé, J.-N. & Roux, S. 2009, '3D analysis from micro-MRI during in situ compression on cancellous bone', *Journal of Biomechanics*, vol. 42, no. 14, pp. 2381-6.

Bessho, M., Ohnishi, I., Matsuyama, J., Matsumoto, T., Imai, K. & Nakamura, K. 2007, 'Prediction of strength and strain of the proximal femur by a CT-based finite element method', *Journal of Biomechanics*, vol. 40, no. 8, pp. 1745-53.

Bevill, G., Eswaran, S.K., Gupta, A., Papadopoulos, P. & Keaveny, T.M. 2006, 'Influence of bone volume fraction and architecture on computed large-deformation failure mechanisms in human trabecular bone', *Bone*, vol. 39, no. 6, pp. 1218-25.

Bevill, G. & Keaveny, T.M. 2009, 'Trabecular bone strength predictions using finite element analysis of micro-scale images at limited spatial resolution', *Bone*, vol. 44, no. 4, pp. 579-84.

Biswas, R., Bae, W., Diaz, E., Masuda, K., Chung, C.B., Bydder, G.M. & Du, J. 2012, 'Ultrashort echo time (UTE) imaging with bi-component analysis: Bound and free water evaluation of bovine cortical bone subject to sequential drying', *Bone*, vol. 50, no. 3, pp. 749-55.

Black, D.M., Greenspan, S.L., Ensrud, K.E., Palermo, L., McGowan, J.A., Lang, T.F., Garnero, P., Bouxsein, M.L., Bilezikian, J.P. & Rosen, C.J. 2003, 'The effects of parathyroid hormone and alendronate alone or in combination in postmenopausal osteoporosis', *New England Journal of Medicine*, vol. 349, no. 13, pp. 1207-15.

Boehm, H.F., Raeth, c., Monetti, R.A., Mueller, D., Newitt, D.C., Majumdar, S., Rummeny, E., Morfill, G. & Link, T.M. 2003, 'Local 3D scaling properties for the analysis of trabecular bone extracted from high resolution magnetic

resonance imaging of human trabecular bone: comparison with bone mineral density in the prediction of biomechanical strength in vitro', *Investigative Radiology*, vol. 38, no. 5, pp. 269-80.

Bonse, U., Busch, F., Günnewig, O., Beckmann, F., Pahl, R., Delling, G., Hahn, M. & Graeff, W. 1994, '3D computed x-ray tomography of human cancellous bone at 8 μm spatial and 10−4 energy resolution', *Bone and Mineral*, vol. 25, no. 1, pp. 25-38.

Borah, B., Gross, G.J., Dufresne, T.E., Smith, T.S., Cockman, M.D., Chmielewski, P.A., Lundy, M.W., Hartke, J.R. & Sod, E.W. 2001, 'Three-dimensional microimaging (MRμI and μCT), finite element modeling, and rapid prototyping provide unique insights into bone architecture in osteoporosis', *The Anatomical Record*, vol. 265, no. 2, pp. 101-10.

Boutroy, S., Bouxsein, M.L., Munoz, F. & Delmas, P.D. 2005, 'In vivo assessment of trabecular bone microarchitecture by high-resolution peripheral quantitative computed tomography', *Journal of Clinical Endocrinology & Metabolism*, vol. 90, no. 12, pp. 6508-15.

Boutry, N., Cortet, B., Dubois, P., Marchandise, X. & Cotten, A. 2003, 'Trabecular bone structure of the calcaneus: preliminary in vivo MR imaging assessment in men with osteoporosis1', *Radiology*, vol. 227, no. 3, pp. 708-17.

Boyd, S.K. & Muller, R. 2006, 'Smoothing surface meshing for automated finite element model generation from 3D image data', *Journal of Biomechanics*, vol. 39, pp. 1287-95.

Braun, M. 2005, *Gravitational potential model. Technical Note*, University of Technology, Sydney.

Braun, M. 2012, 'Note on interpolation of displacement fields', unpublished, University of Technology, Sydney.

Brenner, D.J. & Hall, E.J. 2007, 'Computed tomography — an increasing source of radiation exposure', *New England Journal of Medicine*, vol. 357, no. 22, pp. 2277-84.

Brown, M.A. & Semelka, R.C. (eds) 2005, *MRI: basic principles and applications*, 3rd edn, John Wiley & Sons, Inc.

Buckley, J.M., Loo, K. & Motherway, J. 2007, 'Comparison of quantitative computed tomography-based measures in predicting vertebral compressive strength', *Bone*, vol. 40, no. 3, pp. 767-74.

Callaghan, P.T. 1991, *Principles of nuclear magnetic resonance microscopy*, Oxford University Press.

Camacho, D.L.A., Hopper, R.H., Lina, G.M. & Myers, B.S. 1997, 'An improved method for finite element mesh generation of geometrically complex structures with application to the skullbase', *Journal of Biomechanics*, vol. 30, no. 10, pp. 1067-70.

Capuani, S., Alessandri, F., Bifone, A. & Maraviglia, B. 2002, 'Multiple spin echoes for the evaluation of trabecular bone quality', *Magnetic Resonance Materials in Physics, Biology and Medicine*, vol. 14, no. 1, pp. 3-9.

Carter, D.R. & Hayes, W.C. 1977, 'The compressive behavior of bone as a two-phase porous structure', *The Journal of bone and joint surgery*, vol. 59, no. 7, pp. 954-62.

Cendre, Kaftandjian, Peix, Jourlin, Mitton & Babot 2000, 'An investigation of segmentation methods and texture analysis applied to tomographic images of

human vertebral cancellous bone', *Journal of Microscopy*, vol. 197, no. 3, pp. 305-16.

Chang, W.C.W., Christensen, T.M., Pinilla, T.P. & Keaveny, T.M. 1999, 'Uniaxial yield strains for bovine trabecular bone are isotropic and asymmetric', *Journal of Orthopaedic Research*, vol. 17, no. 4, pp. 582-5.

Charras, G.T., Koontz, J.T. & Guidberg, R.E. 1999, 'A microstructural finite element simulation of mechanically-induced bone formation', *Engineering in Medicine and Biology society, 1999. Proceedings of the 21st Annual International Conference of the IEEE*, vol. 1, p. 115

Charras, G.T. & Guldberg, R.E. 2000, 'Improving the local solution accuracy of large-scale digital image-baed finite element analyses', *Journal of Biomechanics*, vol. 33, pp. 255-9.

Chesnut, C.H., Majumdar, S., Newitt, D.C., Shields, A., Van Pelt, J., Laschansky, E., Azria, M., Kriegman, A., Olson, M., Eriksen, E.F. & Mindeholm, L. 2005, 'Effects of Salmon Calcitonin on Trabecular Microarchitecture as Determined by Magnetic Resonance Imaging: Results From the QUEST Study', *Journal of Bone and Mineral Research*, vol. 20, no. 9, pp. 1548-61.

Chevalier, Y., Pahr, D., Allmer, H., Charlebois, M. & Zysset, P. 2007, 'Validation of a voxel-based FE method for prediction of the uniaxial apparent modulus of human trabecular bone using macroscopic mechanical tests and nanoindentation', *Journal of Biomechanics*, vol. 40, no. 15, pp. 3333-40.

Chung, H.-W., Wehrli, F.W., Williams, J.L., Kugelmass, S.D. & Wehrli, S.L. 1995, 'Quantitative analysis of trabecular microstructure by 400 MHz nuclear magnetic resonance imaging', *Journal of Bone and Mineral Research*, vol. 10, no. 5, pp. 803-11.

Clarke, L.P., Velthuizen, R.P., Camacho, M.A., Heine, J.J., Vaidyanathan, M., Hall, L.O., Thatcher, R.W. & Silbiger, M.L. 1995, 'MRI segmentation: methods and applications', *Magnetic Resonance Imaging*, vol. 13, no. 3, pp. 343-68.

Cody, D.D., Gross, G.J., J. Hou, F., Spencer, H.J., Goldstein, S.A. & P. Fyhrie, D. 1999, 'Femoral strength is better predicted by finite element models than QCT and DXA', *Journal of Biomechanics*, vol. 32, no. 10, pp. 1013-20.

Cordey, J. & Gautier, E. 1999, 'Strain gauges used in the mechanical testing of bones Part II: “In vitro” and “in vivo” technique', *Injury*, vol. 30, Supp.1, no. 0, pp. SA14-20.

Cowin, S.C. (ed.) 2001, *Bone mechanics handbook*, 2nd edn, CRC Press

Crawford, R.P., Cann, C.E. & Keaveny, T.M. 2003, 'Finite element models predict in vitro vertebral body compressive strength better than quantitative computed tomography', *Bone*, vol. 33, no. 4, pp. 744-50.

Cristofolini, L., Conti, G., Juszczyk, M., Cremonini, S., Sint Jan, S.V. & Viceconti, M. 2010, 'Structural behaviour and strain distribution of the long bones of the human lower limbs', *Journal of Biomechanics*, vol. 43, no. 5, pp. 826-35.

Dickinson, A.S., Taylor, A.C., Ozturk, H. & Browne, M. 2011, 'Experimental validation of a finite element model of the proximal femur using digital image correlation and a composite bone model', *Journal of Biomechanical Engineering*, vol. 133, no. 1, p. 014504.

Dufresne, T. 1998, 'Segmentation techniques for analysis of bone by three-dimensional computed tomographic imaging', *Technology and Health Care*, vol. 6, no. 5, pp. 351-9.

El Maghraoui, A. & Roux, C. 2008, 'DXA scanning in clinical practice', *QJM*, vol. 101, no. 8, pp. 605-17.

Elmoutaouakkil, A., Peyrin, F., Elkafi, J. & Laval Jeantet, A.M. 2002, 'Segmentation of cancellous bone from high resolution computed tomography images : influence on trabecular bone measurements', *IEEE Transactions on Medical Imaging*, vol. 21, no. 4, pp. 354-62.

Feldkamp, L.A., Goldstein, S.A., Parfitt, M.A., Jesion, G. & Kleerekoper, M. 1989, 'The direct examination of three-dimensional bone architecture in vitro by computed tomography', *Journal of Bone and Mineral Research*, vol. 4, no. 1, pp. 3-11.

Felsenberg, D. & Boonen, S. 2005, 'The bone quality framework: Determinants of bone strength and their interrelationships, and implications for osteoporosis management', *Clinical Therapeutics*, vol. 27, no. 1, pp. 1-11.

Folkesson, J., Goldenstein, J., Carballido-Gamio, J., Kazakia, G., Burghardt, A.J., Rodriguez, A., Krug, R., de Papp, A.E., Link, T.M. & Majumdar, S. 2011, 'Longitudinal evaluation of the effects of alendronate on MRI bone microarchitecture in postmenopausal osteopenic women', *Bone*, vol. 48, no. 3, pp. 611-21.

Ford, J.C. & Wehrli, F.W. 1991, 'In vivo quantitative characterization of trabecular bone by NMR', *Magnetic Resonance in Medicine*, vol. 17, no. 2, pp. 543-51.

Fritton, S.P., J. McLeod, K. & Rubin, C.T. 2000, 'Quantifying the strain history of bone: spatial uniformity and self-similarity of low-magnitude strains', *Journal of Biomechanics*, vol. 33, no. 3, pp. 317-25.

Fulton, R. 2000, 'Correction for patient head movement in emission tomography', Doctor of Philosophy Thesis, University of Technology Sydney.

Gomberg, B.R., Wehrli, F.W., Vasilić, B., Weening, R.H., Saha, P.K., Song, H.K. & Wright, A.C. 2004, 'Reproducibility and error sources of μ-MRI-based

trabecular bone structural parameters of the distal radius and tibia', *Bone*, vol. 35, no. 1, pp. 266-76.

Gregory, J.S., Junold, R.M., Undrill, P.E. & Aspden, R.M. 1999, 'Analysis of trabecular bone structure using Fourier transforms and neural networks', *IEEE Transactions on Information Technology in Biomedicine*, vol. 3, no. 4, pp. 289-94.

Guldberg, R.E., Hollister, S.J. & Charras, G.T. 1998, 'The accuracy of digital image-based finite element models', *Journal of Biomechanical Engineering*, vol. 120, pp. 289-95.

Haase, A., Frahm, J., Matthaei, D., Hanicke, W. & Merboldt, K.D. 1986, 'FLASH imaging. Rapid NMR imaging using low flip-angle pulses', *Journal of Magnetic Resonance*, vol. 67, no. 2, pp. 258-66.

Harrigan, T.P., Jasty, M., Mann, R.W. & Harris, W.H. 1988, 'Limitations of the continuum assumption in cancellous bone', *Journal of Biomechanics*, vol. 21, no. 4, pp. 269-75.

Herlidou, S., Idy-Peretti, I., Grebe, R., Grados, F., Lecuyer, N. & Fardellone, P. 2001, 'Quantitative evaluation of trabecular bone structure by calcaneus MR images texture analysis of healthy volunteers and osteoporotic subjects', *Engineering in Medicine and Biology Society, 2001. Proceedings of the 23rd Annual International Conference of the IEEE*, vol. 3, pp. 2340-2 vol.3.

Hildebrand, T. & Rüegsegger, P. 1997, 'A new method for the model-independent assessment of thickness in three-dimensional images', *Journal of Microscopy*, vol. 185, no. 1, pp. 67-75.

Hildebrand, T., Laib, A., Müller, R., Dequeker, J. & Rüegsegger, P. 1999, 'Direct three-dimensional morphometric analysis of human cancellous bone:

microstructural data from spine, femur, iliac crest, and calcaneus', *Journal of Bone and Mineral Research*, vol. 14, no. 7, pp. 1167-74.

Homminga, J., Huiskes, R., Van Rietbergen, B., Rüegsegger, P. & Weinans, H. 2001, 'Introduction and evaluation of a gray-value voxel conversion technique', *Journal of Biomechanics*, vol. 34, no. 4, pp. 513-7.

Homminga, J., McCreadie, B.R., Ciarelli, T.E., Weinans, H., Goldstein, S.A. & Huiskes, R. 2002, 'Cancellous bone mechanical properties from normals and patients with hip fractures differ on the structure level, not on the bone hard tissue level', *Bone*, vol. 30, no. 5, pp. 759-64.

Huang, H., Tsai, M., Lin, D., Chien, C. & Hsu, J.-T. 2010, 'A new method to evaluate the elastic modulus of cortical bone by using a combined computed tomography and finite element approach', *Computers in Biology and Medicine*, vol. 40, no. 4, pp. 464-8.

Hwang, S.N. & Wehrli, F.W. 2002, 'Subvoxel processing: a method for reducing partial volume blurring with application to in vivo MR images of trabecular bone', *Magnetic Resonance in Medicine*, vol. 47, no. 5, pp. 948-57.

IOF 2011, <http://www.iofbonehealth.org/policy-advocacy/australia-and-new-zealand.html, 23/12/2011>.

Jara, H., Wehrli, F.W., Chung, H. & Ford, J.C. 1993, 'High-resolution variable flip angle 3D MR imaging of trabecular microstructure in vivo', *Magnetic Resonance in Medicine*, vol. 29, no. 4, pp. 528-39.

Jiroušek, O., Zlámal, P., Kytýř, D. & Kroupa, M. 2011, 'Strain analysis of trabecular bone using time-resolved X-ray microtomography', *Nuclear Instruments and Methods in Physics Research Section A*, vol. 633, Supp.1, no. 0, pp. S148-51.

Juras, V., Welsch, G., Bär, P., Kronnerwetter, C., Fujita, H. & Trattnig, S. 2012, 'Comparison of 3 T and 7 T MRI clinical sequences for ankle imaging', *European Journal of Radiology*, vol. 81, no. 8, pp. 1846-50.

Kabel, J., Van Rietbergen, B., Dalstra, M., Odgaard, A. & Huiskes, R. 1999, 'The role of an effective isotropic tissue modulus in the elastic properties of cancellous bone', *Journal of Biomechanics*, vol. 32, pp. 673-80.

Kazakia, G.J., Burghardt, A.J., Link, T.M. & Majumdar, S. 2011, 'Variations in morphological and biomechanical indices at the distal radius in subjects with identical BMD', *Journal of Biomechanics*, vol. 44, no. 2, pp. 257-66.

Keaveny, T.M., Guo, X.E., Wachtel, E.F., McMahon, T.A. & Hayes, W.C. 1994, 'Trabecular bone exhibits fully linear elastic behavior and yields at low strains', *Journal of Biomechanics*, vol. 27, no. 9, pp. 1127-36.

Keaveny, T.M., Pinilla, T.P., Crawford, R.P., Kopperdahl, D.L. & Lou, A. 1997, 'Systematic and random errors in compression testing of trabecular bone', *Journal of Orthopaedic Research*, vol. 15, no. 1, pp. 101-10.

Keaveny, T.M., Morgan, E.F., Niebur, G.L. & Yeh, O.C. 2001, *Biomechanics of trabecular bone*.

Keaveny, T.M. & Yeh, O.C. 2002, 'Architecture and trabecular bone toward an improved understanding of the biomechanical effect of age,sex and osteoporosis', *Journal of Musculoskel Neuron Interact*, vol. 2, no. 3, pp. 205-8.

Keyak, J.H. & Skinner, H.B. 1992, 'Three-dimensional finite element modelling of bone: effects of element size ', *Journal of Biomechanical Engineering*, vol. 14, pp. 483-9.

Keyak, J.H., Fourkas, M.G., Meagher, J.M. & Skinner, H.B. 1993, 'Validation of an automated method of three-dimensional finite element modelling of bone', *Journal of Biomedical Engineering*, vol. 15, no. 6, pp. 505-9.

Keyak, J.H. & Rossi, S.A. 2000, 'Prediction of femoral fracture load using finite element models: an examination of stress- and strain-based failure theories', *Journal of Biomechanics*, vol. 33, no. 2, pp. 209-14.

Keyak, J.H. & Falkinstein, Y. 2003, 'Comparison of in situ and in vitro CT scan-based finite element model predictions of proximal femoral fracture load', *Medical Engineering and Physics*, vol. 25, no. 9, pp. 781-7.

Kim, N., Lee, J.-G., Song, Y., Kim, H.J., S. Yeom, J. & Cho, G. 2012, 'Evaluation of MRI resolution affecting trabecular bone parameters: Determination of acceptable resolution', *Magnetic Resonance in Medicine*, vol. 67, no. 1, pp. 218-25.

Kopperdahl, D.L. & Keaveny, T.M. 1998, 'Yield strain behavior of trabecular bone', *Journal of Biomechanics*, vol. 31, no. 7, pp. 601-8.

Laib, A., Hauselmann, H.J. & Ruegsegger, P. 1998, 'In vivo high resolution 3D-QCT of the human forearm', *Technology and health care* vol. 6, no. 5-6, pp. 329-37.

Laib, A., Beuf, O., Issever, A., Newitt, D.C. & Majumdar, S. 2001, 'Direct measures of trabecular bone architecture from MR images', *Advances in experimental medicine and biology*, vol. 496, pp. 37-46.

Lammentausta, E., Hakulinen, M.A., Jurvelin, J.s. & Nieminen, M.T. 2006, 'Prediction of mechanical properties of trabecular bone using quantitative MRI ', *Physics in Medicine and Biology*, vol. 51, pp. 6187-98.

Laz, P.J., Stowe, J.Q., Baldwin, M.A., Petrella, A.J. & Rullkoetter, P.J. 2007, 'Incorporating uncertainty in mechanical properties for finite element-based evaluation of bone mechanics', *Journal of Biomechanics*, vol. 40, no. 13, pp. 2831-6.

Les, C.M., Keyak, J.H., Stover, S.M. & Taylor, K.T. 1997, 'Development and validation of a series of three-dimensional finite element models of the equine metacarpus', *Journal of Biomechanics*, vol. 30, no. 7, pp. 737-42.

Lespessailles, E., Chappard, C., Bonnet, N. & Benhamou, C.L. 2006, 'Imaging techniques for evaluating bone microarchitecture ', *Joint Bone Spine* vol. 73, pp. 254-61.

Li, C.Q., Magland, J.F., Rajapakse, C.S., Guo, X.E., Zhang, X.H., Vasilic, B. & Wehrli, F.W. 2008, 'Implications of resolution and noise for in vivo micro-MRI of trabecular bone', *Medical Physics*, vol. 35, no. 12, pp. 5584-94.

Li, H. & Wang, Z. 2006, 'Intervertebral disc biomechanical analysis using the finite element modelling based on medical images ', *Computerized Medical Imaging and Graphics* vol. 30, pp. 363-70.

Linde, F. & Hvid, I. 1989, 'The effect of constraint on the mechanical behaviour of trabecular bone specimens', *Journal of Biomechanics*, vol. 22, no. 5, pp. 485-90.

Link, T., Vieth, V., Stehling, C., Lotter, A., Beer, A., Newitt, D. & Majumdar, S. 2003, 'High-resolution MRI vs multislice spiral CT: Which technique depicts the trabecular bone structure best?', *European Radiology*, vol. 13, no. 4, pp. 663-71.

Link, T.M., Majumdar, S., Konermann, W., Meier, N., Lin, J.C., Newitt, D.C., Ouyang, X., Peters, P.E. & Genant, H.K. 1997, 'Texture analysis of direct

magnification radiographs of vertebral specimens: correlation with bone mineral density and biomechanical properties', *Academic Radiology*, vol. 4, no. 3, pp. 167-76.

Link, T.M., Majumdar, S., Augat, P., Lin, J.C., Newitt, D.C., Lu, Y., Lane, N.E. & Genant, H.K. 1998a, 'In vivo high resolution MRI of the calcaneus:Difference in trabecular structure in osteoporosis patients', *Journal of Bone and Mineral Research*, vol. 13, no. 7, pp. 1175-82.

Link, T.M., Majumdar, S., Lin, J.C., Newitt, D., Augat, P., Ouyang, X., Mathur, A. & Genant, H.K. 1998b, 'A comparative study of trabecular bone properties in the spine and femur using high resolution MRI and CT', *Journal of Bone and Mineral Research*, vol. 13, no. 1, pp. 122-32.

Ludescher, B., Martirosian, P., Lenk, S., Machann, J., Dammann, F., Schick, F., Claussen, C. & Schlemmer, H. 2005, 'High-resolution magnetic resonance imaging of trabecular bone in the wrist at 3 tesla: initial results', *Acta Radiologica*, vol. 46, no. 3, pp. 306-9.

Ma, J., Wehrli, F.W. & Song, H.K. 1996, 'Fast 3D large-angle spin-echo imaging (3D FLASE)', *Magnetic Resonance in Medicine*, vol. 35, no. 6, pp. 903-10.

MacNeil, J.A. & Boyd, S.K. 2008, 'Bone strength at the distal radius can be estimated from high-resolution peripheral quantitative computed tomography and the finite element method', *Bone*, vol. 42, no. 6, pp. 1203-13.

Majumdar, S., Genant, H.K., Grampp, S., Jergas, M.D., Newitt, D.C. & Gies, A.A. 1994, 'Analysis of trabecular bone structure in the distal radius using high-resolution MRI', *European Radiology*, vol. 4, no. 6, pp. 517-24.

Majumdar, S., Newitt, D., Jergas, M., Gies, A., Chiu, E., Osman, D., Keltner, J., Keyak, K. & Genant, H. 1995, 'Evaluation of technical factors affecting the

quantification of trabecular bone structure using magnetic resonance imaging', *Bone*, vol. 17, no. 4, pp. 417-30.

Majumdar, S., Newitt, D., Mathur, A., Osman, D., Gies, A., Chiu, E., Lotz, J., Kinney, J. & Genant, H. 1996, 'Magnetic resonance imaging of trabecular bone structure in the distal radius: Relationship with X-ray tomographic microscopy and biomechanics', *Osteoporosis International*, vol. 6, no. 5, pp. 376-85.

Majumdar, S., Kothari, M., Augat, P., Newitt, D.C., Link, T.M., Lin, J.C., Lang, T., Lu, Y. & Genant, H.K. 1998a, 'High-resolution magnetic resonance imaging:Three-dimensional trabecular bone architecture and biomechanical properties', *Bone*, vol. 22, no. 5, pp. 445-54.

Marshall, D., Johnell, O. & Wedel, H. 1996, 'Meta-analysis of how well measures of bone mineral density predict occurrence of osteoporotic fractures', *BMJ*, vol. 312, no. 7041, pp. 1254-9.

McDonnell, P., Harrison, N., Liebschner, M.A.K. & McHugh, P.E. 2009, 'Simulation of vertebral trabecular bone loss using voxel finite element analysis', *Journal of Biomechanics*, vol. 42, no. 16, pp. 2789-96.

Mittra, E., Rubin, C. & Qin, Y.-X. 2005, 'Interrelationship of trabecular mechanical and microstructural properties in sheep trabecular bone', *Journal of Biomechanics*, vol. 38, no. 6, pp. 1229-37.

Mittra, E., Rubin, C., Gruber, B. & Qin, Y.-X. 2008, 'Evaluation of trabecular mechanical and microstructural properties in human calcaneal bone of advanced age using mechanical testing, μCT, and DXA', *Journal of Biomechanics*, vol. 41, no. 2, pp. 368-75.

Morgan, E.F. & Keaveny, T.M. 2001, 'Dependence of yield strain of human trabecular bone on anatomic site', *Journal of Biomechanics*, vol. 34, no. 5, pp. 569-77.

Morgan, E.F., Bayraktar, H.H., Yeh, O.C., Majumdar, S., Burghardt, A. & Keaveny, T.M. 2004, 'Contribution of inter-site variations in architecture to trabecular bone apparent yield strains', *Journal of Biomechanics*, vol. 37, no. 9, pp. 1413-20.

Mueller, T.L., Christen, D., Sandercott, S., Boyd, S.K., van Rietbergen, B., Eckstein, F., Lochmüller, E.-M., Müller, R. & van Lenthe, G.H. 2011, 'Computational finite element bone mechanics accurately predicts mechanical competence in the human radius of an elderly population', *Bone*, vol. 48, no. 6, pp. 1232-8.

Muller, R. & Ruegsegger, P. 1995, 'Three-dimentional finite element modelling of non-invasively assessed trabecular bone structures ', *Medical Engineering and Physics*, vol. 17, no. 2, pp. 126-33.

Muller, R. & Harry van Lenthe, G. 2006, 'Trabecular bone failure at the microstructural level', *Current Osteoporosis Reports*, vol. 4, no. 2, pp. 80-6.

Müller, R., Gerber, S.C. & Hayes, W.C. 1998, 'Micro-compression: a novel technique for the nondestructive assessment of local bone failure', *Technology and Health Care*, vol. 6, no. 5, pp. 433-44.

Nagaraja, S., Couse, T.L. & Guldberg, R.E. 2005, 'Trabecular bone microdamage and microstructural stresses under uniaxial compression', *Journal of Biomechanics*, vol. 38, no. 4, pp. 707-16.

Nazarian, A. & Müller, R. 2004, 'Time-lapsed microstructural imaging of bone failure behavior', *Journal of Biomechanics*, vol. 37, no. 1, pp. 55-65.

Newitt, D.C., Majumdar, S., Van Rietbergen, B., Von Ingersleben, G., Harris, S.T., Genant, H.K., Chesnut, C., Garnero, P. & Mac Donald, B. 2002, 'In vivo assessment of architecture and micro-finite element analysis derived indices of mechanical properties of trabecular bone in the radius', *Osteoporosis International*, vol. 13, pp. 6-17.

Newitt, D.C., van Rietbergen, B. & Majumdar, S. 2002a, 'Processing and analysis of in vivo high-resolution MR images of trabecular bone for longitudinal studies: reproducibility of structural measures and micro-finite element analysis derived mechanical properties', *Osteoporosis International*, vol. 13, no. 4, pp. 278-87.

Nikro, M. 2008, 'Investigation of the properties of bone and bonelike materials', Engineering Capstone Project Report, University of Technology, Sydney. .

Odgaard, A. & Linde, F. 1991, 'The underestimation of Young's modulus in compressive testing of cancellous bone specimens', *Journal of Biomechanics*, vol. 24, no. 8, pp. 691-8.

Orzada, S., Bitz, A.K., Schafer, L.C., Ladd, S.C., Ladd, M.E. & Maderwald, S. 2011, 'Open design eight-channel transmit/receive coil for high-resolution and real-time ankle imaging at 7 T', *Medical Physics*, vol. 38, no. 3, pp. 1162-7.

Ouyang, X., Selby, K., Lang, P., Engelke, K., Klifa, C., Fan, B., Zucconi, F., Hottya, G., Chen, M., Majumdar, S. & Genant, H.K. 1997, 'High resolution magnetic resonance imaging of the calcaneus: age-related changes in trabecular structure and comparison with dual x-ray absorptiometry measurements', *Calcified Tissue International*, vol. 60, no. 2, pp. 139-47.

Pal, B., Gupta, S., New, A.M.R. & Browne, M. 2010, 'Strain and micromotion in intact and resurfaced composite femurs: Experimental and numerical investigations', *Journal of Biomechanics*, vol. 43, no. 10, pp. 1923-30.

Palombarini, M., Gombia, M., Fantazzini, P., Giardino, R., Giavaresi, G., Parrilli, A., Vittur, F. & Guillot, G. 2009, 'Inhomogeneity of rat vertebrae trabecular architecture by high-field 3D μ-magnetic resonance imaging and variable threshold image segmentation', *Journal of Magnetic Resonance Imaging*, vol. 30, no. 4, pp. 825-33.

Peyrin, F., Salome, M., Cloetens, P., Laval-Jeantet, A.M., Ritman, E. & Rüegsegger, P. 1998, 'Micro-CT examinations of trabecular bone samples at different resolutions: 14, 7 and 2 micron level', *Technology and Health Care*, vol. 6, no. 5, pp. 391-401.

Raeth, C.W., Mueller, D., Rummeny, E.J., Link, T.M., Vogel, M., Koenig, H., Boehm, H. & Monetti, R. 2006, 'Optimizing texture measures quantifying bone structures as well as MR-sequences at 3 Tesla: an integrative statistical approach', Proc. SPIE 6144, 61440E <http://dx.doi.org/10.1117/12.652131>.

Rajapakse, C.S., Magland, J.F., Wald, M.J., Liu, X.S., Zhang, X.H., Guo, X.E. & Wehrli, F.W. 2010, 'Computational biomechanics of the distal tibia from high-resolution MR and micro-CT images', *Bone*, vol. 47, no. 3, pp. 556-63.

Rüegsegger, P., Koller, B. & Müller, R. 1996, 'A microtomographic system for the nondestructive evaluation of bone architecture', *Calcified Tissue International*, vol. 58, no. 1, pp. 24-9.

Ryan, S.D. & Williams, J.L. 1989, 'Tensile testing of rodlike trabeculae excised from bovine femoral bone', *Journal of Biomechanics*, vol. 22, no. 4, pp. 351-5.

Ryoyama, D., Sawaki, Y. & Ueda, M. 2004, 'Experimental study of mechanical analysis in mandibular lengthening: Application of strain gauge measurement', *International Journal of Oral and Maxillofacial Surgery*, vol. 33, no. 3, pp. 294-300.

Schileo, E., Taddei, F., Cristofolini, L. & Viceconti, M. 2008, 'Subject-specific finite element models implementing a maximum principal strain criterion are able to estimate failure risk and fracture location on human femurs tested in vitro', *Journal of Biomechanics*, vol. 41, no. 2, pp. 356-67.

Seeman, E. & Delmas, P.D. 2006, 'Bone quality — the material and structural basis of bone strength and fragility', *New England Journal of Medicine*, vol. 354, no. 21, pp. 2250-61.

Sell, C.A., Masi, J.N., Burghardt, A., Newitt, D., Link, T.M. & Majumdar, S. 2005, 'Quantification of trabecular bone structure using magnetic resonance imaging at 3 tesla—calibration studies using microcomputed tomography as a standard of reference', *Calcified Tissue International*, vol. 76, no. 5, pp. 355-64.

Shahar, R., Banks-Sills, L. & Eliasy, R. 2003, 'Stress and strain distribution in the intact canine femur: finite element analysis', *Medical Engineering and Physics*, vol. 25, no. 5, pp. 387-95.

Steele, J.M. 1989, *Applied finite element modeling*, M. Dekker, New York.

Stolk, J., Verdonschot, N., Cristofolini, L., Toni, A. & Huiskes, R. 2002, 'Finite element and experimental models of cemented hip joint reconstructions can produce similar bone and cement strains in pre-clinical tests', *Journal of Biomechanics*, vol. 35, no. 4, pp. 499-510.

Stone, K.L., Seeley, D.G., Lui, L.-Y., Cauley, J.A., Ensrud, K., Browner, W.S., Nevitt, M.C. & Cummings, S.R. 2003, 'BMD at multiple sites and risk of fracture of multiple types: long-term results from the study of osteoporotic fractures', *Journal of Bone and Mineral Research*, vol. 18, no. 11, pp. 1947-54.

Takahashi, M., Saha, P.K. & Wehrli, F.W. 2006, 'Skeletal effects of short-term exposure to dexamethasone and response to risedronate treatment studied in vivo in rabbits by magnetic resonance micro-imaging and spectroscopy', *Journal of Bone and Mineral Metabolism*, vol. 24, no. 6, pp. 467-75.

Talaia, P., Ramos, A., Abe, I., Schiller, M., Lopes, P., Nogueira, R., Pinto, J., Claramunt, R. & Simões, J. 2007, 'Plated and Intact Femur Strains in Fracture Fixation Using Fiber Bragg Gratings and Strain Gauges', *Experimental Mechanics*, vol. 47, no. 3, pp. 355-63.

Turner, C.H. 1989, 'Yield behavior of bovine cancellous bone', *Journal of Biomechanical Engineering*, vol. 111, no. 3, pp. 256-60.

Ulrich, D., van Rietbergen, B., Laib, A. & Ruegsegger, P. 1999, 'The ability of three-dimensional structural indices to reflect mechanical aspects of trabecular bone', *Bone*, vol. 25, no. 1, pp. 55-60.

Ün, K., Bevill, G. & Keaveny, T.M. 2006, 'The effects of side-artifacts on the elastic modulus of trabecular bone', *Journal of Biomechanics*, vol. 39, no. 11, pp. 1955-63.

van Rietbergen, B., Weinans, H., Huiskes, R. & Odgaard, A. 1995, 'A new method to determine trabecular bone elastic properties and loading using micromechanical finite element models', *Journal of Biomechanics*, vol. 28, no. 1, pp. 69-81.

van Rietbergen, B., Mueller, R., Ulrich, D. & Ruegsegger, P. 1999, 'Tissue stresses and strain in trabeculae of canine proximal femur can be quantified from computer reconstructions', *Journal of Biomechanics*, vol. 32, no. 4, pp. 443-51.

van Rietbergen, B. 2001, 'Micro-FE analyses of bone: state of the art', *Advances in Experimental Medicine and Biology*, vol. 496, pp. 21-30.

van Rietbergen, B., Majumdar, S., Newitt, D. & MacDonald, B. 2002, 'High-resolution MRI and micro-FE for the evaluation of changes in bone mechanical properties during longitudinal clinical trials: application to calcaneal bone in postmenopausal women after one year of idoxifene treatment', *Clinical Biomechanics*, vol. 17, no. 2, pp. 81-8.

Varghese, B., Short, D., Penmetsa, R., Goswami, T. & Hangartner, T. 2011, 'Computed-tomography-based finite-element models of long bones can accurately capture strain response to bending and torsion', *Journal of Biomechanics*, vol. 44, no. 7, pp. 1374-9.

Verhulp, E., Rietbergen, B.v. & Huiskes, R. 2004, 'A three-dimensional digital image correlation technique for strain measurements in microstructures', *Journal of Biomechanics*, vol. 37, no. 9, pp. 1313-20.

Verhulp, E., van Rietbergen, B. & Huiskes, R. 2006, 'Comparison of micro-level and continuum-level voxel models of the proximal femur', *Journal of Biomechanics*, vol. 39, no. 16, pp. 2951-7.

Viceconti, M., Zannoni, C., Testi, D. & Cappello, A. 1999, 'A new method for the automatic mesh generation of bone segments from CT data', *Journal of Medical Engineering & Technology*, vol. 23, no. 2, pp. 77-81.

Viceconti, M., Davinelli, M., Taddei, F. & Cappello, A. 2004, 'Automatic generation of accurate subject-specific bone finite element models to be used in clinical studies', *Journal of Biomechanics*, vol. 37, no. 10, pp. 1597-605.

Waarsing, J.H., Day, J.S. & Weinans, H. 2004, 'An Improved Segmentation Method for In Vivo μCT Imaging', *Journal of Bone and Mineral Research*, vol. 19, no. 10, pp. 1640-50.

Wald, M.J., Magland, J.F., Rajapakse, C.S. & Wehrli, F.W. 2010, 'Structural and mechanical parameters of trabecular bone estimated from in vivo high-resolution magnetic resonance images at 3 tesla field strength', *Journal of Magnetic Resonance Imaging*, vol. 31, no. 5, pp. 1157-68.

Wang, Z.L., Teo, J.C.M., Chui, C.K., Ong, S.H., Yan, C.H., Wang, S.C., Wong, H.K. & Teoh, S.H. 2005, 'Computational biomechanical modeling of the Lumbar spine using marching-cubes surface smoothened finite element voxel mashing ', *Computer Methods and Programs in Biomedicine*, vol. 80, pp. 25-35.

Wehrli, F.W., Hwang, S.N., Ma, J., Song, H.K., Ford, J.C. & Haddad, J.G. 1998, 'Cancellous bone volume and structure in the forearm: noninvasive assessment with MR microimaging and image processing', *Radiology*, vol. 206, no. 2, pp. 347-57.

Wehrli, F.W., Saha, P.K., Gomberg, B.R. & Hee Kwon, S. 2003, 'Noninvasive assessment of bone architecture by magnetic resonance micro-imaging-based virtual bone biopsy', *Proceedings of the IEEE*, vol. 91, no. 10, pp. 1520-42.

Wehrli, F.W., Song, H.K., Saha, P.K. & Wright, A.C. 2006, 'Quantitative MRI for the assessment of bone structure and function', *NMR in Biomedicine*, vol. 19, no. 7, pp. 731-64.

Wehrli, F.W., Ladinsky, G.A., Jones, C., Benito, M., Magland, J., Vasilic, B., Popescu, A.M., Zemel, B., Cucchiara, A.J., Wright, A.C., Song, H.K., Saha, P.K., Peachey, H. & Snyder, P.J. 2008, 'In vivo magnetic resonance detects rapid remodeling changes in the topology of the trabecular bone network after menopause and the protective effect of estradiol', *Journal of Bone and Mineral Research*, vol. 23, no. 5, pp. 730-40.

WHO Scientific Group 2003, *Prevention and management of osteoporosis*, World Health Organization, <http://whqlibdoc.who.int/trs/who_trs_921.pdf>.

Wolfram, U., Wilke, H.-J. & Zysset, P.K. 2010, 'Valid μ finite element models of vertebral trabecular bone can be obtained using tissue properties measured with nanoindentation under wet conditions', *Journal of Biomechanics*, vol. 43, no. 9, pp. 1731-7.

Wright, A.C., Lemdiasov, R., Connick, T.J., Bhagat, Y.A., Magland, J.F., Song, H.K., Toddes, S.P., Ludwig, R. & Wehrli, F.W. 2011, 'Helmholtz-pair transmit coil with integrated receive array for high-resolution MRI of trabecular bone in the distal tibia at 7 T', *Journal of Magnetic Resonance*, vol. 210, no. 1, pp. 113-22.

Zauel, R., Yeni, Y.N., Bay, B.K., Dong, X.N. & Fyhrie, D.P. 2006, 'Comparison of the linear finite element prediction of deformation and strain of human cancellous bone to 3D digital volume correlation measurements', *Journal of Biomechanical Engineering*, vol. 128, no. 1, pp. 1-6.

Zhang, X.H., Liu, X.S., Vasilic, B., Wehrli, F.W., Benito, M., Rajapakse, C.S., Snyder, P.J. & Guo, X.E. 2008, 'In vivo μMRI-based finite element and morphological analyses of tibial trabecular bone in eugonadal and

hypogonadal men before and after testosterone treatment', *Journal of Bone and Mineral Research*, vol. 23, no. 9, pp. 1426-34.